Università degli studi di Genova
Facoltà di Scienze Matematiche, Fisiche e Naturali

Physics Department

This thesis is submitted for the degree of
Doctor of Philosophy
XXX cycle

The CUORE experiment: from the commissioning to the first $0\nu\beta\beta$ limit.

Candidate: Laura Marini

Supervisors: Prof. Marco Pallavicini
Dr. Sergio Di Domizio

March 2018

The terrible tragedies of science
are the horrible murders
of beautiful theories by ugly facts.

W. A. Fowler

Contents

Introduction

No proof of the existence of the neutrinoless double beta ($0\nu\beta\beta$) decay and thus of Majorana neutrinos have been observed yet. Starting from the conclusion is probably a strange way to begin a Thesis, but if $0\nu\beta\beta$ decay had already been discovered, building CUORE would not be so exciting.

CUORE stands for Cryogenic Underground Observatory for Rare Events. It is a ton-scale bolometric detector whose main goal is not only the search for $0\nu\beta\beta$ decay, but also the search for other rare events such as ones induced by dark matter and axions. CUORE is situated underground at the Laboratori Nazionali del Gran Sasso (LNGS) near l'Aquila, Italy, a location suited for rare events searches since 1400 m of rock protects the experiment from cosmic rays. CUORE uses the bolometric technique on 988 TeO_2 crystals to search for $0\nu\beta\beta$ decay of ^{130}Te , an isotope present as the 34% of natural tellurium.

CUORE is in operation since January 2017, about a year before the drafting of this Thesis. Of all the PhD students that worked for CUORE in the last 20 years and of all those who will work for CUORE in the next five years, I was very lucky to witness the moment in which this huge experiment was turned on and to share the excitement of the observation of the first particle interaction ever detected by CUORE.

This Thesis follows the CUORE experiment from the commissioning of the detector to the first limit for $0\nu\beta\beta$ decay obtained with the analysis of the first 86.3 kg·yr of exposure.

In Chapter I the basic theory for $0\nu\beta\beta$ decay through the exchange of light Majorana neutrinos will be recall, as well as the possible mechanism to get massive neutrinos. I will also describe the observables of this search as well as its problematics. Finally I will do a brief review on some of the experiments that seek to directly observe this hypothetic decay.

Chapter II is instead dedicated to the description of the bolometric technique and all the main CUORE systems, starting from the cryostat that host the crystals to end with the data acquisition system. This Chapter will be concluded by the report of the last part of the commissioning phase, the detector installation and the first complete cool down of the detector to few millikelvins.

Chapter III focuses instead on the optimization phase, that happened in part before the beginning of the data taking and in part between the first and the second data taking periods. The optimization phase had the important role of improving the energy resolution, the signal to noise ratio and the energy threshold of the experiment.
In Chapter IV I will describe the data processing of the first CUORE data and the data analysis that lead to obtain a competitive limit on $0\nu\beta\beta$ decay. In particular I will focus on the procedure to find the detector response for all the 988 bolometers, based on the study of the ^{208}Tl line.
Finally Chapter V reviews the procedure to obtain the final limit, including the analysis to get the efficiencies and systematics, and the method used to compute the limit on the half life of $0\nu\beta\beta$ decay of ^{130}Te . As last step I will expose the result of this analysis and compare them to those of other $0\nu\beta\beta$ decay experiments.

Chapter 1

Neutrinoless Double Beta Decay

The Cryogenic Underground Observatory for Rare Events (CUORE) is an experiment that mainly seeks to discover neutrinoless double beta ($0\nu\beta\beta$) decay. This first Chapter is dedicated to explain the scientific reasons for this search and to shed light on the possible mechanisms that can cause this decay. I will also briefly describe which are the observables in this search and lastly I will present an overview of the CUORE competitors, namely other experiments designed to search for $0\nu\beta\beta$ but using different materials and techniques.

1.1 A bit of history

The search for $0\nu\beta\beta$ decay is not a new trend but a search of more than 80 years old. The person who first proposed double beta decay of nuclei was M. Groeppert-Meyer in 1935. Of course she was referring to two neutrino double beta ($2\nu\beta\beta$) decay, even if at that time she called it *double beta disintegration*. Two years later, while Dirac field representation was becoming popular, E. Majorana proposed an alternative way to represent fermions in a relativistic field theory. He proposed to represent fermions with a single quantum field in which particles and antiparticles coincide. To give more strength to his hypothesis he demonstrated that all results of β decay remained unchanged if neutrinos were its own antiparticle. The merit of linking for the first time Majorana fields to massive neutrinos has been of G. Racah in 1937: he believed that Majorana's theory could lead to physical predictions, different from those of Dirac's. We can finally say that the father of $0\nu\beta\beta$ decay was W. H. Furry because in 1939 he applied Majorana's fields to Groeppert-Meyer's double beta disintegration arguing that if neutrinos where Majorana particles and therefore their own antiparticles, double beta decay should be possible without the emission of two

neutrinos as shown in equation 1.1.1

$$(Z, A) \rightarrow (Z + 2, A) + 2e^{-} \tag{1.1.1}$$

We have to wait until 1948 to see the first efforts to observe double beta decay in laboratory: E. L. Fireman attempted, without succeeding, to observe this decay from ^{124}Sn with a geiger counter. The 1950 sees the first indirect measures of $2\nu\beta\beta$ half-life by geochemical methods but double beta decay was not observed for almost other 40 years. The first observation of this rare decay happened in 1987 in a laboratory experiment with ^{82}Se carried by M. Moe. Despite its observation, double beta decay remains the rarest known kind of radioactive decay and it has been observed in only 12 isotopes and all have half-lives over 10^{19} years. The observation of the decay in this isotopes is crucial because as we will see they become the natural candidates for $0\nu\beta\beta$ decay.

1.2 Scientific motivation

In the last 20 years the scientific community has seen an increasing interest on the tiny and elusive particle that is the neutrino. It is now well established from flavour neutrino oscillation experiments that neutrinos do have mass [1]. It is also known that neutrinos are part of three lepton families: electronic, muonic and tauonic. There are however many open questions on the neutrino nature for which experiment studying flavour neutrino oscillation cannot provide information: are they Dirac or Majorana particles? Which is their mass scale and their mass ordering? The answers to all these questions might be within reach in this or next generation of experiments, thanks to the ongoing effort and to the technological development that are affecting this field. The discovery or even the presence of more stringent limits on $0\nu\beta\beta$ decay will help solving all these open issues on neutrino physics and will help understand a bit more our complicated world, including solving the mystery of the matter anti-matter asymmetry in the Universe.

1.2.1 Baryogenesis via Leptogenesis

Regardless of the mechanisms causing the $0\nu\beta\beta$ decay, this process explicitly violates the number of leptons by creating two electrons. Its observation would imply that lepton number, L, is not a symmetry of nature suggesting that leptons played an important role in the creation of matter anti-matter asymmetry in the Universe.
The Universe contains various relic particles like gammas, electrons, protons, neutrinos, deuterium and probably dark matter. Most of these abundances are well understood, with

the exception of the baryons asymmetry:

$$\frac{n_B - n_{\bar{B}}}{n_\gamma} \simeq \frac{n_B}{n_\gamma} \sim 10^{-10} \tag{1.2.1}$$

where n_γ and n_B represent respectively photons and baryon density while the anti-baryon density is negligible. The photon density follows from measurement of the CMB temperature $n_\gamma \sim T^3$, while the baryon density can be estimated using two indirect methods: the first one comes from solving Boltzman equations for neutrino decoupling and nucleosynthesis and the second by measurements of the CMB anisotropies, probing acoustic oscillations of the baryon/photon fluid around photon last scattering. This is the problem of baryogenesis.

At the time of the big-bang there was the same quantity of matter and anti-matter; during the cool down of the first Universe the annihilation of matter with anti-matter resulted in a small excess of baryons. Indeed, the fact that the visible Universe is made out of matter is just due to this small baryon asymmetry:

$$n_B - n_{\bar{B}} \approx 1000000001 - 1000000000 = 1 \tag{1.2.2}$$

without it we would never exist. Naively we could think that this small excess might be the initial condition of the big-bang, but at the same time it would represent a large excess if we believe in inflationary models, since inflation erases initial conditions. So at this point we might ask ourselves: what is the mechanism that is behind the problem of baryogenesis? One possibility is that in a scenario without any baryon asymmetry not all matter and anti-matter would been annihilated, and as the Universe was rapidly expanding some uneven quantity of baryons and anti-baryons would have frozen out and survived at temperature T$\leq m_p$, where m_p is the proton mass. Unfortunately this mechanism is not enough to explain all the matter that we see in our local Universe, since it could account only for an anisotropy of $n_B/n_\gamma \sim 10^{-19}$ [2]. If this does not work we might go for the next plausible explanation to the asymmetry: perhaps our local Universe is made out of matter and at the same time, somewhere, there is some other part of our Universe made entirely of anti-matter. In this scenario what we observe is not a real asymmetry but only an upward fluctuation in matter density. This case cannot be ruled out, however these two adjacent areas of the Universe must touch somewhere and in that case we could also see the effect of matter anti-matter annihilation nowadays. Therefore it is possible to set a limit on this hypothesis by looking carefully for annihilation lines in our observable Universe [3]. Lastly, assuming that the hot big-bang started with an equal number of baryons and anti-baryons at some temperature T$\gg m_p$, the asymmetry could possibly be generated dynamically in

the succeeding evolution. This is at present the most plausible possibility given that the Sakharov conditions [4] are provided at some stage of this evolution:

1. baryon number B is violated;
2. C and CP are violated;
3. the Universe was not in thermal equilibrium;

These three conditions, described by A. Sakharov in 1967, are the minimum properties of Nature required for any baryogenesis to occur, regardless of the exact mechanism. The first Sakharov condition is somewhat trivial: if we want to generate asymmetry we must have a mechanism of creating baryons without creating anti-baryons. If the process producing baryons and anti-baryons has the same velocity the two processes will cancel each other out, therefore, from the second Sakharov condition, we need C and CP violations so that baryons and anti-baryons do not behave in the same way. The third and last condition demands a Universe out of thermal equilibrium because if CPT is conserved, as we believe, particle and antiparticle have the same mass and in thermal equilibrium they would have the same abundance.
Before considering processes beyond the Standard Model (SM) one should check first if these conditions are met within the SM itself.

1. Within the SM, B is violated in a non trivial way by means of processes like *sphalerons* where B and L symmetry are violated, while B−L is a conserved symmetry. This process is heavily-suppressed at energies below 10 TeV, so it is not expected to occur in Nature today, but is feasible in earlier phases of Universe evolution. An example of a sphaleron process is shown in figure Figure (1.2.1) where one lepton for each generation is traded for nine quarks. Unfortunately, this process has never been observed in laboratory being out of our technological reach.

2. CP-violation in weak interactions of the SM is well-established, hence this Sakharov condition is clearly satisfied by many SM processes. However, even if there is CP-violation built into the QCD Lagrangian, it would be ∼16 [6] orders of magnitude smaller than the needed CP-violation to account for the observed baryon asymmetry.

3. The only candidate for the needed out of equilibrium conditions is the electroweak phase, but experiments shows that it needs new particles coupled to the Higgs to achieve an out-of-equilibrium phase transition. Consequently SM baryogenesis is not possible due to the lack of out-of equilibrium conditions.

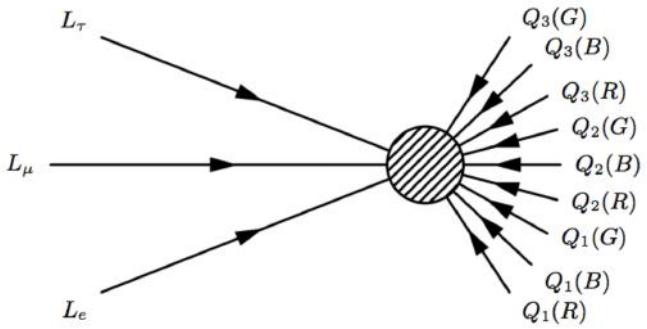

Figure 1.2.1: *Example of a sphaleron process where the incoming quantum numbers are L = 3 and B = 0 and the outgoing quantum numbers are L = 0 and B = −3. Figure from Ref. [5].*

In conclusion, if a single mechanism that can combine all Sakharov condition exists, we have to look for it within possible expansions of the SM. There are many proposal of extension of the SM to introduce a mechanism that would allow baryogenesis, but it is out of the purpose of this thesis discussing them all. I will however mention the most popular: *leptogenesis* [7]. For a more complete discussion on this topic see also Ref. [2]. In baryogenesis via leptogenesis a large excess of leptons (e.g. electrons and neutrinos) is generated by some unknown mechanism. Then, through processes conserving B−L this excess of leptons is turned directly into a baryon excess. Up to now we focused our attention on baryons, yet this mechanism turns the puzzle of baryogenesis into the lepton sector. Indeed if baryon asymmetry exists we expect also to observe an analogous lepton asymmetry such as an excess of electrons over positrons. But the symmetries of this problem stop here: as a matter of fact, it is possible to estimate baryon density from CMB anisotropies, but on the other hand lepton asymmetry is dominated by cosmic neutrino background which has never been directly detected. In short, the presence of a process that violates lepton number L, C and CP symmetries and it is out of thermal equilibrium will satisfy the equivalent of Sakharov conditions for leptogenesis. In this scenario, it is believed that neutrinos have an important role in solving the matter anti-matter asymmetry puzzle, particularly if $0\nu\beta\beta$ decay, a lepton number violating process, will be observed in the near future.

1.3 Neutrino mass generation

In the SM original formulation, neutrinos are massless, come in three flavours (electronic, muonic and tauonic), have associated antiparticles and corresponding charged leptons e, μ and τ.
The absence of neutrino masses in the SM is motivated by direct experiments that are able to set only upper bounds to neutrino masses. Furthermore, the SM predicts that neutrinos can only be left-handed, spin property[1] that was proven by M. Goldhaber, L. Grodzins and A. Sunyar in 1958 [8], only two years after the neutrino discovery. If neutrinos acquire mass with the standard mechanism that works with all other massive particles, therefore through interaction with the Higgs fields, they would need a right-handed field. But neutrinos are proven to be only left-handed, thus implying that they must be massless.
Despite the fact that for most applications stands the approximation $m_\nu \ll m_f$, where f indicates any fermion, this picture brakes down when introducing neutrinos oscillations. We now know that neutrinos do have mass, hence there must be a mass mechanism, not predicted by the SM, that allows neutrinos to acquire mass and that justify the fact that their mass is several orders of magnitude below the mass of the other SM particles as shown in Figure (1.3.1).

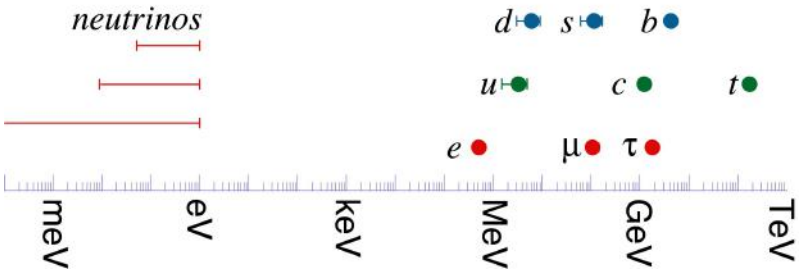

Figure 1.3.1: *Scheme of the distribution of SM particle masses pointing out the huge difference in mass scale between quarks and fermions, and the region where neutrino masses are thought to be.*

There are many possible theoretical options for producing neutrino masses, but in all we must relax some SM conditions, namely the absence of right-handed neutrinos or the fact that there are only Higgs doublets of $SU(2)_L$ or the constrain that all SM terms must be renormalizable.
Depending on which of the above SM conditions we relax, there is one or more proposals for

[1] The handness of a particles is the projection of its spin along the direction of motion, so if neutrino is left-handed it means that the spin projection is always opposite to the particle direction.

the origin of neutrino mass, resulting in five different theoretical options for mass generation mechanisms. We can have R-parity violating supersymmetry [9], implying the existence of SUSY; TeV-scale loop mechanisms generating Majorana mass from extra Higgs doubles and singlets at the TeV scale [10]; there are also extra dimensional models [11] which allows to have Dirac masses with small coupling constants due to the presence of right-handed neutrinos in the bulk; furthermore we can find new mechanisms for generating large Majorana mass for right-handed neutrinos from Planck or string scale physics [12]; and finally there is the most favoured option, called see-saw mechanism [13] which extends the SM by a simple addition of a right-handed neutrino field.
In this section I will describe only this last possible extension of the SM which allows to consistently introduce neutrino masses and to justify the smallness in their mass scale if compared with other leptons (e.g. mass of the electron).

1.3.1 Type I see-saw mechanism

The see-saw mass mechanism is one of most immediate extensions of the SM because it simply adds right-handed neutrinos. Similarly to the Higgs mechanism of the SM the addition of right-handed neutrinos results in neutrinos with the same type of mass as the Dirac mass of charged leptons and quarks.
The SM Lagrangian gains in this way a new term for three generations of left-handed neutrinos and N generations of right-handed neutrinos:

$$\mathcal{L}_{mass,\nu} = -\lambda^D_{\alpha i} \bar{L}^T_\alpha \tilde{\Phi} N_{R,i} \tag{1.3.1}$$

where $\lambda^D_{\alpha i}$ are Yukawa coupling constants, $\Phi \equiv \begin{pmatrix} \phi^+ \\ \phi^0 \end{pmatrix}$ is the scalar Higgs doublet and $L_\alpha \equiv \begin{pmatrix} \nu_{\alpha L} \\ l_{\alpha L} \end{pmatrix}$ is the left-handed doublet for any charged lepton and its neutrino; the subscript α=e, μ, τ and the index i runs over N possible right-handed neutrino states.
The Dirac masses that we just created would break separately the lepton numbers L_e, L_μ, L_τ, but conserve the total lepton number L; however neutrinos could also have the mass type, proposed by Majorana, which would also break L. The only addition of a Dirac mass term to the SM Lagrangian does create a mass, but does not explain the observed smallness of neutrino masses: indeed the presence of Dirac neutrino masses of the order of 0.1 eV implies that the Dirac Yukawa coupling λ^D must be of order 10^{-12}, thus very different from the couplings used in the mass generation of the charged leptons. Moreover right-handed neutrinos are gauge singlets, therefore nothing prevents them from acquiring

a Majorana mass term in addition to the Dirac term of Equation (1.3.1)

$$\mathcal{L}_{mass,\nu} = -\lambda^D_{\alpha i}\bar{L}^T_\alpha \tilde{\Phi} N_{R,i} - \frac{1}{2} M^R_{ij} \bar{N}_{Ri} N^c_{Rj} + h.c. \tag{1.3.2}$$

where M_{ij} could be as large as the Planck scale and the indexes ij run over the N hypothetical right-handed neutrinos. In this Majorana mass term the right-handed field is coupled to its left-handed charged conjugate field, creating a connection between a particle and its own anti-particle.
In the following passages we will demonstrate how the addition of the Majorana mass term to the SM Lagrangian naturally explains the smallness of neutrino masses. In fact if we explicitly write Equation (1.3.2) in its matrix form,

$$\begin{aligned} \mathcal{L}_{mass,\nu} &= -\bar{\nu}_{\alpha L} M^D_{\alpha i} N_{Ri} - \frac{1}{2} \bar{N}_{Ri} M^R_{ij} N^c_{Rj} + h.c. \\ &= -\frac{1}{2} \begin{pmatrix} \bar{\nu}^c_L & \bar{N}_R \end{pmatrix} \begin{pmatrix} 0 & M_D \\ M_D^T & M_R \end{pmatrix} \begin{pmatrix} \nu_L \\ N^c_R \end{pmatrix} + h.c. \end{aligned} \tag{1.3.3}$$

we can isolate the neutrino mass matrix, where the zero follows directly from the fact that right-handed neutrinos do not carry a weak charge, while left-handed neutrinos do. Note that in Equation (1.3.3) $M^D_{\alpha i} = \lambda^D_{\alpha i} \cdot v$ where v is the non-zero expectation value of the Higgs field.
We now need to make two assumptions: the first is the had hoc choice that $M_D \ll M_R$ and the second is the reasonable assumption that M_D is of the order of the other lepton masses. By diagonalizing the neutrino mass matrix in Equation (1.3.3) we obtain a term that describes a set of 3 light Majorana neutrinos with masses m_ν and N heavy Majorana neutrinos with masses M_N

$$\begin{aligned} \begin{pmatrix} 0 & M_D \\ M_D^T & M_R \end{pmatrix} \quad &\rightarrow \quad U \left[\begin{pmatrix} M_D M_R^{-1} M_D^T & 0 \\ 0 & M_R \end{pmatrix} + \mathcal{O}(M_D^4/M_R^3) \right] U^\dagger \\ &\approx \begin{pmatrix} m_\nu & 0 \\ 0 & M_N \end{pmatrix} \end{aligned} \tag{1.3.4}$$

where

$$m_\nu \equiv M_D M_R^{-1} M_D^T \qquad \text{and} \qquad M_N \equiv M_R \,. \tag{1.3.5}$$

This is the type I see-saw mechanism. As foreseen we produced 3 almost pure left-handed neutrinos whose mass is suppressed by $1/M_R$, thus their observed tiny mass is justified by the fact that M_D is much smaller than M_R. At the same time we produced a set

of almost pure right-handed neutrinos with heavy Majorana masses which were never observed because they have zero charge under SM interaction, hence called "sterile". These are also called pure Majorana neutrinos.

We can however go back to the starting point if we make a different initial assumption: $M_R \ll M_D$. In this scenario the matrix elements of Equation (1.3.4) return 3 pure Dirac neutrinos with masses $m_\nu = \lambda_\alpha^D \cdot v$ where the Yukawa couplings is of the order of 10^{-12}, thus much smaller than all other SM Yukawa couplings. In this case we must impose lepton number conservation in order to justify the vanishing of M_N.

In conclusion we can see by comparing these two scenarios that in the case of pure Majorana neutrinos their masses arise more naturally while in the other case we must force the theory to obtain only pure Dirac neutrinos. If the latter mechanism is proven to be true, we will have indeed to find the explanation to the smallness of neutrino Yukawa coupling somewhere else. For all these reasons the mass mechanism that give rise to light Majorana neutrinos is more appealing than others, but we shall remember that this is only one of the possible mechanisms that can generate neutrino masses.

1.4 Observables for $0\nu\beta\beta$ Searches

Two neutrinos double beta decay can be observed only in few nuclei. These are isotopes with even-even nuclei (even number of protons and even number of neutrons) for which single β decay is kinematically forbidden because the ground energy levels (A, Z) and (A, Z+2) are both below (A, Z+1). When this is the case, they can however decay transforming simultaneously two neutrons into two protons with the emission of two electrons and two electronic anti-neutrinos, namely by double beta decay whose Feynman diagram is shown in Figure (1.4.1) (left).

This is indeed a second order weak interaction process, implying that $2\nu\beta\beta$ decay is very, if not the most, rare: the half-lives of the various isotopes are in the range $(10^{19}$ - $10^{24})$ yr [14].

Already in 1930 Pauli postulated that, due to their kinematics, the energies of neutrinos coming from β decays are distributed in a continuous spectrum. For the same kinematical reason the footprint of $0\nu\beta\beta$ decay is a line rather than a continuous spectrum. Therefore, ignoring for a moment the energy resolution and background, what we seek to observe in a $0\nu\beta\beta$ decay experiment is a peak at the Q-value of the isotope of interest. Figure (1.4.2) represents a sketch of the signature we expect from this rare decay.

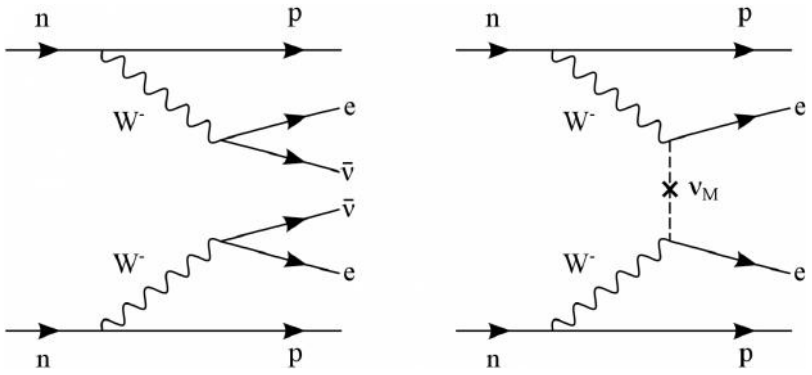

Figure 1.4.1: *Left: Feynman diagram of the $2\nu\beta\beta$ decay, a second order weak interaction process that transforms simultaneously two neutrons in two protons with the emission of two electrons and two electronic anti-neutrinos. Right: Feynman diagram of the hypothetical $0\nu\beta\beta$ decay with the exchange of a light Majorana neutrino (dotted line).*

1.4.1 $0\nu\beta\beta$ via exchange of Majorana neutrinos

In investigating the connection between $0\nu\beta\beta$ decay and neutrino masses, we will assume that this hypothetical decay takes place thanks to the exchange of a light Majorana neutrino, even if we can also allow the possibility of other new physics that violates the lepton number. In the following we will also take the reasonable assumption that neutrino masses are much smaller than the isotope Q-value ($Q_{\beta\beta}$).
Under these assumptions, $0\nu\beta\beta$ amplitude is proportional to the $\nu_L\nu_L$ element of the Majorana neutrino mass matrix of Equation (1.3.4), namely the effective Majorana mass $m_{\beta\beta}$. Thanks to this link, the decay rate (or equivalently the half-life), observable by the experiments, can be written in terms of the neutrino masses

$$\Gamma_{0\nu} = G^{0\nu}|M^{0\nu}|^2 \frac{\langle m_{\beta\beta}\rangle^2}{m_e^2} \qquad \rightarrow \qquad T^{0\nu}_{1/2} = \frac{ln2}{\Gamma_{0\nu}} \tag{1.4.1}$$

where m_e is the electron mass and $G_{0\nu}$ represents the number of ways the particles can share the kinetic energy in the final-state, namely the decay phase-space, which scales as the fifth power of $Q_{\beta\beta}$.
$M_{0\nu}$ in Equation (1.4.1) is the nuclear matrix element that accounts for the nuclear part of the decay, representing the transition from the initial nuclear state to the final nuclear state. In practise it represents the probability for every pair of neutrons in the nucleus to transition to protons through $0\nu\beta\beta$ decay. These nuclear matrix elements depend indeed on both the complicated structure of the nucleus and on the particular assumptions that we make when describing the neutrino interaction. Since the nuclei that can undergo

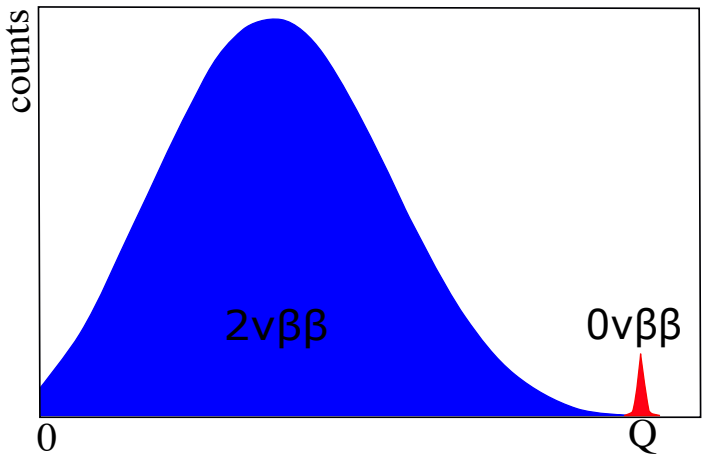

Figure 1.4.2: *Schetck of the spectrum of $2\nu\beta\beta$ decay in red and theoretical signature of $0\nu\beta\beta$ decay in green. Image from [15].*

$2\nu\beta\beta$ decay are typically very large, their description is rather complicated and the nuclear matrix elements cannot be calculated exactly. There are many techniques used to compute numerically the nuclear matrix elements, each one using different approximations. An example is the commonly used Quasiparticle Random Phase Approximation (QRPA) which sums many possible states of the nucleus in a limited number of shells; the Interacting Shell Model (ISM), which does the opposite, using only few nucleus states but summing on all the possible shell configurations; the Interacting Boson Model (IBM-II) and so on. The calculation of the nuclear matrix elements carries significant theoretical uncertainties and the various techniques can differ up to a factor of 10. Usually the nuclear matrix element is written by explicitly factorising out the axial coupling term g_A^2

$$M^{0\nu} = g_A^2 M^{0\nu} \tag{1.4.2}$$

In literature the standard value for the axial coupling term in free nucleons is $g_A \simeq 1.27$[16], which is the value that we will use in this Thesis. However, inside nuclear matter g_A might be affected by the correlation with the other nucleons. There are hints that this coupling could be quenched [17, 18], thus influencing the limits placed on $m_{\beta\beta}$.

For reference I report here the unitary neutrino mixing matrix [19, 20], parametrized by 3

angles 3 CP violation phases following the parametrization of [21, 22].

$$V = \begin{bmatrix} c_{12}c_{13} & s_{12}c_{13} & s_{13}e^{-i\delta} \\ -s_{12}c_{23} - c_{12}s_{23}s_{13}e^{i\delta} & c_{12}c_{23} - s_{12}s_{23}s_{13}e^{i\delta} & s_{23}c_{13} \\ s_{12}s_{23} - c_{12}c_{23}s_{13}e^{i\delta} & -c_{12}s_{23} - s_{12}c_{23}s_{13}e^{i\delta} & c_{23}c_{13} \end{bmatrix} \times diag\left(1, e^{i\frac{\alpha_{21}}{2}}, e^{i\frac{\alpha_{31}}{2}}\right) \tag{1.4.3}$$

where we use the compact notation c_{ij} to indicate $cos\theta_{ij}$ and s_{ij} to indicate $sin\theta_{ij}$ which we will continue to use in the subsequent steps.

The effective Majorana mass $m_{\beta\beta}$ can be explicitly broke up in terms of neutrino masses m_i, mixing angles θ_i and Majorana CP violation phases, where the index $i = 1, 2, 3$ runs over the neutrino mass eigenstates. In particular, since we only need the electronic elements of the mixing matrix, only the first row of the matrix in Equation (1.4.3) will be selected:

$$|m_{\beta\beta}| = |\sum_i V_{ei} m_i| = |c_{13}^2 \left(m_1 c_{12}^2 + m_2 s_{12}^2 e^{2\alpha_{21}}\right) + m_3 s_{13}^2 e^{i(\alpha_{31} - 2\delta)}| \,. \tag{1.4.4}$$

The three neutrino masses m_i can be expressed in terms of the measured oscillation parameters Δm_{21}^2 (solar) and Δm_{31}^2 (atmospheric) and in terms of the lightest neutrino mass. Depending on which neutrino mass eigenstate we choose to be the lightest, we will have Normal Hierarchy (NH) or Inverted Hierarchy (IH), and Quasi Degenerate (QD) spectrums. It became common to represent NH and IH in the neutrino mass parameters space $m_{\beta\beta}$ versus $m_{lightest}$

$$|m_{\beta\beta}| \simeq |\sqrt{\Delta m_{21}^2} s_{12}^2 c_{13}^2 + \sqrt{\Delta m_{31}^2} s_{13}^2 e^{i(\alpha_{31} - \alpha_{21} - 2\delta)}| \qquad \text{for NH} \,, \tag{1.4.5}$$

$$|m_{\beta\beta}| \simeq \sqrt{\Delta m_{23}^2 + m_3^2} \left(1 - sin^2 2\theta_{12} sin^2 \frac{\alpha_{21}}{2}\right)^{\frac{1}{2}} \qquad \text{for IH and QD} \tag{1.4.6}$$

where we have exploited the fact that $sin^2\theta_{13} \ll cos^2\theta_{12}$. You can see the two scenarios of Equation (1.4.5) and Equation (1.4.6) represented in Figure (1.4.3), where the former (NH) is depicted in red, while the latter (IH) is depicted in green. For each scenario of neutrino mass spectrum, the CP phases determine the intervals of possible values of $m_{\beta\beta}$ corresponding to each value of $m_{lightest}$, giving the width of the band.

In the non degenerate region, the NH and IH bands are clearly separate, therefore an experiment sensitive to $m_{\beta\beta}$ could confirm or discard one of the two scenarios in case the signature of $0\nu\beta\beta$ is observed. In the current situation in which no signal has ever been observed experiments can only set limits, thus slowly excluding regions of the parameters space.

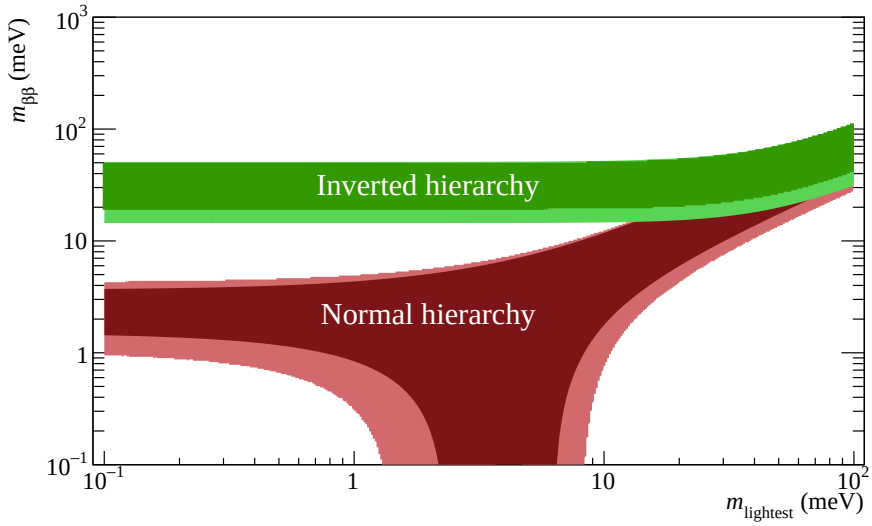

Figure 1.4.3: *Effective Majorana mass $m_{\beta\beta}$ as a function of $m_{lightest}$. The NH (red) and IH (green) separate scenarios are obtained using the current best fit on neutrino oscillation parameters, and the width of the bands are obtain by varying the CP phases in their full range.*

1.4.2 Why Improving the Limit on $0\nu\beta\beta$ is Difficult

Despite the huge experimental effort in developing techniques for $0\nu\beta\beta$ decay, in the last few decades the sensitivity of the experiments improved very slowly. In this Section we will investigate why it is so difficult to improve the limits on $0\nu\beta\beta$ decay.
We start considering the number of $0\nu\beta\beta$ events expected to be observed in an experiment, namely the number of signal events N_{sig}

$$N_{sig} = \mathcal{T} \cdot \Gamma_{0\nu} \cdot f \cdot N \cdot \varepsilon \tag{1.4.7}$$

where $\mathcal{T}$ is the live time of the experiment, $\Gamma_{0\nu}$ is as usual the decay rate of $0\nu\beta\beta$ decay, f is the fractional isotopic abundance of the isotope that undergoes $2\nu\beta\beta$ decay, N is the total atoms composing the target material of the experiment in object and $\varepsilon \leq 1$ is the efficiency in electron detection.
From Equation (1.4.7) it might seems that the experimental sensitivity is linearly dependent on the mass of active material and on the detection efficiency, thus improving those two factors is enough to improve the sensitivity. However in any real experiment we must consider the presence of background events in the signal energy region ΔE

$$N_{bkg} = \mathcal{T} \cdot \Delta E \cdot \frac{d\Gamma_{bkg}}{dE} \cdot N \tag{1.4.8}$$

where $\mathcal{T}$ is the live time of the experiment, $d\Gamma_{0\nu}/dE$ is the background rate per atom per energy interval and it is constant over the energy range considered, N is, like before, the number of total atoms in the detector.
Using the number of $0\nu\beta\beta$ events and the number of background events expected, we introduce a figure of merit F which has to be as large as possible for a successful experiment. We can think at F like the overall signal to noise ratio of the experiment. F is indeed the ratio of the number of expected signal events with the Poisson fluctuation of the background

$$F = \frac{N_{sig}}{\sqrt{N_{bkg}}} = \Gamma_{0\nu} \cdot f \cdot \varepsilon \cdot \sqrt{\frac{N \cdot \mathcal{T}}{\Delta E \cdot d\Gamma_{bkg}/dE}} \tag{1.4.9}$$

In few simple passages we can turn the number of atoms N in Equation (1.4.9) in a more friendly unit to describe the mass M of the detector material. In this way the background rate per atom per energy interval $d\Gamma_{0\nu}/dE$, becomes the background index b defined as the background rate per unit of mass per energy interval. At this point, in few trivial passages we obtain

$$T^{0\nu}_{1/2} \propto \frac{\mathcal{N}_A \cdot \varepsilon}{A} f \sqrt{\frac{M \cdot \mathcal{T}}{\Delta E \cdot b}} \tag{1.4.10}$$

showing that the half life of the $0\nu\beta\beta$ decay is proportional to the square root of the exposure $(M \cdot \mathcal{T})$ and inversely proportional to the square root of the background index and of the energy resolution. ΔE is not actually the energy resolution, but is the energy range where we expect to see the $0\nu\beta\beta$ decay signal, which in turn is strictly dependent from the energy resolution.
In conclusion, Equation (1.4.10) demonstrates why a big improvement for $0\nu\beta\beta$ decay experiments is so difficult. In fact, all the factors upon which experiments can act (mass, exposure time, energy resolution and background index) are under square root, thus in order to gain a factor 10 in sensitivity to the half life of the decay, one must build an experiment 10^2 times bigger without any worsening in energy resolution and background index.

1.5 Experimental Review

We have seen so far the importance of $0\nu\beta\beta$ decay search to shed light on the problems of leptogenesis and neutrino mass. From now I will focus instead only on the experimental point of view of this search.
All the experiments aiming to observe this rare decay, must have some common characteristics. In fact $0\nu\beta\beta$ decay is possible only for few isotopes and, if it exists, it has an half life

predicted to be more than 15 orders of magnitude above the age of the Universe. Therefore a common goal for all experiments is to have as many atoms as possible of the isotope that undergoes $2\nu\beta\beta$ decay. There are two possible strategies to overcome this need: big experimental mass, isotopic enrichment, or both in some cases. An other common goal is the suppression of possible sources of background: cosmic ray induced background is suppressed by placing the experiments in underground facilities, radioactive background from environmental contamination is controlled by extreme care in the selection of the construction materials of the experiment and by using any kind of stratagems to avoid any further contamination. Very popular is the use of veto systems to tag and eliminates contaminations coming from outer sources and particle discrimination in order to select only the interactions having the expected topologies. There is however a source of background that cannot be avoided by any mean: the intrinsic contamination of $2\nu\beta\beta$ events caused by the same isotope that undergoes $0\nu\beta\beta$ decay. The best strategy is having an energy resolution high enough to clearly discriminate the two signals. However, not all the detection techniques allow to have such high energy resolution: in this latter case the only way to isolate the possible $0\nu\beta\beta$ signal is by statistical subtraction of the background which implies the use of Monte Carlo simulations and a deep understanding of the background model of the experiment.

In this last part of the first chapter, I will briefly review few experiments which use different $0\nu\beta\beta$ decay source as well as different techniques to detect it. Each one has its own strategy to solve the issues just mentioned, however it is easy to notice some similarities in background control strategies and analysis techniques. Of course these are just some among the many experiment that have been taking data or that are currently in operation. However these are the experiments that set so far the best limit on their element of interest and at the end of this work of Thesis I will compare our result, in the scenario of light Majorana mass mechanism, with theirs.

First I will review the GERDA[23] experiment that is somehow the most similar to CUORE, whose major strength is the pulse shape discrimination and the excellent energy resolution; then I will talk about an experiment completely different, having a structure resembling a classic neutrino detector and which relies on its huge mass of active material: KamLAND-Zen[24]. The last one is the NEMO-3[25] experiment, ended in 2010, whose primary characteristic is the ability for a 3D reconstruction of the particle track, thus a very high particle discrimination.

GERDA

GERDA stands for GERmanium Detector Array. It is an experiment located underground at Laboratori Nazionali del Gran Sasso (LNGS) operating bare germanium detectors in liquid argon. GERDA searches $0\nu\beta\beta$ decay from ^{76}Ge, whose Q-value is (2039.061 $\pm$ 0.007) keV. It deploys 37 enriched detectors up to a ^{76}Ge isotopic abundance of 87%, for a total mass of 35.6 kg: 7 coaxial detectors from previous experiments and 30 broad energy detectors, also called BEGe. The detectors are arranged in 6 strings surrounding a central string of 3 coaxial detectors with natural isotopic composition. The strings hang inside a cryostat filled with 64 m^3 of liquid argon which is in turn immerse in a 590 m^3 water tank. The water tank, instrumented with 66 Photo Multiplier Tubes (PMTs), and an array of plastic scintillators placed on top of the experiment compose the muon veto. The liquid argon has the double role of keeping the detectors at low temperature and working as a veto. In fact, the strings of detectors immerse in liquid argon are surrounded by a cylinder instrumented with PMTs and optical fibers connected to SiPMs. The detector strings are protected by a nylon shield in order to keep free ions in the liquid argon far from the surface of the detectors. All the surfaces within the instrumented cylinder are covered by wavelength shifter to shift the argon scintillation light to the quantum efficiency peak of the PMTs. A schematic drawing of the GERDA detector is shown in Figure (1.5.1). In order to obtain the correspondence between the measured signal and the energy, once a week the detectors are calibrated with a ^{228}Th source.

The GERDA latest published result asses an energy resolution at 2.6 MeV between 2.6-4.0 keV Full Weight Half Maximum (FWHM) for BEGe and 3.4-4.4 keV FWHM for coaxial detectors. In the data analysis all events that are in coincidence with signal in the veto within a short time window (depending on the characteristics of the detector considered) are rejected. In addition, the time profile of the germanium detector signal is used to eliminate undesired background through pulse shape discrimination techniques.

They perform both a Frequentist and Bayesian analysis based on an unbinned extended maximum likelihood, modelling the region of interest around the Q-value as a flat background and a gaussian peak for the hypothetic $0\nu\beta\beta$ decay signal. The Frequentist analysis yield a limit on the ^{76}Ge $0\nu\beta\beta$ decay half life of $T^{0\nu}_{1/2}$ >5.3·10^{25} yr at 90%C.L., corresponding to a limit on the effective Majorana mass of $m_{\beta\beta}$ <150-330 meV depending on the nuclear matrix element used.

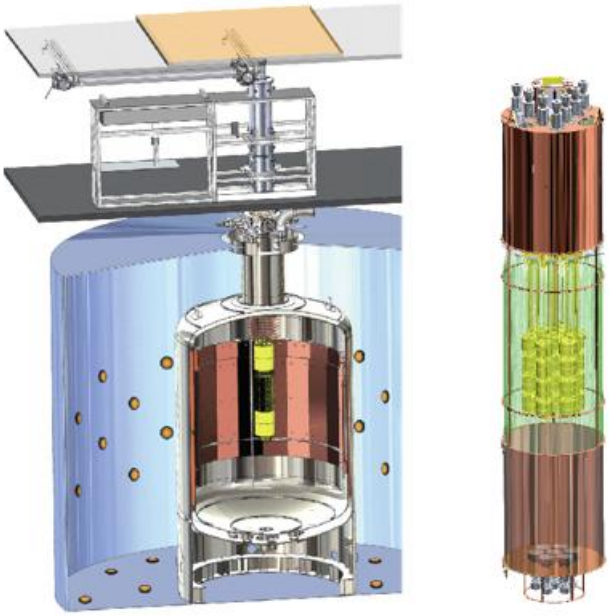

Figure 1.5.1: *Scheme of the GERDA structure adapted from [23]: the drawing on the left is a rendering of the instrumented water tank, with inside the cryostat containing the liquid argon. On top of the water tank there is a clean room with glove box and an array of plastic scintillators. The inner part of the detector is represented on the right with the germanium detectors at the center of an instrumented cylinder surrounded by a curtain of wavelength shifting fibers.*

KamLAND-Zen

KamLAND-Zen searches $0\nu\beta\beta$ decay from ^{136}Xe. It uses the infrastructure of the former experiment KamLAND[26], located underground, exploiting its high radio-purity. KamLAND-Zen consists in 13 tons of Xe-loaded scintillator, where the xenon is for the majority ^{136}Xe with some residuals of other isotopes. The active material is hosted in a 3.08 m diameter transparent nylon balloon at the center of a second, much bigger nylon balloon filled with 1 kton of liquid scintillator which act as an active shield being continuously monitored by 1879 PMTs (see Figure (1.5.2)). The entire spherical structure hosting the balloons is placed in an instrumented water tank acting as muon veto. Initially the experiment had contamination problems caused by ^{110m}Ag, but after a period of repetitive cycles of purification of the liquid scintillator they succeeded in reducing the silver contamination by a factor of 10.

The ^{136}Xe $0\nu\beta\beta$ decay Q-value is at 2458 keV, therefore any contamination in this region of the spectrum must be either suppressed or well modelled. The analysis of the data

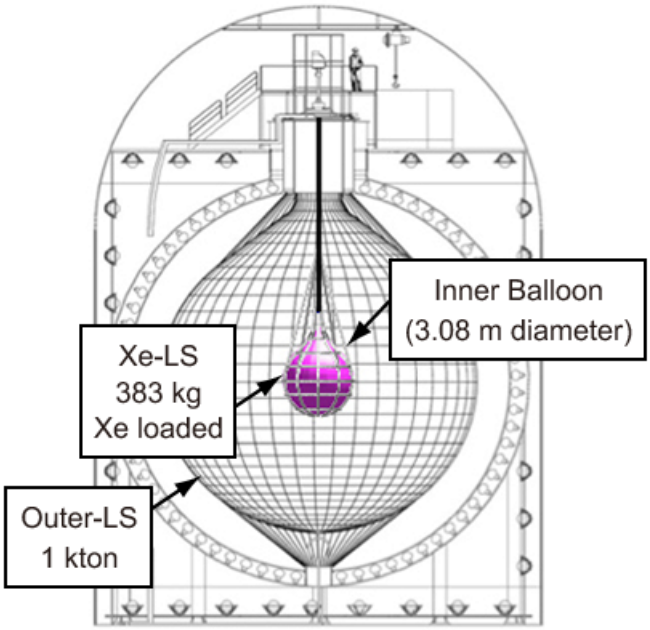

Figure 1.5.2: *Schematic structure of the KamLAND-Zen experiment where it is highlighted in magenta the volume of Xe-loaded scintillator where the active material is concentrated; all outer layers act instead as active shields. Figure taken from [27].*

from 534.5 days of live time highlighted a radioactive contamination of the inner balloon surface due mostly to ^{214}Bi, a daughter of ^{238}U, and to ^{134}Cs, caused by the fallout from the Fukushima-I reactor accident in 2011. The background for these as well as other radioactive contaminations are removed by both fiducializing the volume of active material and by studying the topology of the events such as ^{214}Bi-Po or neutron captures on hydrogen and carbon. The observed resolution of the KamLAND-Zen experiment at 2615 keV is 227.4 keV FWHM, hence this experiment has to rely on the good knowledge of its background and on the precision of the Monte Marlo simulation in order to extract a limit on $0\nu\beta\beta$ decy of ^{136}Xe. Thanks to its huge mass, namely 138 kg·yr of exposure, in the last publication KamLAND-Zen obtained an half life limit for ^{136}Xe $0\nu\beta\beta$ decay of $T^{0\nu}_{1/2} > 1.07 \cdot 10^{26}$ yr at 90%C.L. including systematics and fitting the data simultaneously in different geometrical regions of the balloon to account for the non-uniform background both radially and vertically. Considering the usual variety of nuclear matrix elements, this lower limit corresponds to an upper limit on the effective Majorana neutrino mass in the range $m_{\beta\beta}$ <61-165 meV.

NEMO-3

The NEMO-3 was a $0\nu\beta\beta$ decay experiment operated from 2003 until 2010 in the Modane Underground Laboratory. Differently from the experiments described so far, NEMO-3 has the peculiarity of measuring $2\nu\beta\beta$ decay and searching for $0\nu\beta\beta$ decay of seven different isotopes, in the form of thin foils. The longest data taking was with 6.914 kg of ^{100}Mo which has a Q-value of (3034.40 $\pm$ 0.17) keV. The foils are suspended in a cylindrical structure surrounded first by 6180 drift cells operated in Geiger mode and then, in the most external part of the detector, by a calorimeter made of plastic scintillators coupled with PMTs. The entire structure is immerse in a 25 G magnetic field. Such a detector allows to reconstruct the full topology of the events and, at the same time, to measure their energy as shown in Figure (1.5.3). NEMO-3 can thus reject the background and selecting the $2\nu\beta\beta$ and $0\nu\beta\beta$ candidates by identifying electrons, positrons, γ rays, and α particles. Pair production is identified by mean of the curvature of the tracks.
The energy is calibrated every three weeks with ^{207}Bi. This detector yields an energy resolution of 14-17%/$\sqrt{E(MeV)}$[2] FWHM and a timing resolution of 250 ps.

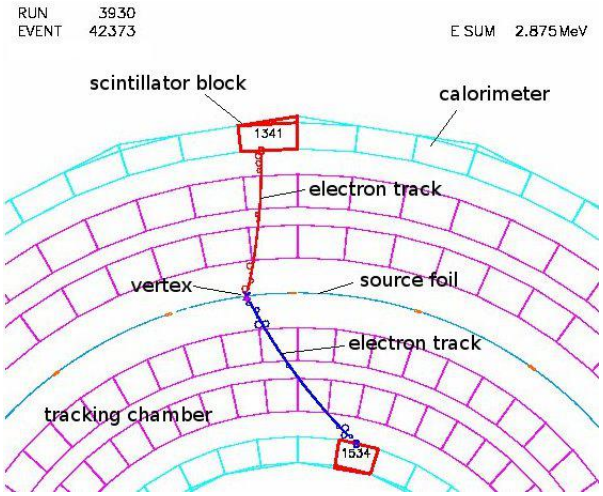

Figure 1.5.3: *Scheme of part of the NEMO-3 (view from the top) showing a $0\nu\beta\beta$ decay candidate event. The trajectory of the electrons is reconstructed thanks to the Geiger signals extracted from the drift cells (depicted in magenta); the curvature of the two tracks in the magnetic field shows that the event is compatible with electrons coming from the source foil. The scintillators (in cyan) measure a total energy deposit of 2875 keV, consistent with what is expected for a $0\nu\beta\beta$ decay of ^{100}Mo nucleus if corrected by energy loss in the source foil. Image from [28].*

[2]For a comparison with the other experiments, the FWHM resolution at 2615 keV is between 226.4 keV and 274.9 keV.

The main sources of background for the $0\nu\beta\beta$ decay search are $2\nu\beta\beta$ ^{100}Mo decay events and radioactive decays from ^{238}U and ^{232}Th chains, especially ^{222}Rn. This last isotope is in secolar equilibrium with ^{214}Bi which is easily recognizable from the $\alpha - \beta$ cascade of the ^{214}Bi-Po decay. An other important source of background are (α,n) reactions whose effect has been studied with an Am-Be dedicated calibration. The NEMO-3 background model has been verified using other sectors of the cylinder with foils of copper and ^{130}Te. The $2\nu\beta\beta$ background to $0\nu\beta\beta$ has been taken into account by fitting the $2\nu\beta\beta$ decay spectrum.
In conclusion, with an exposure of 34.7 kg·yr, NEMO-3 set a limit on the half life for $0\nu\beta\beta$ decay of ^{100}Mo of $T^{0\nu}_{1/2} > 1.1 \cdot 10^{24}$ yr at 90%C.L. In the scenario of light Majorana neutrino mass mechanism this limit corresponds to an upper limit on the effective Majorana mass in the range $m_{\beta\beta}$ <300-900 meV, depending on the choice of the nuclear matrix elements.

1.5.1 Comparing the Sensitivity of Different Experiments

Despite the few points in common, so far we saw how different experiment searching for $0\nu\beta\beta$ are: each one searches for this rare decay in a different isotope and uses different techniques. However at the end their results are always expressed in terms of half life or equivalently in terms of the limit on the decay rate of the isotope of interest. In Equation (1.4.1) we saw how the $0\nu\beta\beta$ decay rate $\Gamma_{0\nu}$, observable by the experiments, can be expressed in terms of the effective Majorana mass $m_{\beta\beta}$, thus the parameter space of Figure (1.4.3) is used by different experiments as a confrontation field. In fact the limit on the $0\nu\beta\beta$ decay rate $\Gamma_{0\nu}$ can be transformed in a range of tested values of $m_{\beta\beta}$. Note that due to the inconsistency of the different theoretical models for approximating the nuclear matrix elements, and due to their big theoretical uncertainties we must consider the full available range of nuclear matrix elements present in literature.
For each limit on the $0\nu\beta\beta$ decay rate $\Gamma_{0\nu}$ of the experiments presented in this Section, we can visualize the results in bands across the parameter space $m_{\beta\beta}$ versus $m_{lightest}$, as shown in Figure (1.5.4).
Finally, at the end of this work of Thesis I will report the results obtained by the CUORE experiment on the $0\nu\beta\beta$ decay of ^{130}Te on this same parameter space.

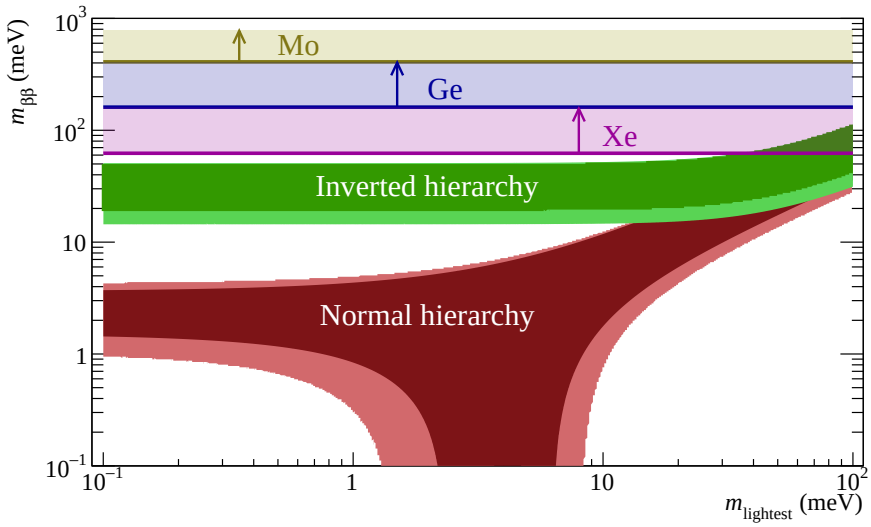

Figure 1.5.4: *Effective Majorana mass $m_{\beta\beta}$ as a function of $m_{lightest}$. The red and green bands represent respectively the NH and IH mutual excluding scenarios. The yellow band represent the lower limit set on the ^{100}Mo $0\nu\beta\beta$ decay by the NEMO-3 experiment [25]; the blue band represent the latest results on ^{76}Ge set by the GERDA experiment [23]; the magenta band represent the latest limit set on ^{136}Xe by the KamLAND-Zen experiment [24].*

Chapter 2

CUORE

2.1 Introduction to the CUORE experiment

CUORE is the name of the experiment object of this work of Thesis, but the name by itself does not tell much. CUORE is the first ton-scale bolometric detector designed to search for $0\nu\beta\beta$ decay. It is in operation since January 27^{th} 2017 and currently taking data at LNGS in Assergi (AQ), Italy, since April 2017.

The CUORE project began in 1991, within the experimental group held by E. Fiorini, with the first γ-ray spectroscopy measurements performed using 5.7 g and 20.9 g of TeO_2 crystals [29]. These firsts measurements already showed the great potential of the bolometric technique with TeO_2 crystals. The subsequent developments of this technology have been focusing on three complementary directions: increasing the mass, reducing the radioactive background and improving the energy resolution. The success of these developments lead in 1997 to the proposal, by E. Fiorini, for "an array of 1000 cryogenic detectors of a mass between 0.5 and 1 kg each" devoted to build an experiment "to search for neutrinoless double beta decay, interactions of WIMPS and of solar axions and for rare events in nuclear physics" [30]. After 20 years of continuous work, the CUORE experiment is now operational and taking data. Its first physics results are reported in this work of Thesis.

The general approach of any kind of $0\nu\beta\beta$ search is to compile the decay spectrum of the observed $\beta\beta$ emitter isotope and to identify a possible excess of events around the Q-value. In Table (2.1.1) we report the isotopes undergoing double beta decay. In the CUORE case ^{130}Te was chosen because of the high isotopic abundance of 34.167% [31], that allows to gather the desired quantity of ^{130}Te using natural tellurium, without resorting to the expensive and risky (because of the introduction of possible contaminants) isotopic enrichment. In addition ^{130}Te has a Q-value of (2527.515 ± 0.013) keV [32, 33, 34] ($Q_{\beta\beta}$)

which is above most of the prominent γ-lines due to environmental radioactivity, but below the 2615 keV γ line from ^{208}Tl .

$\beta\beta$ Decay Reaction	Isotopic Abundance (atomic %)	Q-value (keV)
^{48}Ca$\rightarrow^{48}$Ti	0.2	4274
^{76}Ge$\rightarrow^{76}$Se	7.6	2039
^{82}Se$\rightarrow^{82}$Kr	8.7	2996
^{96}Zr$\rightarrow^{96}$Mo	2.8	3348
^{100}Mo$\rightarrow^{100}$Ru	9.6	3034
^{116}Cd$\rightarrow^{116}$Sn	7.5	2814
^{124}Sn$\rightarrow^{124}$Te	5.8	2288
^{128}Te$\rightarrow^{128}$Xe	31.8	866
^{130}Te$\rightarrow^{130}$Xe	**34.2**	**2528**
^{136}Xe$\rightarrow^{136}$Ba	8.9	2458
^{150}Nd$\rightarrow^{150}$Sm	5.6	3368

Table 2.1.1: *Isotopes that are $\beta\beta$ emitters with the corresponding isotopic abundance and endpoint of the $\beta\beta$ spectrum (Q-value). Both the abundances and the Q-values are from [35]. The isotope underlined in bold, ^{130}Te , is the one chosen for the CUORE experiment.*

Experiments searching for rare events, such as CUORE, must be located underground to mitigate the irreducible background due to "cosmic rays". CUORE is indeed situated in Hall A of LNGS underground laboratories (Figure (2.1.1)), shieled by 1400 m of rock (3600 meters of water equivalent), mostly of calcareous composition, that belongs to the Gran Sasso mountain, located in central Italy (Assergi, Abruzzo). The special environment provided by LNGS suppresses the cosmic ray flux by six orders of magnitude, strongly reducing the related background due to spallation products and cosmogenic activation.
A comparison of the background conditions on the surface and underground at LNGS is presented is in Table (2.1.2).

Background source	Flux at surface (m^{-2} h^{-1})	Flux at LNGS (m^{-2} h^{-1})	Reference
μ	$3.1 \cdot 10^6$	$\sim$1.08	[36, 37]
$n < 10$ MeV	$5 \cdot 10^4$	$\sim$144	[38, 39]
γ		$\sim 2.6{\cdot}10^7$	[40, 41]

Table 2.1.2: *Comparison between background a the surface and underground at LNGS.*

The sensitivity for experiments searching $0\nu\beta\beta$ decay, is defined as the half life of the particular decay, object of the study, corresponding to the minimum number of counts

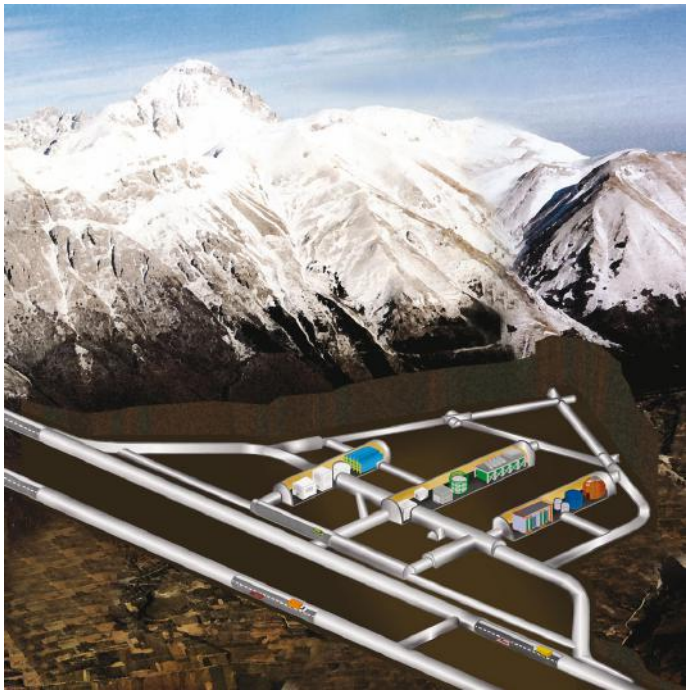

Figure 2.1.1: Sketch of the underground laboratory (LNGS) situated under the Gran Sasso mountain. The core of the laboratories are the three halls where the experiments are situated called A,B and C: CUORE is situated in Hall A. The entrance and exit to the underground laboratories is connected to the highway tunnel, thus the only link to the outside world.

observed above the background at a given Confidence Level (C.L.). We can assume it scales with the total mass of the detector, hence from what we already derived in Equation (1.4.10) we can write the sensitivity as

$$S^{0\nu}(n_\sigma) = \frac{ln2}{n_\sigma}\epsilon\mathcal{N}_a\frac{f}{A}\sqrt{\frac{M\cdot\mathcal{T}}{\Delta E\cdot b}} \tag{2.1.1}$$

where n_σ is the number of sigma considered.
We can infer from Equation (2.1.1) that an experiment must have a large mass and take data for a long time, and at the same time it must have a low background and a good energy resolution.
To meet these requirements CUORE foresees 5 years of data taking with a detector of 742 kg of TeO_2 , an energy resolution of 5 keV FWHM at $Q_{\beta\beta}$ and a background index of 0.01 counts/keV/kg/yr [42].
The 742 kg of TeO_2 consists in 988 crystals, each one with dimension of 5×5×5 cm and weight 750 g, giving 206 kg of ^{130}Te active material. The crystals are grouped in 19 modular

structures, called *towers*, held together by a copper frame; each tower is divided in 13 floors hosting 4 crystals each.
The CUORE requirements in terms of background, uniformity and energy resolution were tested on a single CUORE-style tower called CUORE-0 [43, 44, 45], which ran from March 2013 to March 2015 as a stand-alone experiment. CUORE-0 validated the assembly line [46] for the towers and proved that the CUORE goal, in terms of low background and good energy resolution, was possible.

1. CUORE-0 measured a background index in the ROI of (0.058 ± 0.004 (stat) ± 0.002 (syst)) counts/keV/kg/yr - mostly due to residual cryostat contaminants [1] [47]), showing that the CUORE goal is within reach. The background measured by CUORE-0 is expected to improve in CUORE, since all the materials used to build the cryostat infrastructure had to accomplish more stringent radio-purity criteria and underwent additional and enhanced cleaning procedures with respect to CUORE-0. Moreover, the CUORE cryostat has been equipped with a better shielding from environmental background, from both the underground rocks and cryostat radioactivity.

2. Thanks to the CUORE-0 experiment, the energy resolution was proven to be (5.1±0.3) keV FWHM at 2615 keV. A good energy resolution is crucial for separating the $0\nu\beta\beta$ signal from the irreducible background coming from $2\nu\beta\beta$ decays, even in the zero background hypothesis.

In conclusion CUORE complies all the three above mentioned essential qualities - big mass, low background level and good energy resolution - to build a competitive $0\nu\beta\beta$ decay experiment.
This Chapter is dedicated to the description of the CUORE detector and its working principle. For a better understanding of the subsequent Chapters I will also discuss the full data taking process, from the raw signals of the bolometers to the triggered data, ready to be analyzed.

2.2 Bolometer Technique

CUORE uses the bolometric technique to detect particle interactions in the TeO_2 crystals. Bolometers are calorimeters working at very low temperatures, in which the energy

[1] Contaminations in the CUORE-0 cryostat do not affect background budget since for CUORE there is a new bigger and cleaner cryostat.

deposited by particles is converted into phonons and is thus measured as temperature variations. Some kinds of detector, such as scintillators, loose part of released energy into heat and ionization channels. The bolometric technique has instead the advantage of converting a considerable fraction of the released energy into phonon excitation. Bolometric detectors have indeed a better intrinsic energy resolution, but on the other hand these kind of detectors have a very slow response and hence they are suitable only for experiments where the signal event rate does not exceed few tens of milliHertz, such as rare event searches. Another drawback is the necessity to operate the detectors at milliKelvin temperatures, for reasons that will become clear in the following.

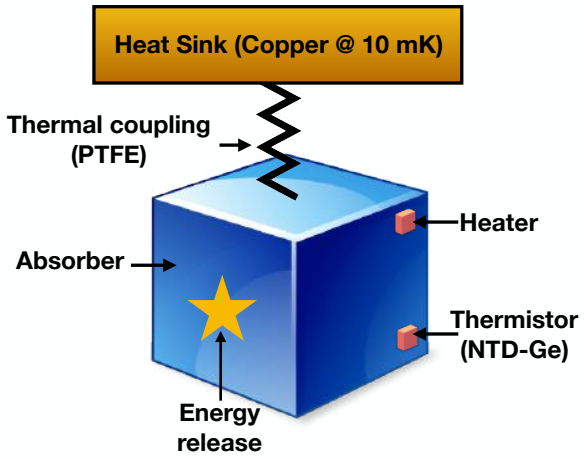

Figure 2.2.1: *Schematic drawing of the main components of a CUORE bolometer: the crystal is the absorber and attached to it there is a sensor, an NTD-Ge thermistor, and a silicon heater; the bolometer is weakly coupled to the heat sink at 10 mK by PTFE holders.*

Figure (2.2.1) represents a schematic drawing of a CUORE bolometer. The cubic TeO_2 crystal conveniently is at the same time the source of the $\beta\beta$ emitter and the energy absorber of the bolometer. The sensor is a thermistor based on doped semiconductor, namely an NTD, that converts the energy into a measurable signal. The sensors are glued on the crystal by mean of 9 spots[2] of Araldit Rapid Epoxy glue to guarantee a low failure rate during cool down. In fact the glue spots prevent the crystal and the thermistor to crack during the cool down, event that could happen due to the different thermal contraction of the glue with respect to the crystal and the NTD. The glue is posed by a mechanic arm that allow to deposit the glue always in the same position and in the same amount:

[2]The glue spots are 0.5 mm in diameter and 50 μm in thickness.

this is crucial to guarantee uniformity of the thermal capacitance and resistivity for all the detector sensors. The second chip glued on the absorber is a silicon heater[3], strongly doped with a resulting resistance between 50 and 100 kΩ. These are used as Joule heaters and designed to periodically[4] provide a tuneable amount of energy in the detector for gain stablization purposes. The two chips glued on the crystals, the NTD and the silicon heater, are shown in Figure (2.2.2) (left). The crystal is maintained in its position in the tower by mean of eight PoliTetraFluoroEthilene (PTFE) [5] holders, one on each corner of the TeO_2 cube: the PTFE has the double effect of mechanically tightening the bolometers to the frame and to act as a weak thermal link to the heat sink. The entire support structure of the CUORE tower is made out of Electronic Tough Pitch (ETP1) copper alloy with a very low radioactive content, usually called NOSV Cu. This copper offers a remarkably high thermal conductivity so that it acts as heat sink at the base temperature of about 10 mK. The PTFE holders and the copper frame are shown in the picture of Figure (2.2.2) (right), captured during the towers assembly.

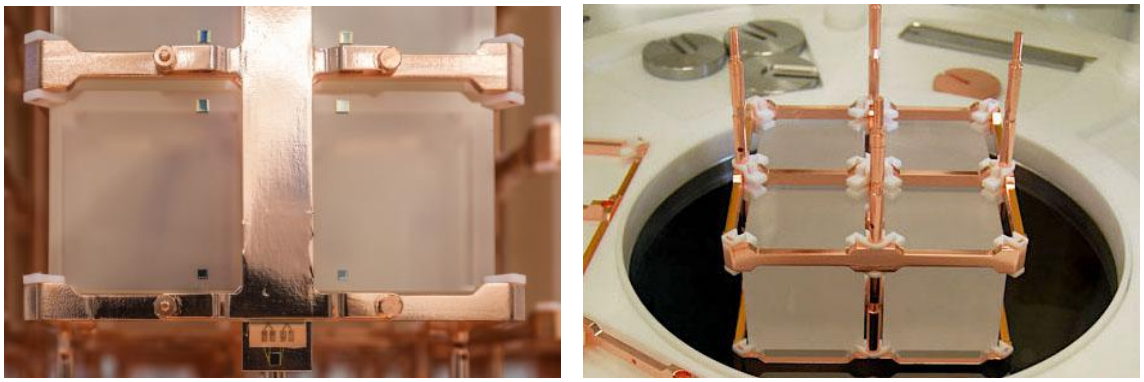

Figure 2.2.2: *Pictures showing the CUORE crystals. Left: if you focus on the bottom right crystal, the silicon heater is the chip on the bottom and the NTD is the chip on the upper left part of the crystals. Right: picture taken during the assembly of the towers where it is visible the structure of the copper frame and the white PTFE holders.*

[3]The size of this chip is $2.33 \times 2.40 \times 0.52\,\mathrm{mm}^3$.

[4]Heater pulsers are released to one column at the time with few seconds of delay between towers. There are 4 columns for each tower and 19 towers in total, so the periodicity of the pulser is usually of the order of several minutes.

[5]PTFE is also known under its commercial denomination of "Teflon", name given by Kinetic Chemicals when this product was patented in 1941.

2.2.1 Absorber

In a simplified model the absorber has a heat capacity C and it is connected to a heat sink at temperature T_0 through a conductance K. In this framework the temperature variation induced by a particle releasing an energy E in the crystal can be written as

$$\Delta T = E/C \, . \tag{2.2.1}$$

The heat then flows through the thermal conductance to the heat sink until the absorber returns in its initial equilibrium. If we assume a temperature variation much smaller than the temperature of the heat sink,

$$\Delta T(t) \equiv |T(t) - T_0| \ll T_0 \quad \forall t \tag{2.2.2}$$

where T(t) is the absorber temperature as function of time, C and K can be considered constant in time. Regardless of the description of the rising edge, in this simplified model the time evolution of the signal (represented in Figure (2.2.3)) is well approximated by a single[6] exponential decay as follows:

$$\Delta T(t) = \frac{E}{C} \cdot e^{-t/\tau} \tag{2.2.3}$$

where $\tau = C/K$ is the decay time of the bolometer signal and can range from few milliseconds up to several seconds depending on the heat capacity and conductance values.
From Equation (2.2.3) it is obvious that in order to have a detectable signal, the absorber must have a small heat capacity. For TeO_2 crystals, the main contribution to C is given by the crystal lattice, thus we can use the Debye low for the specific heat at low temperatures, from which we can extract

$$C \propto \left(\frac{T}{\Theta_D}\right)^3 \tag{2.2.4}$$

where Θ_D is the Debye temperature of the material. Now it is evident that in order to maximize the increase in temperature, or rather the signal itself, we must run the experiment at very low temperatures. Nevertheless the rise in temperature is still very small. Considering that typical values for the heat capacity of a CUORE crystal at 10 mK are measured to be around 10^{-9} J/K, the temperature rise for a 1 MeV energy release in the absorber is estimated to be about 100 μK.

[6] In reality we need more than one decay constant to better describe the decay of the pulse to base temperature.

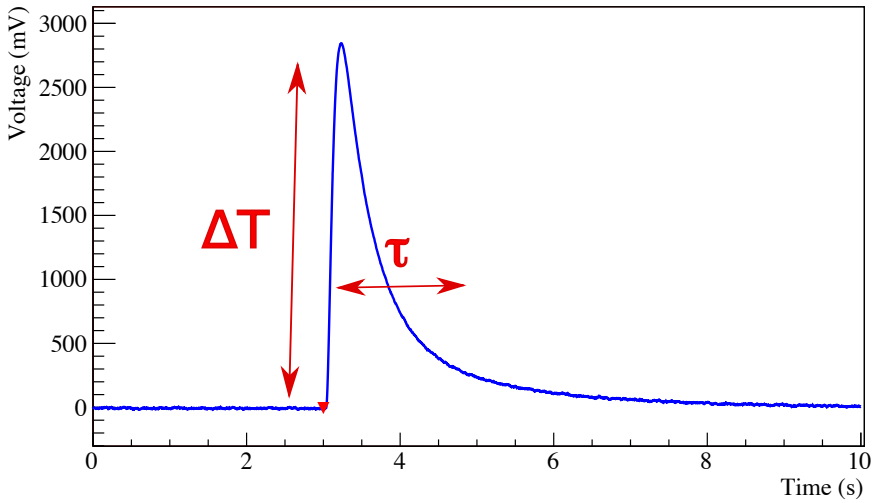

Figure 2.2.3: *Rapresentation of a CUORE signal induced by particle interaction. From left to right the two red harrows indicate respectively the hight of the signal as the temperature rise in the bolometer, proportional to the energy released int the absorber, and the time constant of the bolometer upon which depend the decay time, hence the length of the signal.*

Particles can interact in the absorber by scattering on nuclei or electrons: in both cases the energy is converted into phonons. When a particle interacts with the nuclei of the crystal lattice, it causes vibrational excitation as well as possible damages to the lattice structure, creating irregularity that could worsen the energy resolution. When a particle interacts with the electrons of the absorber, it quickly slows down, traveling only few micrometers for heavy particles like αs and few millimetres for electrons. In this picture phonons are produced in the interaction of electron-hole pairs formed in the lattice. Also in this case there might be a loss in energy resolution due to missing detection of the electron-hole pair interaction.
We can now roughly estimate the intrinsic energy resolution, making the hypothesis that all the thermal phenomena are detected. If the energy in the absorber is $E = C(T) \cdot T$, we can write this quantity in terms of the energy of each single phonon ($\varepsilon = K_B T$). Since the total number of phonons depends on the Poisson statistics we can write the uncertainty on the energy as

$$\Delta E = \Delta N \cdot \varepsilon = \xi \sqrt{K_B T \cdot C(T) \cdot T^2} \tag{2.2.5}$$

where ΔN is the uncertainty on the number of phonons generated in the interaction and ξ is a dimensionless factor depending on the detector details. Using the typical value for

CUORE crystals C=10^{-9} J/K, the intrinsic energy resolution is

$$\Delta E \simeq \sqrt{1.38 \cdot 10^{-23} \frac{J}{K} \cdot 10^{-9} \frac{J}{K} \cdot 10^{-4} K^2} \cdot 6.24 \cdot 10^{18} \frac{eV}{J} \simeq 10\, eV \tag{2.2.6}$$

where $6.24{\cdot}10^{18}$ eV/J is the electronVolts to Joules conversion factor. This equation shows that the intrinsic energy resolution of the bolometric technique is excellent. The broadening of the peaks in the energy spectrum due to the statistical fluctuations in the phonon population is negligible when compared to the noise contributions coming from cryogenic apparatus and the readout electronics. These additional sources of noise dominate the energy resolution and spoil it up to values of the order of few keV at 1 MeV. Potentially, when keeping these sources of noise under control, the bolometric technique allows to push the energy resolution down to few tens of eV.

2.2.2 Sensor

As a rule of thumb, the sensors used in this field convert temperature variations into electric resistance variations of the sensor itself. There are two possible kind of thermistors[7] that can be used for our scope: Transition Edge Thermistors (TES) and Semiconductor Thermistors (ST). The former are superconductive films with a fast response (order of microseconds), but they can work only in a very narrow temperature range and therefore they have not been chosen for CUORE. We use instead the latter: they have a slower response (order of milliseconds), but they can be used in a wider temperature range. The feature we look for in a thermistor is the steepness of the resistance slope as a function of temperature. The figure of merit used to characterise these thermistors is the sensitivity η, whose expression is

$$\eta = \left| \frac{dlogR(T)}{dT} \right| \quad \Rightarrow \quad \frac{dR}{R} = \eta \frac{dT}{T} \, . \tag{2.2.7}$$

The bigger is η, the better is the detector response. Typical values for TES and ST are 100 and 10 respectively, however CUORE chose to use ST even if less sensitive, because of their wider range of working temperatures, hence their flexibility in operation conditions.

In general semiconductors at room temperature behave as insulators because the valence band is full and the conductive band is empty. The gap between the two bands is about 2 eV (room temperature is K_BT=0.025 eV), therefore the conduction can happen only at high temperatures. However if the semiconductor has some impurities (is doped) other

[7] See reference [48] for a full review on phonon sensors.

valence levels are created just below the conductive band and the conduction can happen also at low temperatures. The dopant concentration determines the behaviour of the sensor and there is a critical concentration at which the semiconductor passes from insulator to metal behaviour, called Metal-Insulator Transition (MIT) region. In this region the material resistivity is highly dependent from the operational temperature. In particular, at temperatures below 10 K the conduction is dominated by the migration of the charge carriers between two different impurity sites, without using the conduction band. This migration is possible thanks to the tunnelling effect through the potential wall that separates the dopants sites (hopping mechanism). The charge carriers are activated by the incoming phonons from the absorber. If the dopant concentration is lower than a critical value, lowering the temperature results in an even stronger dependence of the thermistor resistivity on the temperature. By getting close to the Fermi level, charge carriers can travel longer distances and migrate not only between nearby impurity sites, but also to far sites. This is called the Variable Range Hopping (VRH) regime. In this regime the resistivity of the sensor obeys the following temperature dependence:

$$\rho(T) = \rho_D \cdot e^{(T_D/T)^\gamma} \tag{2.2.8}$$

where ρ_D and T_D are respectively the resistivity of the semiconductor and a temperature parameter, both dependent on the doping level. In our case we can fix the value for γ to 0.5 [49] and given that ρ_D and T_D depend from the dopants concentration, we get a sensitivity of

$$\eta = \frac{dlogR(T)}{dT} = \gamma \cdot \left(\frac{T_D}{T}\right)^\gamma. \tag{2.2.9}$$

In particular for CUORE were chosen NTD [50] Germanium thermistors, doped to the VRH regime. NTDs are made from Germanium wafers 0.9 mm thick, bombarded with a thermic neutron beam: neutrons induce nuclear reactions, creating as donors Arsenic and Selenium atoms, and as acceptors Gallium atoms. The wafers are finally cut into small pieces of dimensions $3.0 \times 2.9\,\mathrm{mm}^2$, forming the NTDs. The resultant resistance is

$$\begin{gathered} R = R_D \cdot e^{(T_D/T)^\gamma} \\ where \quad R_D = \rho_D \cdot \frac{l}{S} = 1.15\,\Omega\,, \quad T_D = 3.35\,K\,, \quad \gamma = \frac{1}{2}\,. \end{gathered} \tag{2.2.10}$$

The static resistance that one obtains with these values is

$$R_S = 100\,M\Omega \quad at \quad T_S = 10\,mK \tag{2.2.11}$$

and the sensitivity computed from Equation (2.2.9) results slightly higher than 9. On the upper face of the NTD and along the sides, there are two gold pads used to bond the golden wires connecting the sensor to the bias circuit, thus used to read the signal. Figure (2.2.4) shows two pictures of the NTD: on the left there is a close up of an NTD where the gold pads are visible while on the right there are 4 NTDs bonded to the strips that bring the signal outside the cryostat.

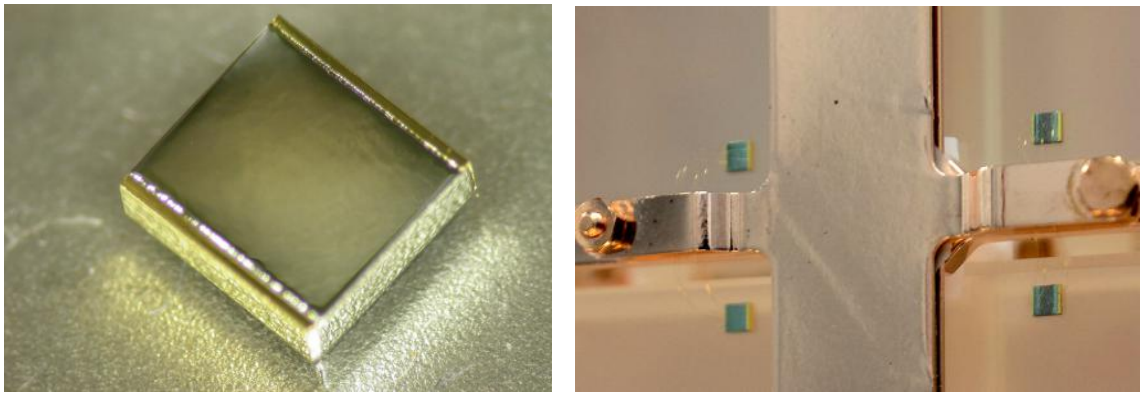

Figure 2.2.4: *Left: close up of a CUORE NTD where you can see the two golden pads along two opposite sides of the chip. Right: NTDs glued on the crystals and bonded to the strips through golden wires.*

2.2.3 Detector Operation

When a particle releases energy in the absorber, the phonons created in the lattice cause a reduction in the NTD resistance. This resistance variation can be measured if the thermistor is biased with a circuit illustrated in Figure (2.2.5), where the thermistor is represented by $R_{BOL}(T)$.
On top of the NTD surface are bonded two golden wires used to apply to the thermistor a small current I_B. The bias voltage V_B is produced by a generator closed on a load resistance R_L, in series with the thermistor. The load resistance must be chosen much higher (few order of magnitude higher) than the thermistor resistance so that R_{BOL} can be neglected when compared to R_L and the bias current $I_B = V_B/R_L$ is nearly constant. The voltage on the two edges of the NTD is therefore proportional to the thermistor resistance

$$V_{BOL}(T) = I_B \cdot R_{BOL}(T) \tag{2.2.12}$$

An additional element change however this naive picture of the functioning scheme of the bolometers: the current passing through the thermistor causes power dissipation ($P = R \cdot I^2$),

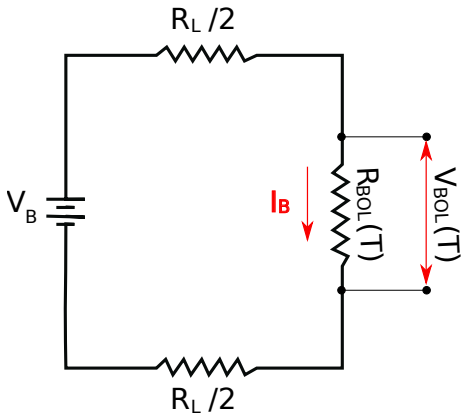

Figure 2.2.5: *Scheme of the bias circuit to extract the signal from CUORE bolometers.*

which heats up the thermistor hence reducing its resistance. This effect is called *electrothermal feedback*. In a steady situation the thermistor temperature T_{BOL} is

$$T_{BOL} = T_0 + P/K \tag{2.2.13}$$

where T_0 is the temperature of the heat sink (for CUORE is 10 mK), P is the dissipated power and K is the thermistor thermal conductance.

The electrothermal feedback induces a non ohmic behaviour that causes a non linearity in the relation between I_B and V_{BOL}. The resulting plot, called *load curve*, is sketched in Figure (2.2.6). From this curve we define the *dinamic* resistance as the inverse of the tangent to the V-I curve while the *static* resistance is simply the ratio V_{BOL}/I_{BOL}. As a matter of fact, increasing the bias current, the V_{BOL} raises until it gets to an *inversion point* and then it decreases again.

In static conditions (when there are no particle interactions in the absorber) the thermal and electric parameters of the thermistor are described as a point. To operate the detector, we must choose a bias voltage for each bolometer. The inversion point is highly unstable because in that region the bolometer response is not linear. It is preferable to choose a bias voltage V_B such that V_{BOL} is maximized but still in the ohmic regime. The point chosen on the load curve to operate the detector is called *working point*. In Figure (2.2.6) there is an example of a possible working point. The procedure used to find the working points for the CUORE bolometers will be described in detail in Section (3.1).

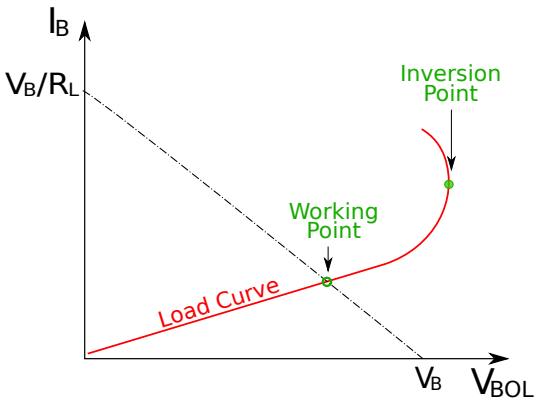

Figure 2.2.6: *Simple sketch of a load curve for a bolometer. In red is represented the I_B versus V_{BOL} relation (load curve), describing the thermistor behaviour; the dotted black line represents the bias circuit, and is called load line. The filled green dot is the inversion point while the empty green dot is the working point, selected by providing a particular V_B.*

2.3 Cryostat

In order to maintain a ton-scale detector to an optimal operational temperature around 10 mK, a powerful cryostat is needed. The CUORE cryogenic system construction had to face the challenge of building the biggest cryostat in the world reaching such low temperatures. At the same time it had to stand to strict radio-purity material selection criteria and provide a stable temperature over a lifetime of about five years, in a low vibration environment. This cryostat must be able to accommodate about 7 tons of lead to shield the detector from radioactive background and host more that 2500 wires for the channels readout.

To fulfill all these requirements a large custom cryogen-free cryostat was constructed. This is cooled down by means of 5 Pulse Tubes (PTs) cryocoolers and an high-power Dilution Unit (DU) working with an $^3He/^4He$ mixture.

2.3.1 Cryostat structure

The CUORE cryostat, shown in Figure (2.3.1), is composed by 6 nested vessels, kept at 300 K, 40 K, 4 K, 600 mK, 50 mK, 10 mK[8], respectively. A detailed description of the vessels production and machining can be found in reference [51].

[8]These are nominal temperature, but the actual temperature of each stage could be different.

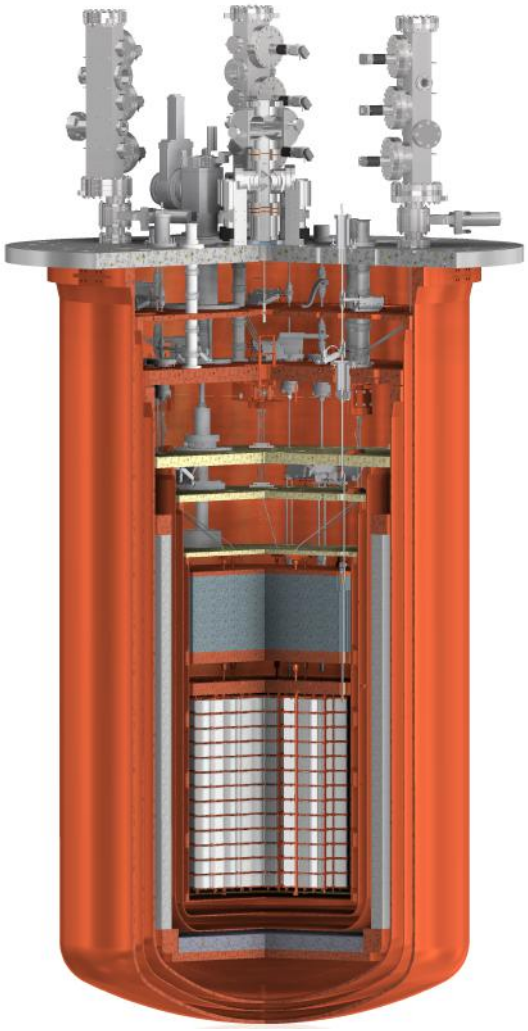

Figure 2.3.1: *Sketch of the CUORE cryostat with all its vessels and lead shieldings.*

The 300 K and 4 K shields are vacuum tight and therefore create two separated vacuum chambers of which the outermost one is referred to as Outer Vacuum Chamber (OVC) with a volume of 5.9 m^3 and a minimum pressure lower than 10^{-6} mbar. The innermost one is called Inner Vacuum Chamber (IVC), with a volume of 3.4 m^3 and a minimum pressure lower than 10^{-8} mbar.

The 300 K plate is the outermost plate and it is therefore at room temperature. Together with the upper flange it is the only part of the cryostat made by stainless steal because this material guarantees a better mechanical stability and vacuum tightness. The 300 K vessel however is made out of Oxygen-Free Electrolytic (OFE) copper which is the highest purity

copper available [9] (99.99%), produced by Aurubis company. The 40 K and 4 K plates and the corresponding vessels are made of OFE Cu and are covered on the outer side respectively with 30 and 10 layers of super-insulation in order to limit their irradiation on lower temperature stages. Each layer consists of double high reflectivity aluminized mylar and low thermal conductivity polyester. Inside the IVC there are the three sub-Kelvin thermalization stages: the 600 mK stage called *Still* and the 60 mK called Heat EXchangers (HEX), both made of OFE Cu, and the 10 mK stage reached by the Mixing Chamber (MC). The 10 mK plate and the Tower Support Plate (TSP) are made of ETP1 copper alloy, also called NOSV Cu, having an even lower radioactive content than OFE Cu in the bulk and a low hydrogen content. The TSP is inside the 10 mK stage and directly supports the 19 towers of the CUORE detector.
All the cryostat components are held by the 300 K plate: 3 bars per plate form a cascade system that holds all the plates which in turn support the corresponding vessels. The only exception is the TSP and therefore the towers: these are not held by the 300 K plate but by an external structure right above the cryostat called Y-beam, by mean of the Detector Suspension (DS) bars.

2.3.2 Inner Lead Shieldings

Despite the careful material selection, the cryostat structure is still a source of background because of residual radioactive contaminants such as isotopes from the radioactive decay chain of U and Th. To suppress γ background coming from cryostat materials, two different lead shields are placed at cryogenic temperatures inside the IVC: a lateral and bottom shield thermalized at 4 K and a second lead shield on the top of the TSP, thermalized at 50 mK.
The lateral and bottom shields are made out of archeological Roman lead dated I century B.C. and found on a Roman shipwreck close to Sardinia coast. A picture of the shipwreck finding is shown on the left of Figure (2.3.2). This lead has the peculiarity of having an extremely low radioactivity and of being depleted of ^{210}Pb, because it spent more then 21 centuries under 30 m of water, which protected the lead from cosmic rays, hence from cosmogenic activation. The contamination of ^{210}Po, thus of ^{210}Pb, were measured using samples of the same roman lead used for the CUORE shield, but from these measures it was only possible to set an upper limit of 7 mBq·kg^{-1} at 95% C.L. [52]. The ingots were cleaned and later they were melted and casted in nitrogen atmosphere, at MTH Metalltechnik Halbrüke GmbH & Co. KG foundry in Halsbrüke, Germany. A picture of

[9] Samples of OFE Cu can asses only upper limits on radioactive isotopes content: $6.5{\cdot}10^{-5} Bq/kg$ for ^{232}Th and $5.4{\cdot}10^{-5} Bq/kg$ for ^{238}U.

the casted sectors is shown on the right of Figure (2.3.2). The casted sectors are 6 cm in thickness, and the final shield has a radius and an height of about 64 cm and 178 cm, respectively. The total weight of the Roman lead inside the cryostat is around 5 tons and it is suspended from the 600 mK plate. Figure (2.3.3) shows the rendering of the Roman lead shield (left) and the shield after installation at LNGS at the end of 2015 (right).

Figure 2.3.2: *Left: recovery of the roman lead ingots. Right: casting of the roman lead into circular sectors at MTH.*

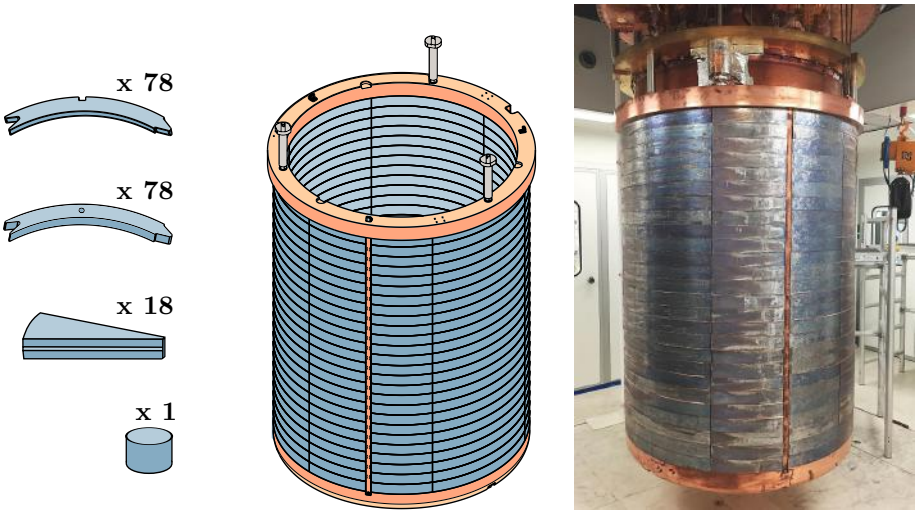

Figure 2.3.3: *Left: rendering of the lateral lead shield composed by 156 circular sectors, 18 sliced plus a central plug. Right: installation of the lateral and bottom lead shields.*

The second lead shield placed in IVC is called *Top Lead*. It is a 30 cm thick modern lead, placed below the 10 mK plate but thermalized at 50 mK. This shield protects the upper part of the towers from cryostat and external radioactivity. With a radius of about 36 cm, it accounts for more than 2 tons of lead. Limits on the contamination of the *Top Lead*

can be found in Ref. [53]: for the ^{232}Th and ^{238}U contaminations only an upper limit of $1.4{\cdot}10^{-4}\,\mathrm{Bq{\cdot}kg^{-1}}$ was set.

2.3.3 External infrastructure and suspension system

For an experiment searching for rare events using cryogenic calorimeter, like CUORE, in addition to the many constraints in terms of radio-purity, it is crucial to reduce every source of noise induced on the detectors. Among the different noise sources, there is the heat transfer to the crystals due to vibrations. It is therefore mandatory to put a big effort in keeping under control all possible sources of vibration or to isolate the detector from them.

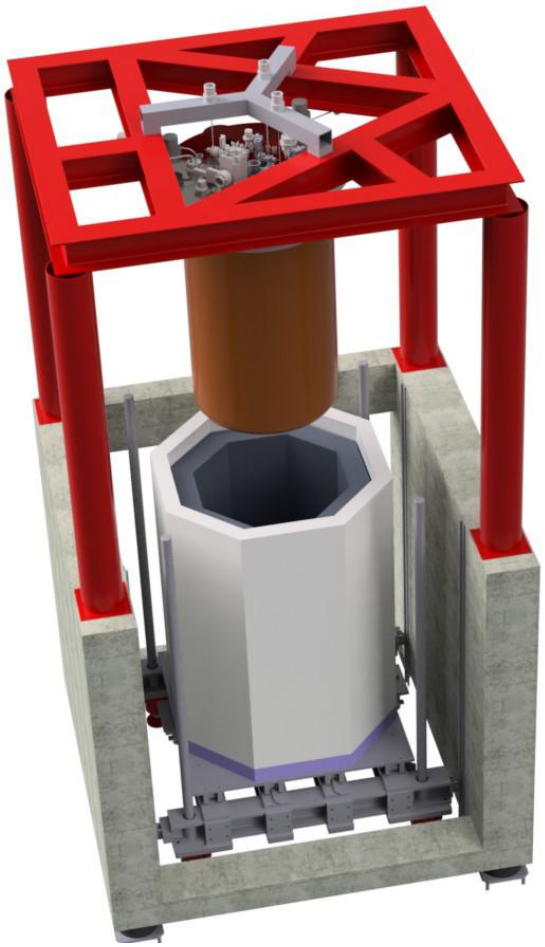

Figure 2.3.4: *Sketch of the CUORE support infrastructure.*

The cryostat is suspended from above to a structure called Main Support Plate (MSP), represented in red in the rendering of Figure (2.3.4). As we already mentioned, the detector is instead decoupled from the rest of the cryostat and is held by a Y-shape support structure called Y-beam, formed by three arms at 120° from one each other and of 1.2 m of length. The detector is suspended to the Y-beam by means of three DS [54], three identical vertical supports that run into the cryostat down to the TSP, therefore passing through several thermalization stages and regions of different vacuum levels. These supports indeed have to guarantee a very low thermal load, attenuation of residual vibrations from the Y-beam and radio-pure materials since they arrive in proximity of the detector. The Y-beam structure is anchored to the MSP in three points, by means of Minus-K insulation systems, a device formed by a particular arrangement of springs that tolerate heavy loads but at the same time behave as soft springs, resulting in an effective cut-off of the transferred vibration spectrum, minimizing vibration transmission from the cryostat and the MSP to the TeO_2 crystals. The whole MSP stands on a concrete structure by means of four 4.25 m tall sand-filled columns. The concrete structure is mechanically insulated from the floor of Hall A at LNGS by four custom designed seismic elastomeric dumpers whose main purpose is to attenuates the effect of earthquakes and vibrations from activities in the underground laboratories.

To further shield the detector from the γ-rays coming from the laboratory environment an external modern lead shield, of about 70 tons of mass and 25 cm of thickness, was design. The lead shield inner surface is covered by polythylene panels and boric acid powder, the former to thermalize neutrons and the latter to capture them. Neutrons in the underground laboratory of LNGS originate from external sources such as (α, n) reactions and cosmic rays spallation products. This shield usually rests below the cryostat, inside the concrete structure, but it is raised up during data-taking by means of four screw jacks to cover the external part of the cryostat. The entire external shielding structure is placed on a movable platform, which allows its removal if needed.

The cryostat infrastructure is hosted in a three floors building. The ground floor accommodates the base of the cryostat support and the external shielding, the DU gas handling system as well as the Pulse Tube (PT) compressors and sand-box used to attenuate the vibrations of the flex-lines going from the compressors to the PT motor heads. On the first floor there are the clean rooms used during the detector assembly as well as the clean room hosting the cryostat. Finally on the second floor there is the Faraday cage that surrounds the MSP and the Y-beam as well as the front-end electronics. In addition, outside the Faraday cage, at the second floor, there is also the CUORE control room and racks for Data AQuisition (DAQ) system and the control of other CUORE sub-systems.

2.3.4 The multistage refrigerator

The CUORE cyostat is a cryogen-free infrastructure able to guarantee a base temperature lower than ∼10 mK for a ton-scale detector and a 5 years lifetime. It is capable to maintain 0.98 ton and 7.4 tons respectively at 40 K and at 4 K, and cool down approximately 4.5 tons of material below 50 mK.

The cryostat relies on three subsystems to reach its different temperature stages, namely the Fast Cooling System (FCS) that lower the IVC temperature down to 50 K, the PTs to drive the 40 K and 4 K stages to their base temperature and finally the DU to cool down the detector to the operational temperature of 10 mK.

The first stage of the cool down is provided by the FCS which is a custom design apparatus to pre-cool the inner cryostat mass and in this way allowing to keep the cool down time well below one month. The FCS cools ^{4}He gas initially to 200 K and later to 50 K using an external cryostat powered by three Gifford-McMahon (GM) cold heads. The gas is injected into the IVC through a proper combinations of dedicated PTFE tubes and then circulated back into the external cryostat. The pressure of the ^{4}He in the IVC never exceed 1.3 bar, to avoid any risk of spoiling the cryostat sealings.

The FCS operates alone for few days only, after which also the PTs are turned on. The cryostat reaches 50 K in approximately two weeks. At that point, the FCS is switched off and the gas pumped out from the IVC; now only the PTs remain active.

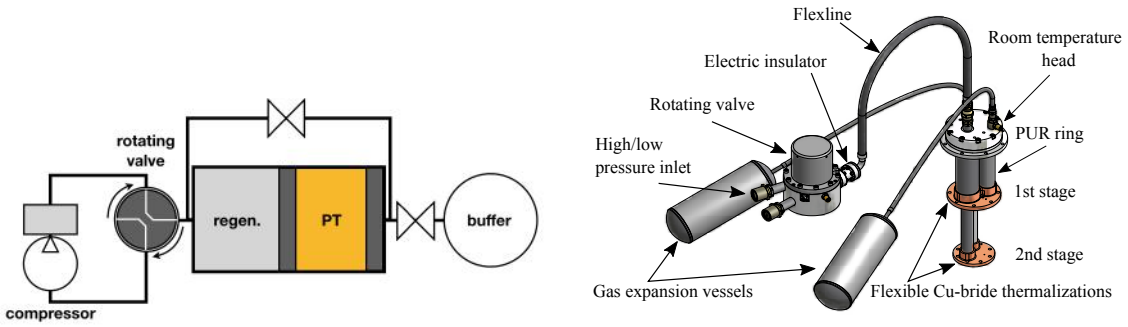

Figure 2.3.5: *Left: schematic drawing of the PT system. Right: rendering of PT-415RM.*

The second stage of the cool down takes the mass inside the IVC at ∼4 K. This temperature is obtained by means of five two-stages Cryomech PT415 Pulse Tubes, each one with nominal cooling power of 1.2 W at 4.2 K and 32 W at 45 K. Figure (2.3.5) shows a schematic drawing and a rendering of the PTs used in this experiment. A PT consists in a

rotating valve used to generate oscillating pressure upon which is based the cooling effect together with the displacement of He gas in the PTs. These are thin-walled tubes with heat exchangers at both ends after which the actual Pulse Tube takes the name. At room temperature, each PT is powered by a compressor that sends the He gas to the rotating valve, that alternatively connects the PT to the high and low pressure side of the compressor with a frequency close to 0.7 revolutions per second, equivalent to a complete cycle at 1.4 Hz. The usage of PTs instead of a LHe bath for this intermediate stage allows to increase the duty cycle and reduces the costs of the experiment due to the absence of cryogens to refill. The use of PTs without moving parts at low temperatures has also the advantage of diminishing the magnetic interference and guarantees higher reliability. These devices have however a disadvantage: due to the pressures waves generated by the compressed He gas and to the regular movement of the rotating valve, a characteristic vibrational noise is transmitted to the cryostat and also to the detector. In order to limit the injection of this noise in the detector, several countermeasures have been taken: a series of mechanical decouplers have been applied to different critical points of the PT-system. Before reaching the Faraday cage, the flex-lines enter a sand box filled with non-hygroscopic quartz powder. After the flex-lines enter the Faraday cage they are suspended to the ceiling and routed in such a way to dump the residual vibrations. Also the rotating valves are suspended from the ceiling of the Faraday cage in such a way to avoid any contact with the MSP or the Y-beam. Moreover, a remote motor option has been chosen for the PTs, so that the rotating valves are separated from the PT-heads by a swan-neck outlet. In addition, entering the cryostat at room temperature, all the PT flanges are mechanically decoupled from the top plate of the cryostat by mean of special polyurethane collars; at 40 K and 4 K stages flexible copper braids provide thermalization on the cryostat plates minimizing the mechanical coupling. Beside these numerous passive countermeasures, an active system to reduce PT induced noise have been developed: Section (3.3) will be completely dedicated to its description.

The base temperature is provided by a DRS-CF3000 Joule-Thomson Dilution Refrigerator (DR), called DU, customized by Leiden Cryogenics for CUORE purposes. A sketch of the DU is reported in Figure (2.3.6). Its nominal cooling power is 3 μW at 12 mK (2 mW at 120 mK), and the minimum reachable temperature for the CUORE cryostat at full load is around 7 mK.

The working principle of a continuous-cycles DR is based on a particular property of the ^{3}He/^{4}He mixture. In fact below a fixed temperature of 0.87 K the ^{3}He/^{4}He mixture separates into two phases: on one side an ^{4}He Bose liquid with a small concentration of ^{3}He (^{3}He dilute phase) and on the other side an almost pure ^{3}He Fermi liquid (^{3}He concentrate

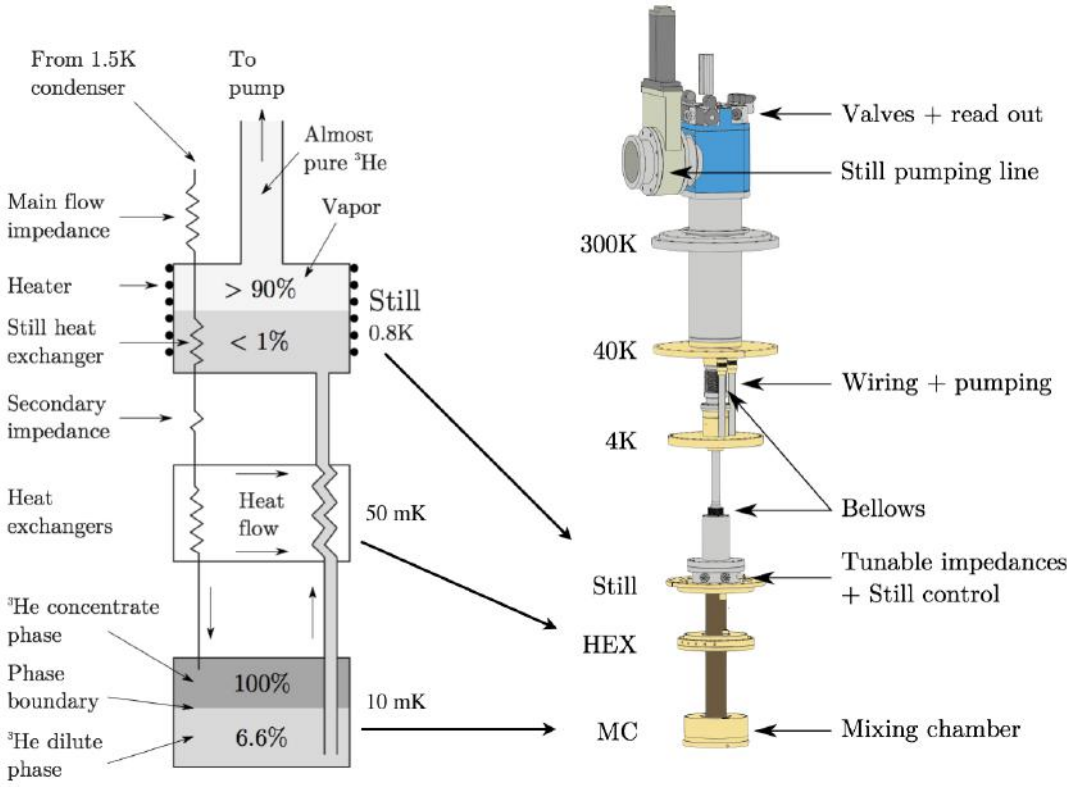

Figure 2.3.6: *Left: functioning scheme of the DU with the percentage of* ^{3}*He for each phase. Right: rendering of the CUORE DU from the room temperature stage to the MC (10 mK).*

phase). As a consequence of its lower density, the ^{3}He concentrate phase floats on top of the ^{3}He dilute phase. The concentration of ^{3}He in the dilute phase never reaches zero, but it stabilises on a constant value of about 6.6%. Since the enthalpy of the ^{3}He in the dilute phase is larger compared to the enthalpy of ^{3}He in the concentrate phase, the equilibrium is reached through an endothermic reaction occurring at the boundary separating the two phases. This process subtracts energy from the environment and is indeed the mechanism generating the cooling power of the dilution refrigeration. In order to obtain a continuous cooling power, the dilute phase is kept out of equilibrium by extracting its ^{3}He content and injecting it back into the conductance. This is done exploiting the remarkably higher ^{3}He vapour pressure above 0.6 K when compared to the ^{4}He one. Keeping the dilute phase above this temperature is then possible to extract only ^{3}He by pumping on it.

A schematics of what happens in a dilution refrigerator is reported in Figure (2.3.6). The phase separation occurs in the MC where the ^{3}He flows to the dilute phase generating

the cooling power. The dilute phase is then connected through a small pipe to a second chamber (*Still*) at higher temperature (>0.6 K). Here the ^{3}He is pumped out of the diluted phase and recirculated back to the concentrated phase. The recirculation system is however very complex. In fact unfortunately there are no pumps on the market that can work at cryogenic temperatures, hence to maintain the circulation we are forced to extract the ^{3}He gas out of the cryostat and then injecting it back without spoiling the cryostat temperature (need of low heat load on the MC). Before re-entering the cryostat, the ^{3}He gas is cleaned in LN_2 traps. Finally the ^{3}He gas goes back into the cryostat, condenses in the Joule-Thomson impedance passing through a series of counterflow heat exchangers (HEXs) to lower its temperature as much as possible before entering again the MC.

2.3.5 Detector Calibration System

The last important CUORE system that deserves an accurate description for the full understanding of the following analysis is the Detector Calibration System (DCS) [55]. As the particles interact in the crystals, the energy deposited is transformed into phonons and therefore into heat; the NTD thermistors convert the temperature variation into a voltage drop, but the relation between the initial particle energy and the measured voltage is not linear and may vary depending on the specific bolometer considered [56]. The $0\nu\beta\beta$ search is based on the identification of a peak in the energy spectrum, thus the understanding of the energy scale and resolution is crucial for the experiment. In CUORE each period of physics data taking, usually one month long, is bracketed by two calibrations. The former provides an energy calibration in the detector conditions as close as possible to the following physics data and the latter ensures the stability of the detector response during the data taking. The DCS is designed to provide a reliable energy calibration on a wide energy range [10]. The design of the DCS must guarantee some basic requirements both on the thermal load and data taking point of view and a low failure rate since it will be operated often during the CUORE lifetime. The DCS consists in 12 kevlar strings, each one equipped with 25 thoriated (^{232}Th) tungsten capsules [11], whose activity must be high enough to calibrate in the shortest possible time, but also sufficiently low to avoid pile-up in the acquired data. To achieve an uniform and equilibrated illumination of the detector, the sources activities have been optimized by GEANT4 Monte Carlo simulations and their positioning has been decided to avoid detector self-shielding. Figure (2.3.7) (Right) shows the position of the strings deployed among the towers (6 strings with 3.5 Bq of activity),

[10] CUORE can be used also for other rare events searches for which also a calibration at low energies is important.

[11] Copper capsules containing a ^{232}Th source and covered by a PTFE layer.

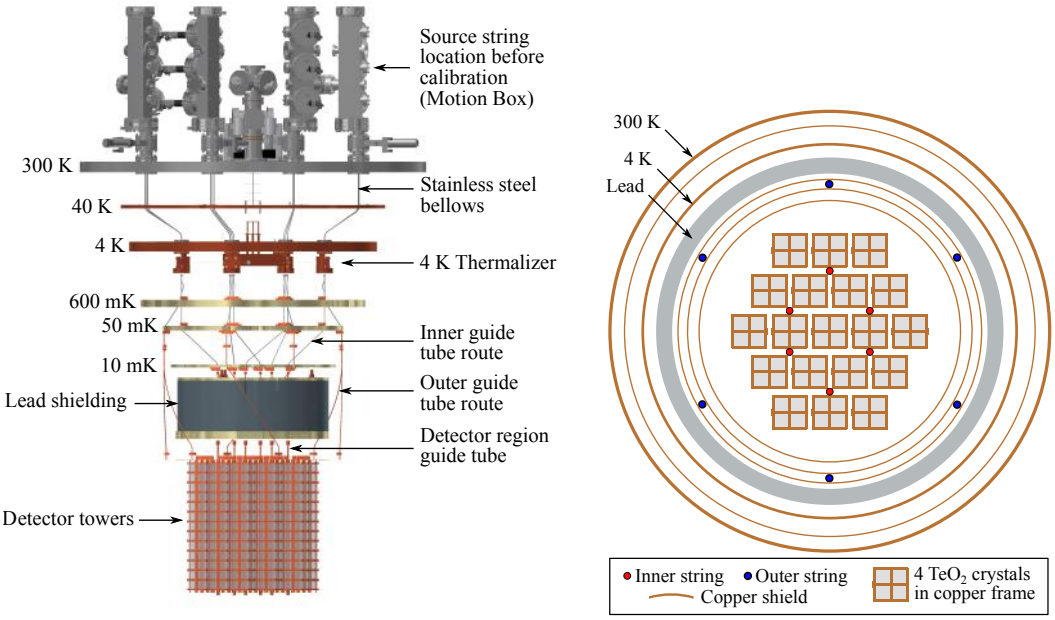

Figure 2.3.7: *Rendering of the DCS system. Left: in this drawing of the inner parts of the cryostat the path done by the 12 thoriated kevlar strings is visible, starting from the motion boxes and ending within the detector towers. Right: horizontal section of the detector and the cryostat where the position of the strings is visible (6 within the towers and the rest just before the roman lead shield).*

facing directly the detector and additional 6 external strings with higher activity (19.4 Bq) deployed outside the 50 mK vessel. During physics data taking the thoriated strings are wound on spools above the cryostat at room temperature, so that the detector is protected from the Th γ-rays from the top lead shield. Before the beginning of the calibration runs the strings are lowered and guided into the cryostat by a series of tubes made by different materials depending on the temperature stage (PTFE, stainless steel, copper). The tubes are thermalized at each stage and then, below the 4 K plate, they split into inner and outer paths: the inner path leads to the 10 mK volume between the towers, while the outer path leads to the 50 mK stage. Despite all the thermalizations provided along their path down to the detector, lowering the strings causes a non-neglectable rise in temperature of the bolometers and few hours are needed after the end of the DCS deployment before starting a new data taking.

In Section (4.1) a full description on the use of the calibration data is provided.

2.4 Read-Out Chain

To complete the description of the CUORE experiment we must devote few words to the read-out chain, the combination of two systems that allow to control the biasing circuit of the bolometers, described in Section (2.2.3), and that enable to acquire the data coming from the detectors. These two interdependent systems are the *Electronics*[57] and the DAQ.
The former has the double role of providing the bias voltage necessary to measure the NTD resistances and at the same time amplifying the signal coming from the bolometers. Part of the electronics is an active filtering system that acts as anti-aliasing and allows to cut out high frequencies that are far from the particle signal bandwidth (in the 1 Hz region).
The latter has the important role of digitizing the filtered signal, triggering it and writing the data to disk for an offline analysis. The DAQ system also controls all the electronics parameters and the power supplies through a communication system that links the computer that controls the full read-out chain (called *Builder*) to all the parts of the electronics system. The communication system uses a standard CAN-bus serial connection integrated with optical fibers for the main paths to avoid possible injection of disturbances and creation of ground loops.

2.4.1 Electronics

The electronics system is composed mainly by three parts: the Front End (FE) boards (or main-boards), the Bessel boards (or anti-aliasing filters) and the Pulser boards. A simplified representation of the full read-out chain is depicted in Figure (2.4.1).
The FE boards racks are situated inside the Faraday cage, on a strut overlying the Y-beam without touching it and resting on the MSP. There are 7 FE small racks, each one with two crates, for a total of more than 1000 channels, between bolometers and thermometers placed inside the cryostat for monitoring purpose. A FE crate hosts 13 boards, with 6 amplifiers each, and one power supply unit. On the back panel of the FE crate, there are 6 cables arriving from the cryostat, each one containing the wires of 13 bolometers (one column of a tower): the back panel is meant to reroute the wires so that the 12 channels are split between two adjacent boards and the 13^{th} is routed to the last board of the crate. On the other side of each cable arriving on the back panel of the FE, a thermistor, glued on the crystal, is connected by two wires across which the bias is provided and the signal is read. The thermistor signal is not referenced to ground but is acquired in differential mode, because in this way the common mode noise, such as cross-talk between two adjacent channels, can be suppressed once the signal reaches the preamplifier input. When

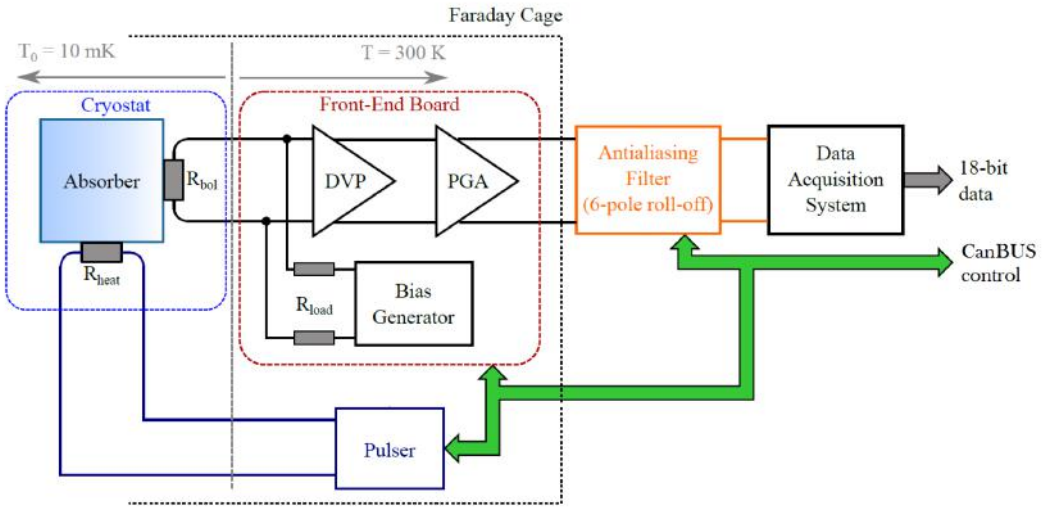

Figure 2.4.1: *Schematic of the read-out chain. The FE boards provides the NTD with bias polarization and a two stages of amplification for the bolometer signal (DVP and PGA). The signal is later filtered and digitized. The pulser boards power and control the Joule heaters. A CAN-bus communication system guarantees the communication between the Builder and all the electronics boards. Image adapted from [45] .*

the signal from a bolometer enters the FE board, it is amplified by a factor 210 V/V by mean of a preamplifier. But this is not all that happens at the preamplifier level. In fact here the signal is also shifted by an offset, letting the position of the signal in the DAQ dynamic range be adjustable remotely. Other adjustable parameters are the values of some trimmers, designed to compensate for two effects: the thermal drift of the FE electronics parameters (offset and gain), due to the warm up of the electronic components, and the common mode noise in the incoming signal. The thermal drift compensation parameters have been calibrated in special runs with the electronics at different ambient temperatures, and then stored in an EPROM on the FE board; when the offset is set the correct coefficient is chosen, depending on the current environmental temperature. Also the Common Mode Rejection Ratio (CMRR) trimmer needs a scan, in order to identify the best value for each channel. The CMRR optimization was done both before the commissioning, by minimizing the output voltage when an asymmetric bias is applied to the input, and after the cool down in the firsts weeks of data taking, by varying the trimmer values and minimizing the output signal RMS of the bolometers. After the first amplification stage there is a Programmable Gain Amplifier (PGA), settable between 1 V/V and 50 V/V. Due to the wide spread in energy gain of the detectors, this second amplification stage is necessary to

use at best the DAQ dynamic range. In addition to the amplifiers, FE boards have also a micro-controller that manages the board according to the DAQ instructions, sent through the CAN-bus communication system.

The signal exiting the FE boards is routed to D-Sub connectors that group 2 boards together. The signal is then sent to the Bessel boards before being digitized. These are antialiasing active low-pass filters of Bessel-Thomson type (six-poles filter). The filter provides an attenuation of 120 dB/decade with a cut-off frequency that can be remotely set to the following values: 15, 35, 100 or 120 Hz. The cut-off is chosen depending on the sampling frequency of the digitizers. Each Bessel board has 12 channels and a micro-controller managed by the DAQ through the CAN-bus communication.

Part of the electronics system are also the Pulser boards, placed on top of the FE racks. The pulsers are used to send short, periodic, δ-like voltage pulses to the Joule heaters on the crystals. The result is a constant energy release on the absorber that mimics a particle interaction. These heater pulses are flagged by the DAQ and are used off-line to characterize the detector response in time, and eventually compensate for possible small temperature variations of the detector. Each pulser board has 4 channels and each channel is connected to an entire column (13 channels), so that each pulser board is assigned to one tower. In order to create a pulse as similar as possible to a real particle interactions there are some parameters that are remotely set by the DAQ such as the amplitude and the duration of the pulse, as well as its periodicity. The equivalent energy in keV of the pulses is not fixed a priori, but once the amplitude and duration are set the resulting energy of the pulse in the detector is stable in time and can later be calibrated in the same way than any other particle-induced pulses. Usually parameters which pulse energy corresponds roughly to 3 MeV are chosen, in order to be close to the region of interest for $0\nu\beta\beta$ search, but not exactly on it. Beside this heater pulse used for stabilization (called *Stabilization Pulse*), other two pulses are sent to the Joule heaters in order to monitor the overall stability of the detector at multiple energies: one below the Stabilization Pulse, usually with the equivalent energy of 1 MeV, and a second one with equivalent energy around 5 MeV.

Finally all these boards are powered by a system of multiple power supplies. The power to the FE boards, Bessel boards and Pulser boards is provided by 5 Genesys 750 W/1500 W AC/DC power supplies produced by TDK-Lambda. These Lambda power supplies provide 48 V voltage for several DC/DC units, having 2 analog output adjustable between $\pm$5 V and $\pm$15 V and one digital output, settable from 5 V to 15 V. The final stage is provided

by linear power supplies generating ±5 V with very low noise and high stability. The role of these different stages for the power supply is to filter out the noise coming from the power grid. The Lambdas power up all the electronics but it does not provide the current bias for the NTDs. This is provided by two 2231A-30-3 Triple-channel DS power supply produced by Keithley. All the power supplies are remotely controlled by the DAQ: the Lambda and Keithley power supplies are managed through RS232 serial communication while both the DC/DC and the linear power supplies are controlled through the CAN-bus communication system.

2.4.2 Data Acquisition System

The last CUORE system that will be described in this Chapter is the DAQ. Beside handling the electronics, the DAQ is responsible for turning the analog signal exiting the Bessel filters into triggered data, ready to analyze, and to keep the database updated with all the sensible information concerning the data, that are not stored directly on the data files.

The CUORE DAQ system is an evolution of the acquisition system used previously for CUORE-0. The major upgrades concern the ability of managing an order of magnitude increase in the number of channels, and therefore of incoming data, and the control of the electronics and power supplies. Figure (2.4.2), summarizes the most important components and processes forming the CUORE DAQ. The hardware is placed in three cabinets positioned just outside the Faraday cage, in the CUORE control room, on the second floor of the building hosting the whole experiment. Two of the cabinets contain the digitizer modules while the third one has all the computers used for the data acquisition. All the DAQ computer run Scientific Linux [12] and communicate through a standard network connection using the Transmission Control Protocol/Internet Protocol (TCP/IP). These computers have different names depending on their role within the readout chain and the processes that they run: there are 6 computers which role is reading and triggering the data stream from the digitizing modules called *Data Readers*, and one who has the role of handling all the DAQ subsystems, building the events and writing the files in the final format, called *Event Builder*. The Event Builder is the only computer accessible from the outside because the Data Readers are connected to the Event Builder through a local network. The Event Builder is accessible by the shifters to start and stop a measurement (run) or to perform other data taking related activities.

[12] Scientific Linux is an operating system specifically developed for scientific purposes by Fermilab and CERN.

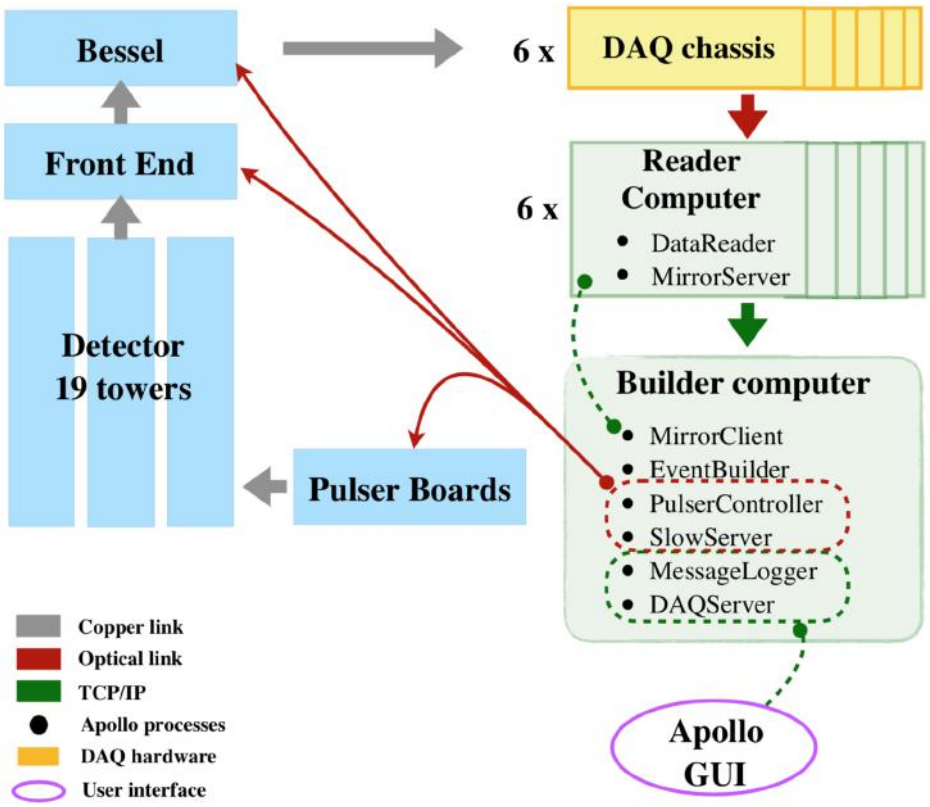

Figure 2.4.2: *Sketch of the CUORE DAQ system.*

DAQ boards

The output of the Bessel filters is directed to an array of National Instrument (NI) digitizer modules (PXI-6284). This model has an 18-bit Analog to Digital Converter (ADC) and, splitted into 2 connectors, 16 differential analog inputs and 48 digital I/O. Since the NI connector is incompatible with the 12 channels D-Sub connector coming from the Bessel boards, a series of custom Patch boards have been designed to remap two - 12 channels connectors into three - 8 channels connectors compatible with the NI modules. The digitizer modules are housed into six NI chassis (PXI-1044) of 14 slots each, placed in turn into two of the three DAQ racks, together with the correspondent crates of the Patch boards [13]. In total there are 64 digitizer modules, equivalent to 1024 channels acquired in differential mode, part of which are bolometers and the remaining are thermometers internal to the cryostat. Every chassis has a controller module in the first slot (PCI-PXI8336) whose role

[13] Each rack has 3 chassis and 3 patch boards crates, each one on top of the corresponding chassis for an orderly cable placement.

is to collect the digitized data from all the modules thanks to the chassis PXI bus, and send it to a Data Reader computer using an optical link to guarantee high data transfer and a total electrical insulation between the acquisition computers and the rest of the DAQ and electronics. The chassis have a 10 MHz internal clock shared among all the boards, but in order to guarantee the time alignment during data taking we need to exploit an external clock, equal for all chassis. To meet this requirement one chassis has been chosen as the "master chassis" and its clock is propagated to the others using a BNC coaxial cable and dedicated BNC connectors on the chassis back-panel.

The digitizer modules were chosen taking into account that the ADC resolution must be negligible compared to all other sources of noise. Considering that the maximum ADC dynamic range is 21 V ($\pm$10.5 V), the minimum resolution results $10.5/2^{17} \simeq 80\,\mu$V which is in effect neglectable compared to the RMS of the typical CUORE signal when no events are present (few millivolts).

The sampling frequency used to digitize the data must be chosen considering the features of the signal that we want to record: pulses have typical rise times of the order of few tens of milliseconds and decay times about one order of magnitude larger, resulting in a frequency bandwidth that extends up to about 10 Hz. In CUORE-0 a sampling frequency of 125 Hz was picked because adequate to properly reconstruct the signals, but for CUORE we choose the maximum sampling frequency achievable while avoiding cross-talk effects between the channels acquired by the same DAQ board. A sampling frequency of 1 kHz was selected because a more accurate pulse reconstruction could allow further studies on pulse shape of particle events.

Finally, in addition to the 16 differential channels acquired on each board, there are also some digital channels that can be used for both input and output. In particular we use these digital channels to ensure a synchronous data acquisition among the chassis. In fact when the acquisition starts, the six Reader computers, connected by optical fibre to the NI chassis, stands in waiting mode until the "master" Reader sends a trigger to the master chassis which propagate the trigger to all other chassis using the digital channel. In addition the digital lines are also used to contemporaneously send a periodic signal to the chassis, to check offline if the data acquisition is synchronous on all channels.

Digital channels are also used for other purposes such as flagging pulser events, flagging period of the measurement in which the data is not useable because a communication with the electronics was occurring, and so on.

Apollo

Each NI chassis is linked to one Reader, where a process, called DataReader, runs independently. The DataReader process is only the first of a series of processes that are part of the `Apollo` framework. Apollo is an acquisition software specifically developed for the CUORE experiment and designed with high level of modularity. Apollo offers indeed easy scalability for the number of acquired channels and the needed flexibility to handle the various subsystems of the apparatus. Apollo is written in the C++ programming language and built by almost all custom software with the exception of the NI drivers used to communicate with the NI controller on the chassis and the ROOT [58] software package[14]. We will quickly go over the main Apollo processes, represented in Figure (2.4.2), following when possible the data flow.

The `DataReader` is the main process running on the Reader computers and the first process the data encounter after digitalization. It fetches the data from the NI controller and writes them into shared memories, accessible also by other Apollo processes and by a software oscilloscope for online visualization of the data. The shared memories allow multiple processes to access the same data without the need to copy them multiple times. The shared memories are mirrored from the six Reader computers to the Builder computer using a process called `MirrorClient` on the Builder side and `MirrorServer` on the Readers side. The DataReader has also an other important role: running the trigger algorithm on the subset of channels present on that Reader.

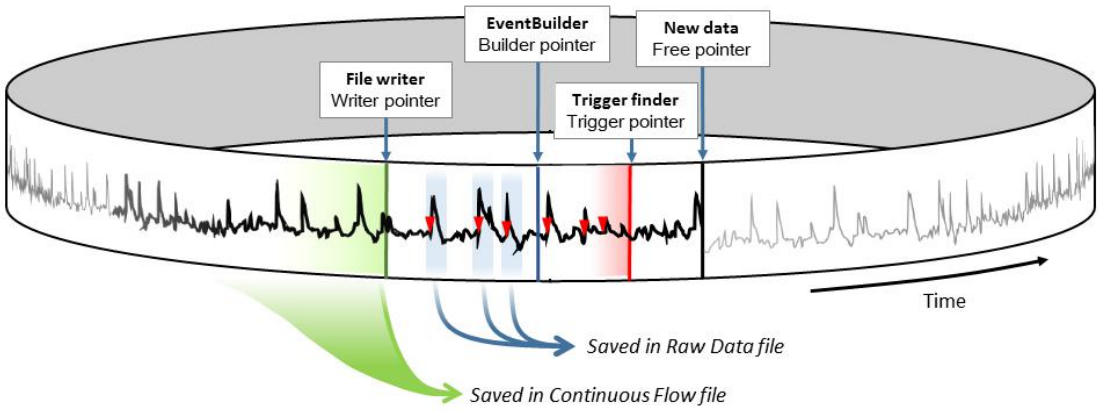

Figure 2.4.3: *Representation of the shared memories as circular buffers from [59].*

The shared memories act as a circular buffer, depicted in Figure (2.4.3), accessed by various

[14]ROOT is a software package developed at CERN and widely used by the particle and astro-particle community for data analysis.

processes. Each process has a pointer scanning the data stream and they cannot surpass one another so that if one process takes more time for whatever reason, the others must wait and we do not incur in running conflicts. The first process accessing the data is the trigger finding algorithm. Unlike other experiments exploiting an hardware trigger, thanks to its low sampling and event rates, CUORE is able to afford an online software trigger. This gives the advantage of reducing the costs for the hardware and, thanks to the Apollo modularity, allows to implement multiple trigger algorithms, each one with customizable channel by channel configurations. At the moment there are two trigger algorithms running in parallel on each channel: the *noise* trigger and the *signal* trigger. The former is a simple random trigger, that fires with a given probability per unit of time, design to acquire part of the waveform that, apart from accidental coincidences, it is devoid of pulses. These are called noise events, used to monitor the detector stability and for a run by run noise characterization, crucial to evaluate the pulse amplitude, as will be discussed in Section (4.1). The latter is a derivative trigger which fires whenever the derivative of the waveform calculated on a given distance (average) exceed a threshold for a certain number of samples (debounce). Average, threshold and debounce are parameters that can be tuned for each bolometer in order to accommodate the wide range of behaviours among channels. A whole section of Chapter (3) (Section (3.2)), will be dedicated on tuning the derivative trigger parameters and verifying the resulting energy thresholds.

The DataReader has access only to a limited number of number of channels, hence it does not have a general view of the whole detector and can not build the event. Accessing to all the channels at once is necessary in order to order temporally the events and associates the side pulses (operation that in CUORE has been moved to the offline analysis). This is done instead by the `EventBuilder` process, running on the Builder computer. The EventBuilder is an instance of the analysis code `Diana` which reads the trigger flags from all the available shared memories instead than from file. Unlike CUORE-0 where for each trigger a 5 s waveform was actually saved in to the triggered data files, called *Raw Data*, in CUORE only the trigger timestamp is saved together with the basic event information. In CUORE we chose to have windows of 10 s, therefore we define an event as a region of the waveform of 10 s, of which 3 s are before the trigger (called pre-trigger) and 7 s are after the trigger (post-trigger). During the analysis, the Raw Data files are used to retrieve the event info and the trigger timestamp; from the event timestamp is then possible to randomly access the actual waveform saved in continuous files. This choice was taken to address a problem concerning the slowdown of some processes: in particular during the data analysis reading files without the waveforms is much faster and easy to read.

The process writing the continuous files to disk is the last one accessing the buffers; in fact

the DataReader process has also the role of saving for each channel the whole acquired waveform to files written in ROOT format called Raw Data Continuous Flow (RDCF). This is unusual among the particle physics experiment, but in CUORE this is possible thanks to the small size of the data files due to the low sampling frequency. Storing the continuous data allow us to retrigger the data if a better trigger algorithm is developed or for further studies on data not allowed by the triggered events. Indeed this is what happen in the firsts months of CUORE: when the data taking started we were using event windows of 5 s, like it was done in CUORE-0. Later it was proven that the noise and pulse characterization improved if using a window of 10 s and so the first data acquired was retriggered to 10 s windows and used in the analysis presented here.

In addition to the processes presented so far, there are others equally important to enable the DAQ to work properly. The most important is the `DaqServer`, a process that has control over the whole system including starting and stopping the measurements and monitor the status of the system during acquisition. The shifter can communicate with the DaqServer using the Apollo graphical user interface, nominally the `ApolloGUI`. Through the GUI the user can start and stop a measurement, but it is also possible to monitor the status of the data taking such as checking the event rate or a rough amplitude spectrum; the GUI allows also to look on real time data and its noise power spectrum for a maximum of 4 channels at the time.

The pulser boards are managed by the `PulserController` process which periodically communicates through the CAN-bus the pulser parameters to the boards, preparing them to fire. The boards do not fire until a trigger signal is sent them through optical fibre connected to the digital lines of the NI digitizers. In this way, when the trigger is sent to the pulser boards, at the same time the flag is acquired by the digitizers, grouping the digital channels to form a 16-bit channel, similar to the analog ones. Using the 16-bit channel we save in the data not only the timing information of the pulser, but also a pulser identification number which univocally identifies the heater pulse properties in the database.

All Apollo processes produce some messages that are gathered by a dedicated process, the `MsgLogger`. This process is also important to allow different processes to know each other status.

Lastly there is a process that, even if not explicitly, has been mention many time in this Section. I am talking about the `SlowServer` whose responsibility is the communication with all the DAQ hardware, FE, Bessel and Pulser boards. The SlowServer hides the details of how the single protocols are implemented and can be used by other Apollo pro-

cesses to modify the status of the hardware, such as setting different parameters of the FE boards. Usually, during stable data taking, the SlowServer is used only to interact with the pulser boards, but there are measurements that intensively use the SlowServer even during data taking such as load curve and working point measurements (more details on this topic in Section (3.1)).

During the data taking, in addition to the `Apollo` processes, we also evaluate some basics quantities such as the trigger rate, the pulser rate, the baseline average value, the baseline RMS, etc. Those measurements are written to a database which is accessible in real time through a web interface and used for the online monitoring of the data taking. This system is called CORC.

Database

All the information not stored in the data are saved into a `PostgreSQL` database. The CUORE database is designed to be a unique place where to store informations about the apparatus mapping, bolometers characteristics and position, and most important to keep track of the measurements acquired. During stable background data taking, or calibration, we acquire usually 2 runs a day; the run number, as well as the run start and stop time and the DAQ, trigger and pulser configurations are saved into the database.
The database is also very helpful during data analysis. First of all every time there is some global variable or quantity that is accessed many times throughout the data processing and analysis, the database is a good place where to store it so that the variable does not need to be copied around. Secondly, the shifter can use the database to flag periods in which the data is not usable for one or multiple channels, called *BadIntervals*; it is possible also to flag channels that failed a particular step of the data processing or that cannot be included for one analysis, but are ok for another one.

2.5 Comissioning

The commissioning of the CUORE cryostat started at the beginning of 2014, when its assembling reached the final configuration. The first phase of the commissioning was completed in March 2016, when a stable base temperature of 6.3 mK was reached with only the towers missing from the cryostat. During the cryostat commissioning there have been many test runs with the purpose to check the cryostat performance. Every run consisted in the installation of new parts in the apparatus followed by a cool down test that required several months. The first test run was done to characterize the dilution

refrigerator and to reach the base temperature. The second test run served to fully test the read-out chain using a tower with only 8 crystals (called *Mini-tower*) installed directly on the 10 mK stage: the test was used to verify the functioning of electronics and DAQ chain and to prove temperature stability. The third test run had the top lead installed and

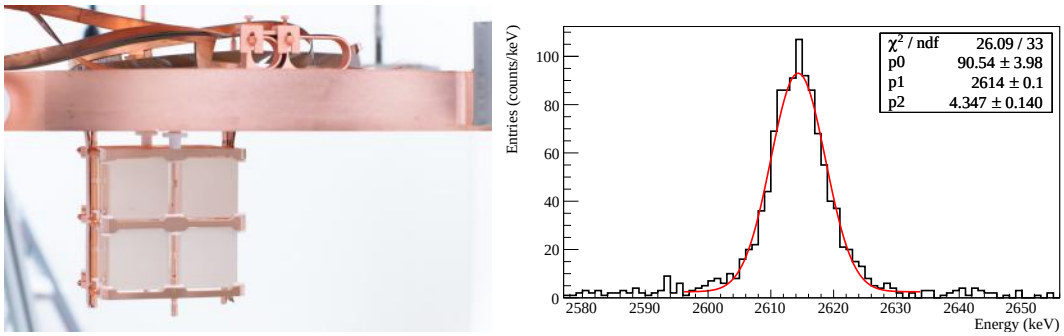

Figure 2.5.1: *Third commissioning test run. Left: photo of the Mini-tower (small CUORE tower containing only 8 bolometers) installed on TSP plate. Right: energy resolution at 2615 keV, obtained during calibration on the 5 best channels, without any detector optimization.*

the Mini-tower moved to the TSP. During this run a noise characterization was performed which highlighted and confirmed the presence of a 4 h mechanical oscillation probably induced by the PTs. This effect has been mitigated by taking some precautions: on one hand, by rerouting the PT flex lines, we reduced the incoming vibrations from the PTs, on the other hand the effects of the vibrations has been mitigated by making the cryostat more strongly coupled with the rest of the support structure.

During this test an external calibration was deployed and it allowed to get a very preliminary energy resolution of about 10 keV FWHM at 2615 keV (γ line from ^{208}Tl) without any detector optimization. Figure (2.5.1) shows a photo of the Mini-tower installed on the TSP and the energy distribution of the events during the calibration, from which a rough estimate of the energy resolution has been extracted.

The fourth test run was done to prove the refrigerator power of the cryostat with the lateral lead shield installed inside the 4 K stage. In fact, after the completion of the third cool down test, the installation and commissioning of the lateral and bottom roman lead shielding began. This test indeed included cooling the a mass of approximately 14 ton down to 4 K and acquiring data from the Mini-tower before moving on to detector installation. This time the temperature reached at the coldest stage was 6.3 mK, obtaining a cooling power of more than 3 μW at 10 mK.

After the cryostat commissioning was completed, we proceed with the commissioning of

the other systems, including electronics and DAQ, then we proceeded with the tower installation and with the final cool down which happened right before the beginning of the data taking.

2.5.1 Towers Installation

The installation of the towers began on July 27^{th} of 2016 and ended on August 26^{th} of the same year with an average one tower per day (considering working days only). Even if the installation lasted only about one month, this operation required a very long preparation and a careful analysis of all the possible risks and accidental problems for both the detector and the installation team.
The installation took place in the same CUORE clean room where the towers have been assembled few years before[60] and kept under N_2 atmosphere up to this moment. The clean room is divided in different areas utilized for different scopes: an entrance meant as an interspace between the outer radioactive world and the clean room where all objects coming from outside are thoroughly cleaned with isopropyl alcohol and where anyone going inside must wear special clothes in order not to contaminate the clean room; an area dedicated to sensor gluing on the crystals (used during detector assembly); one called Clean Room (CR) 4 where the towers are stored together with most of the pieces to be install and all the instruments needed during the installation; and an area containing the refrigerator plates, called CR 5. Inside this last area an additional temporary clean room, called CR 6, was mounted before the tower installation began. This small clean room had the peculiarity that it was flushed with Rn-free air [61] and its radon and particle level was continuously monitored. The installation was the first (and hopefully the last) time in which the towers were exposed to air. After the installation of each tower, a bag flushed with N_2 was mounted to protect the towers during non working hours. For the whole installation time of one tower the installation team was not allowed to exit the CR 6, thus a support and monitoring team were always present outside the CR 6 for safety and logistic reasons, to provide communication with the outside world and to log everything was happening inside CR 6 for future reference. The installation team had the role of checking all the connections of both NTD and heaters, attaching the towers on the TSP, connecting the DCS copper tubes to the bottom of the TSP, routing and securing the wires above the TSP. The installation team trained on each one of these operations with a mock tower made out of brass “crystals" and spare or discarded parts from the tower assembly. Of all the 988 bolometers, during the connection inspection 8 were found to be problematic, but only 4 were irreparably broken, hence more than 99.5% of the crystals are functioning and taking data. Figure (2.5.2) (left) pictures one of the last days of the installation phase,

when all the towers were in place. After all the wires routing, the last check needed was the functioning of the DCS, before the 10 mK vessel was finally closed. The check consisted in lowering the kevlar strings down to the detector and verify that no obstacle stopped the calibration sources at room temperature. The photograph in Figure (2.5.2) (right) capture the moment in which one of the strings reached the bottom of the towers.

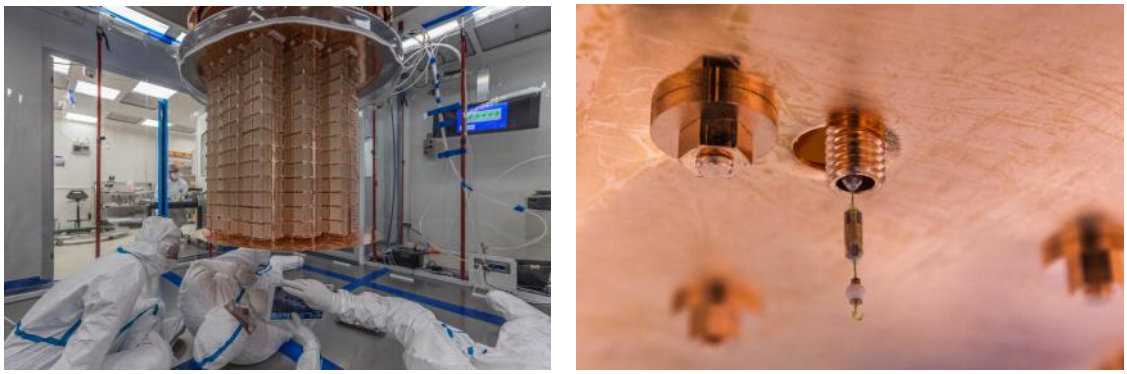

Figure 2.5.2: *Towers installation. Left: picture from one of the last days of the towers installation taken inside the CR 6. Right: picture of the bottom of the detector during the DCS room temperature test, where a kevlar string with the Thorium sources exits one of the copper pipes.*

2.5.2 CUORE cool-down

After the completion of the towers installation and the cryostat closure, the first phase of the official CUORE cool down started. The left plot in Figure (2.5.3) shows the temperatures of the 40 K and 4 K plates during the cool down. This phase started on December 5^{th} 2016 with the turning on of the FCS in order to pre-cool the cryostat with helium exchange gas. After about 4 days, also the 5n PTs were switched on. After the first week, the FCS was switched off and the cool down continued using the PTs only. The inner part of the cryostat reached 3.4 K after approximately 22 days from the beginning of the cool down. In Figure (2.5.3) two periods in which the temperature remained stable are visible: the first one was caused by the pumping of residual helium exchange gas in the IVC while the second one was done on purpose and it was not requested by the cool down procedure. A period of about one month was indeed dedicated to the optimization of several subsystems, especially the debugging of the electronics noise. In fact this period with the detectors not at their base temperature was exploited to study possible sources of disturbances because it was possible to decouple the electronics noise from the bolometer intrinsic noise not yet present because the temperature was far from the operational temperature of the NTD.

On January 23^{rd} 2017, we started the second phase of the cool down: the DU was turned on. This phase took another 4 days and finally on January 26th a base temperature of ∼6.9 mK was reached (see Figure (2.5.3), right plot). Without counting the month dedicated to electronics optimization, the total net cool down time was ∼26 days, during which almost 10^9 J of enthalpy has been removed from the cryostat.

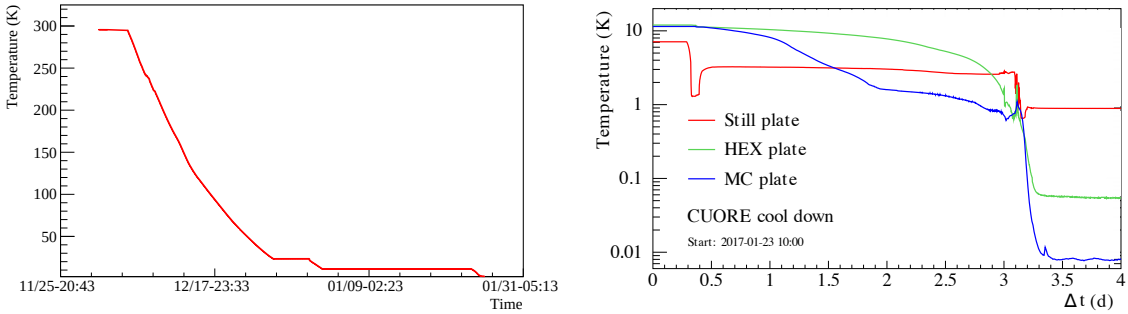

Figure 2.5.3: *Temperature plots of the CUORE cool down in the period between December 2016 and the end of January 2017. Left: temperature measured on the MC with the noise thermometer for the whole cool down duration: the first period of decreasing temperature is due to FCS and then PTs and FCS together; the second period is PTs while the last one is due to the DU. Right: temperature measured on three different plates (Still, HEX and MC) during the last 4 days of the cool down, when the DU was turned on; on the fourth day all the plates reached their base temperature.*

Immediately after reaching the base temperature, the first CUORE pulse was observed. This was a very exciting moment for the CUORE collaboration, however the detector was not ready to acquire data because all the systems needed tuning and optimization.
The last step of the commissioning phase, before the beginning of data taking was the test of the calibration system. Finally, in April 2017 the calibration sources were deployed for the first time with the detector at base temperature: 12 thoriated strings facing the detector was used to perform a preliminary energy calibration using the main peaks of ^{232}Th and to evaluate the energy resolution on the 2615 keV γ peak from ^{208}Tl .
In conclusion, CUORE commissioning ended successfully in April 2017 and CUORE data-taking began immediately after.

Chapter 3

Optimization

The optimization of the detector is a rather long and complicated process and still it is not over, even after the publication of the first CUORE results. All the subsystems presented in the previous Chapter need indeed to be tuned, keeping in mind that the final goal is to maximize the sensitivity which depends on the total mass of the detector M, the live time of the detector $\mathcal{T}$, on the background index b and on the energy resolution. Once the detector has being built we cannot do anything about M and b, but we can act on the live time of the experiment, tuning the detector in order to mimimize the probability of having periods of unstable data taking, and we can act on the energy resolution by optimizing all detectors parameters.

The factors concurring to the worsening or improving of the energy resolution are countless, but most of them concur to the Signal to Noise Ratio (SNR), partially due to noise source (small temperature instabilities, electronic noise, grounding, mechanical vibrations induced on the systems) and partially due to tuneable detector parameters (voltage chosen to bias the sensors, operational temperature from which the sensors behaviour depends), and of course the quality itself of the crystals and the thermistors. A good SNR allows to correctly evaluate the signal amplitude, thus obtaining a good energy resolution.

Another important set of factors that highly influence the quality of the data are some electronics, DAQ and trigger algorithm parameters, such as gain and offset, cutoff frequency of the Bessel filters, sampling frequency and derivative trigger thresholds. Some of these parameters have been set since the beginning of the data taking, chosen thanks to the experience acquired with CUORE-0; others needed more specific runs and some dedicated studies before being set. In fact, despite the experience with CUORE-0, we are dealing with a totally new system, hence the first few months were dedicated to a better understanding of the detector itself.

In this Chapter I will discuss some of the most important studies for the detector optimization on which I was personally involved during my PhD. These studies lead to a significant improvement of the data quality during the first few months after the CUORE cool down. For a full comprehension of this Chapter, in Table (3.0.1) I report some important quantities that will come useful in the following.

Temperature (mK)	Gain (V/V)	Bias Circuit Polarity	Load Resis. (GΩ)	Bessel Cutoff (Hz)	Sampling Freq. (Hz)
15	∼5000	Negative	60	120	1000

Table 3.0.1: *Important settings of the CUORE detector during data taking. The gain is not equal for all the channels: channels that show an higher signal have a lower gain set and vice versa, but the overall average is around 5000 obtained with the pre-amplifier set to 211 V/V and the PGA gain set to values around 25 V/V.*

3.1 Load Curves and Working Points

In Section (2.2) we saw the working principle of the bolometer technique and the importance of the bias circuit for the correct operation of the NTD as bolometric sensors. In this Section we elaborate on the notions introduced in Section (2.2.3) and we apply them to set the correct bias voltage to each bolometer of the CUORE detector. For this purpose, it is necessary to acquire special runs in order to build the load curves. Afterwards we need to check the overall uniformity of the sensors by acquiring an analyzing other special runs used to measure the obtained working points. From now on we will refer to these special runs as *LoadCurves* run and *WorkingPoints* run, respectively.

The main goal of the load curves procedure is to measure the characteristic I-V curve of the detectors. The working point must be identified along this curve such that it corresponds to the best SNR. This means that the chosen working point must maximize the signal amplitude and minimize the noise. At the same time we must pay attention in keeping a safe distance from the inversion point of the load curve: in fact, as we will intensively discuss in the following paragraphs, an excessive proximity to the inversion could cause from pulse deformations to instabilities in the measured signal.
The I-V curve is obtained by measuring the voltage drop across the bolometer sensors in static conditions [1] for many different values of the bias current which can be modified by

[1] Static conditions means that no pulses perturb the waveform when the voltage is measured.

changing the bias voltage of the polarization circuit of Figure (2.2.5). Intuitively we could measure the voltage drop by just getting the average signal value at the end of the readout chain, subtracting the FE offset and diving by the gain applied by the amplifiers. In fact the output signal (V_{OUT}) can be written as

$$V_{OUT} = (V_{OFF} + V_{bol}) \cdot G \tag{3.1.1}$$

where G is the gain introduced by the amplifiers in the readout chain, V_{bol} is the voltage drop across the thermistor and V_{OFF} is the offset summed to V_{bol} before the preamplifier such that the resulting signal fits in the ADC dynamic range.
Both the gain and the offset values are set or can be read by the DAQ through the SlowServer, thus in theory their value can be known precisely. However there are some additional contributions to the offset coming from the FE circuitry that cannot be known a priori. These contributions make our naive method to evaluate the voltage drop across the sensor unusable. Anyhow there is a workaround that we can exploit in order to eliminate such unknown contributions: by performing two measures of the output voltage with the opposite values of the bias voltage polarity, the unknown offset components are cancelled out. Equation (3.1.2) reports quantitatively what just said:

$$V^{\pm}_{OUT} = (V_{OFF} \pm V_{bol}) \cdot G\,, \quad \Rightarrow \quad V_{bol} = \frac{V^{+}_{OUT} - V^{-}_{OUT}}{2G} \tag{3.1.2}$$

where V^{+}_{OUT} and V^{-}_{OUT} are respectively the signals at the end of the readout chain for positive and negative polarization of the thermistor.
To plot the I-V curve we now need the current (I_{bol}) passing through the bias circuit for each value of the bias voltage (V_B) applied. I_{bol} is given by this espression

$$I_{bol} = \frac{V_B - V_{bol}}{R_L} \tag{3.1.3}$$

where R_L is the load resistance of the circuit shown in Figure (2.2.5), which value is reported in Table (3.0.1). Each point of the load curve is thus obtained with the I_{bol} and V_{bol} corresponding to each V_B applied. The whole load curve is then drawn by repeating the described measurement for different values of the applied bias voltage.

The working point measurement is carried out in a similar way, but only for one value of the bias voltage: once the bias and the gain are set, the circuit is maintained for few hundred seconds with the negative polarization, then the polarization is inverted and other few hundred seconds of signal are acquired. From the V^{+}_{OUT} and V^{-}_{OUT} we can therefore

measure I_{bol} and V_{bol} and calculate the thermistor resistance corresponding to a specific working point:

$$R_{bol} = \frac{V_{bol}}{I_{bol}} \tag{3.1.4}$$

3.1.1 Load curves

The first preliminary analysis to find the working point for each channel was performed in the second half of March 2017. It consisted in three runs, one for each subset of towers (from tower 1 to 6; from tower 7 to 12; from tower 12 to 19). The load curve measure is carried out by the EventBuilder process and by the SlowServer process which is intensively used in this kind of runs. At the beginning of the run the current electronics configuration is read so that at the end of the run it is possible to restore the original electronics configuration. The offset is then set to 0 V so that during the LoadCurve measurement the signal takes values in a range almost symmetric around zero. The gain is set to 211 V/V so that when the value of the bias voltage that corresponds to the inversion point is applied, the signal is still within the ADC dynamic range. During the load curve procedure the bolometer voltage is varied roughly from zero to few tens of mV for a certain number of times specified in a configuration file: after a bias is set, the DAQ acquires data for few hundreds of seconds at negative polarity, then the polarity is inverted and other few hundreds of seconds are acquired at positive polarity. Once one point is complete the polarity is switch again to negative, a new higher value of the bias is set and so on. In order to identify the optimal working point utilizing the SNR, a fixed energy reference pulse is fired about every 100 s exploiting the pulser control system described in Section (2.4). For this first set of load curves the amplitude of the pulser was set to 2500, correspondent to approximately 7 MeV. After each electronics configuration change, the DAQ assigns a different configuration ID to the data (configuration ID > 0) while the period of time during the electronics change are flagged with a null configuration ID, so that they are easily filtered out.
Figure (3.1.1) shows an example of LoadCurve run for one channel. The duration of the negative polarity was fixed requiring a minimum number of heater pulses, while the duration of positive polarity was fixed requiring a minimum number of noise events. In fact we use only the negative polarity to estimate the reference pulse amplitude, while the noise events of both negative and positive polarity are used to evaluate the I-V curve.

The first set of LoadCurves runs was done in order to find the maximum bias for each channel. This was necessary because if the bias is too high and beyond the inversion point on the V-I curve, the channel output will result unstable and eventually it will start

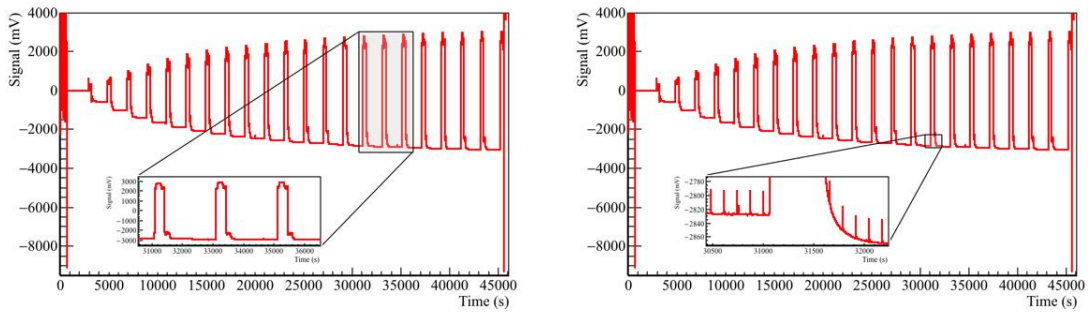

Figure 3.1.1: *Example of LoadCurve run which overall duration of a run is approximately 12 h. Left: zoom in of a section of the run where are visible the shift between negative and positive polarity for three values of the bias voltage. Right: zoom in of a portion of the run where are visible the reference pulses injected to evaluate the pulse amplitude trend as a function of the bias voltage.*

oscillating (Figure (3.1.2)). This phenomenon is called electrothermal feedback. The oscillation amplitude can be up to few Volts, influencing also neighbour channels (neighbours not geometrically in the detector, but on the same Front End board or crate).

A second set of LoadCurves runs was done in order to find a good working point for each channel. These runs had an average of 20 increasing bias values. This set of runs were really helpful to develop the algorithm to find the optimal working points. However after a brief data taking period[2] some problems arose with the bias applied to the channels: on one side there was same issue in the read/write accuracy of the electronics parameters and on the other side the amplitude chosen for the reference pulse was too high, hence it did not reflect the behaviour of the bolometer for an average signal (hundreds of keV). This distort for many channels our estimate of the optimal working point so that the chosen bias value was too close to the inversion point, leading those channels to an instability condition.

The first symptom of the instability condition is the deformation of low energy pulses, which in its extreme forms distorts the pulses in such a way that it appears to have two peaks, mimicking a pileup event. Within the analysis chain, events with more than one pulse are usually rejected to avoid pileup, so many of these deformed pulses are rejected from the subsequent analysis. The second symptom was the impossibility to stabilize those channels using reference heater pulses, resulting in double calibration peaks and bad resolution. Figure 3.1.3 is an example of a channel which spectrum shows "double peaks", particularly visible on the ^{208}Tl line.

[2]This brief data taking period was a complete dataset, including calibration, called dataset 3015.

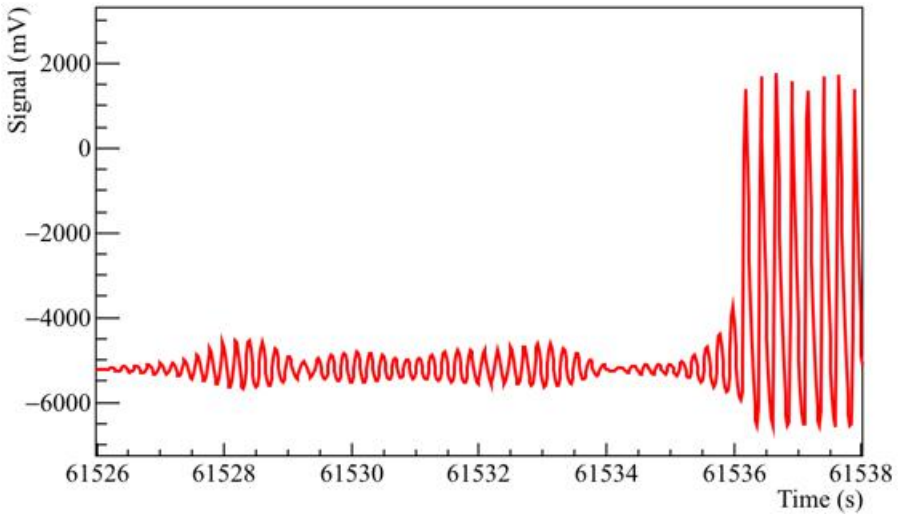

Figure 3.1.2: *Example of signal from one channel exhibiting increasing instabilities up to oscillations of the order of few volts: this channel had a bias voltage too high, so that it gets close to the load curve inversion point.*

These symptoms were not noticed during the analysis of the second set of LoadCurve runs because, as it was discovered later, the pulse deformation is energy dependent and it is less prominent at high energies, at which the reference pulse was set. We can see an example of pulse deformation in Figure (3.1.4) (left) showing average pulses obtained with heater pulses at different amplitudes: the pulse deformation is visible at all energies, but it is accentuated at low energy.
A third set of LoadCurve runs were acquired in the second half of April 2017 with the same configuration than the previous ones with the exception of the pulser which amplitude was set to 1000, corresponding to about 800 keV.
The list of the runs that was used for this third set of the LoadCurves is reported in Table (3.1.1).

Run Number	Towers	Date
301016	1 - 6	21-04-2017
301017	7 - 12	22-04-2017
301018	13 - 19	23-04-2017

Table 3.1.1: *Runs used for the final load curve analysis to set the optimal working points for all channels.*

Figure (3.1.4) (right) shows the same channel as Figure (3.1.4) (left); here the working

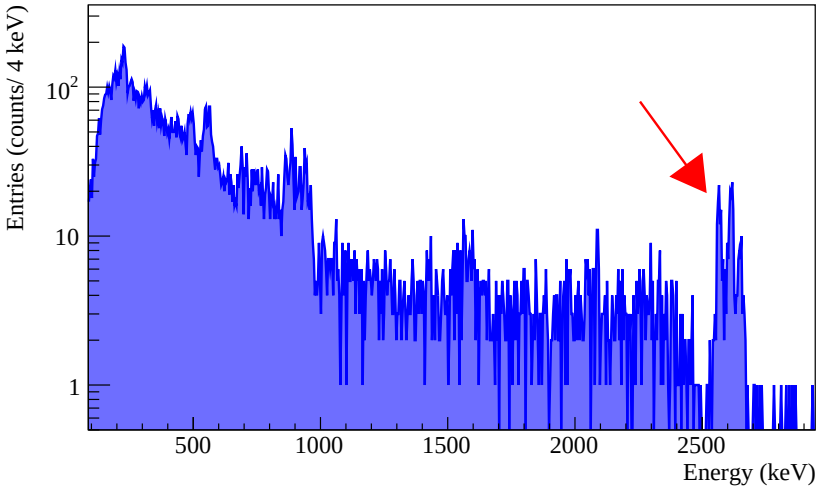

Figure 3.1.3: *Example of calibration spectrum for a channel which working point is close to the inversion.*

point for the channel has been chosen optimizing the 800 keV pulser response (low energy pulser Load Curves). This lead to a choice of a bias value in a region of stability for the channel and to an improved and more uniform pulse shape at several energies. In fact Figure (3.1.4) (right) does not show any hint of pulse deformation at all energies.

3.1.2 Algorithm to Find the Optimal Working Points

I want to remind that the value of the bias is chosen following some basic requirements: it has to maximize the signal to noise ratio and avoid pulse deformation that could rise for channels close to instability conditions.
In CUORE-0, which had 52 channels, the procedure for choosing the working points was not automatic. The optimal working point was chosen just looking at the load curve data (I_{bol} vs V_{bol}) and selecting a value of V_B intermediate from that corresponding to the maximum pulse amplitude A (in the A vs I_{bol} curve) and the one corresponding to the maximum SNR (in the SNR vs I_{bol} curve). However CUORE has 988 channels, hence an automated tool was developed to provide the working point bias voltage for all channels.
The automated working point search algorithm works following these steps for each channel:

1. get load curve data from the run corresponding to the selected channel and build the following plots: A vs I_{bol}, RMS vs I_{bol}, SNR vs I_{bol} (using noise and amplitude from both standard and filtered[3] signal), V_{bol} vs I_{bol};

[3]We will talk more about filtered signal in Section (4.1).

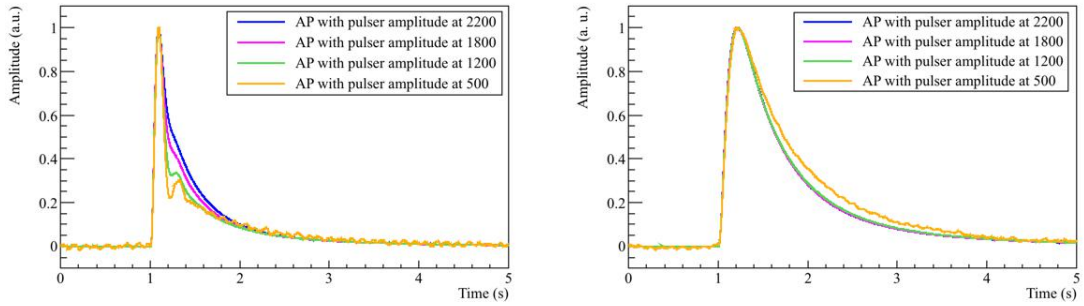

Figure 3.1.4: *Left:example of AP at different energies of channel 97 for which the energy dependence of the pulse deformation is clearly visible. Here the working points had been set to optimize the pulser@2500. Right: example of AP at different energies of channel 97, with the updated working point, which was set to optimize the pulser@1000. The pulse doesn't show any deformation even at lower energies.*

2. find the maximum on A vs I_{bol} curve and get the corresponding V_B;

3. find the maximum on SNR vs I_{bol} curve and get the corresponding V_B.

The first analysis step is getting all the different curves that we will use to extract the optimal working point. In Figure (3.1.5) there is an example of all the curves built in point 1) of the "find working point" procedure.
The blue curve is the actual load curve: each point correspond to a V_{bol} - I_{bol} pair for a set bias voltage V_B. The maximum of this curve is the inversion point[4]. This curve is built using only noise events of both polarities, eliminating those events having pulses in it or being too close to the polarity inversion.
The red curve describes the trend of the amplitude of the reference pulse with respect to the current passing in the NTD, I_{bol}. This curve can be built with two methods both using only signal pulses induced by the heater of the negative polarity waveforms. The fist method consists in evaluating the amplitude of each pulse (the height of the pulse with respect to the baseline) and obtaining each point of the curve by averaging together the amplitudes obtained at a same bias configuration. The second method consists in doing the average of all the heater pulses of a same bias configuration, building an Average Pulse (AP), thus each point of the curve is the amplitude of the average pulse of a single bias voltage value. In the latter case, when averaging the pulses, most of the noise frequencies present in the waveforms cancel each other out, obtaining a better evaluation of the pulse amplitude. For this reason from now on we will use only the amplitude evaluated from the AP. In both cases events showing pileup or too close to the polarity inversion are eliminated.

[4]Note that with respect to the load curve sketched of Figure (2.2.6), the axis of this curve are inverted.

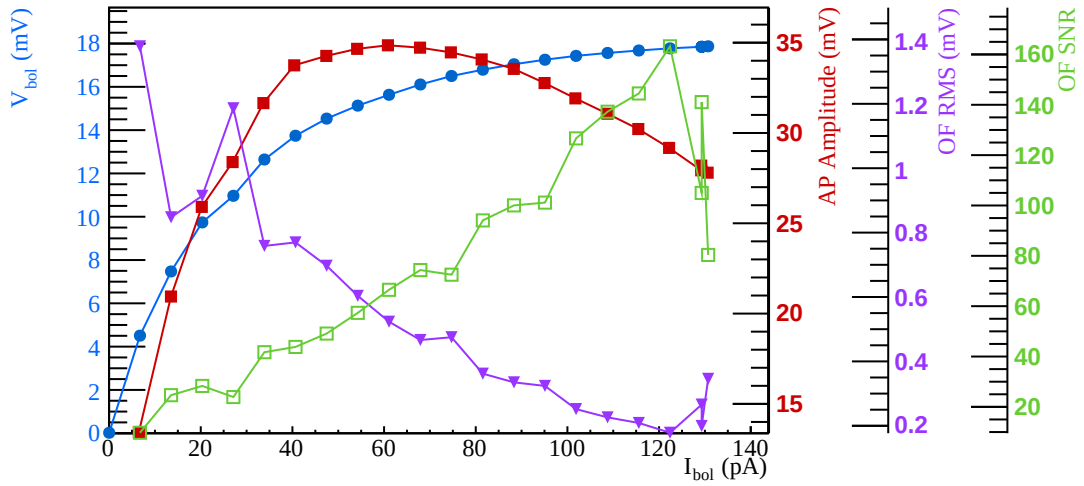

Figure 3.1.5: *Example of the Load Curve Plots that are produced for each channel (here for Channel 831 Run 301018) and utilized for the analysis.*

Also for the evaluation of the RMS there are two possible methods. In both cases the RMS is measured on all the noise events of both polarities, eliminating those events having pulses in it or being too close to the polarity inversion. The fist method consists in evaluating the standard deviation of samples of the noise events about the baseline; the second one uses instead the optimum filter built on all the noise and signal events of each bias configuration. The optimum filter, described in Section (4.1), attenuates in the event Noise Power Spectrum (NPS) the frequencies that do not contribute to the signal events, thus leaving mostly the low frequency components of the noise. The RMS is then evaluated by integrating the NPS. From now on we will use only the latter method to evaluate the RMS since it select only the noise components that could spoil the amplitude evaluation, hence the energy resolution. The purple curve in Figure (2.2.6) represents the RMS computed from filtered waveforms. This curve is the one that suffers more for lack of statistics, random fluctuation of the noise and presence of small not triggered particle pulses; the curve is in fact not smooth and sometimes it is difficult to identify a clear trend. This last problem could be mitigated acquiring more data, but in that case the measure should be much longer.

Lastly, the green curve is the SNR computed using the amplitudes evaluated from the AP and the RMS from filtered waveforms and thus called *OF SNR*. The sharp variation in this curve are due to the bumps in the RMS curve, but later in this section we will see the workaround to smooth out the RMS, hence the SNR, curves.

In building these curves there are some precautions that one must take before finding the working points. A check is run on all the above curves to remove possible (still) oscillating points as well as points in which the evaluation of the pulse amplitude variable (or RMS, or V_{bol}) failed. These points could lead to a wrong evaluation of working points. An example is reported in Figure (3.1.6) where one point of the amplitude curve is an outlier compared to the rest of the curve; this can be caused by a physical coincident event in the same crystal or to an error in the amplitude evaluation. When looking for the maximum of the amplitude curve, the presence of this outlier could lead to a fake maximum.

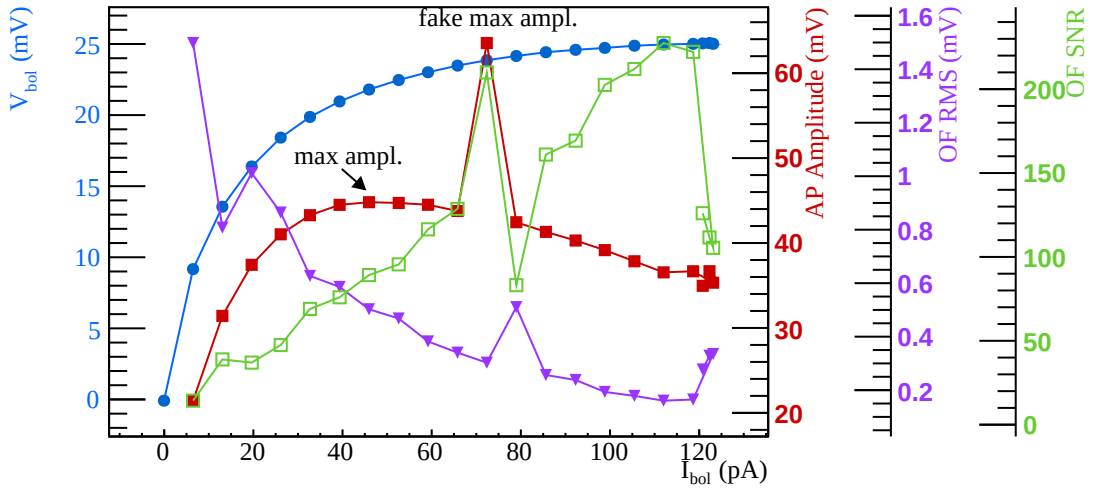

Figure 3.1.6: *Example of load curve plots for channel 19, in which a fake maximum of pulse amplitude curve is identified by the algorithm; it is therefore skipped and the real maximum of the curve is found.*

Moreover a check on the V_{bol}-I_{bol} curve was performed, to identify its maximum as the NTD inversion point. Load curve points with bias voltages nearby the inversion point and beyond it were not utilized for the "find working point" algorithm. The analysis for finding the optimal working point is then performed only on the load curves points which pass all the above safety checks.

The last problem to be solved is the fact that the RMS and thus the SNR curves are jagged. If we assume that the main contribution to the detector noise is due to the Johnson noise of the resistances we have that the RMS due to the NTD resistance at the operational temperature is

$$RMS_{bol}^2 = 4k_B R_{bol} T_{bol} \tag{3.1.5}$$

where k_B is the Boltzman constant. The sensor is biased using a load resistance R_L as illustrated in Figure (2.2.5) of the previous Chapter, which is in general at room temperature T_L, thus giving alone a RMS of

$$RMS_L^2 = 4k_B R_L T_L \tag{3.1.6}$$

always assuming that the thermal white noise is the main contribution to the RMS. These two resistances are in parallel, thus the RMS on the output voltage of the bolometer becomes

$$RMS_{det}^2 = \frac{RMS_L^2}{R_L^2}\left(\frac{R_{bol}\cdot R_L}{R_{bol}+R_L}\right)^2 \simeq 4k_B T_L \cdot \frac{R_{bol}^2}{R_L} \tag{3.1.7}$$

in the approximation that $R_{bol} \ll R_L$. Therefore, assuming the RMS is dominated by thermal noise, it is linearly proportional to the NTD resistance which in turn depends from both the operational temperature and from the V_B imposed to the circuit. The thermistor resistance R_{bol} can be calculated for each V_B as V_{bol}/I_{bol}. We perform a linear fit of RMS vs R_{bol}, in a range of R_{bol} that covers only the NTD stable region of operation. An example of the fit is shown in Figure (3.1.7) (left). In the end, instead of using the actual RMS we use the values extrapolated from the fit. The values extrapolated for the RMS are eventually used to smooth the SNR curves as illustrated in Figure (3.1.7) (right).

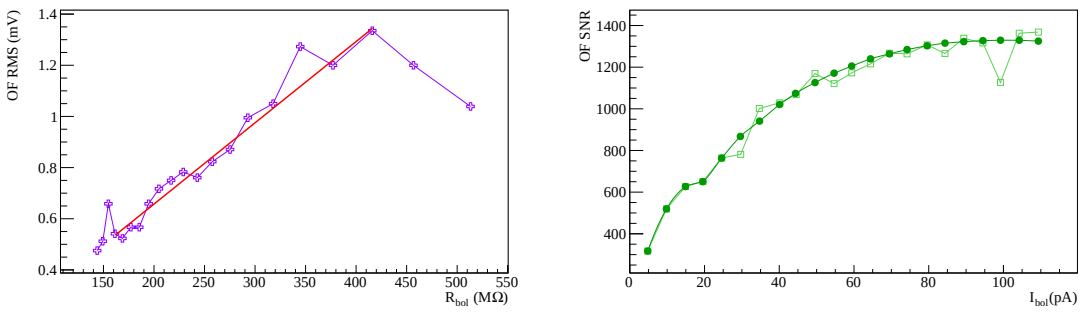

Figure 3.1.7: *Left: example of the RMS versus R_{bol} fit in order to smooth the SNR. Right: SNR curve before and after the smoothing process. The curve now is more homogeneous than before allowing the "finding working point" algorithm to work better.*

The outcome of this operation is shown in Figure (3.1.8).
Finally, in order to find the working point the algorithm looks for the SNR maximum given that the bias voltage is between the maximum on the amplitude curve and two steps before the inversion point. The SNR maximum and the maximum amplitude are indicated in Figure (3.1.8) as two vertical lines: the red line points to the I_{bol} corresponding to maximum

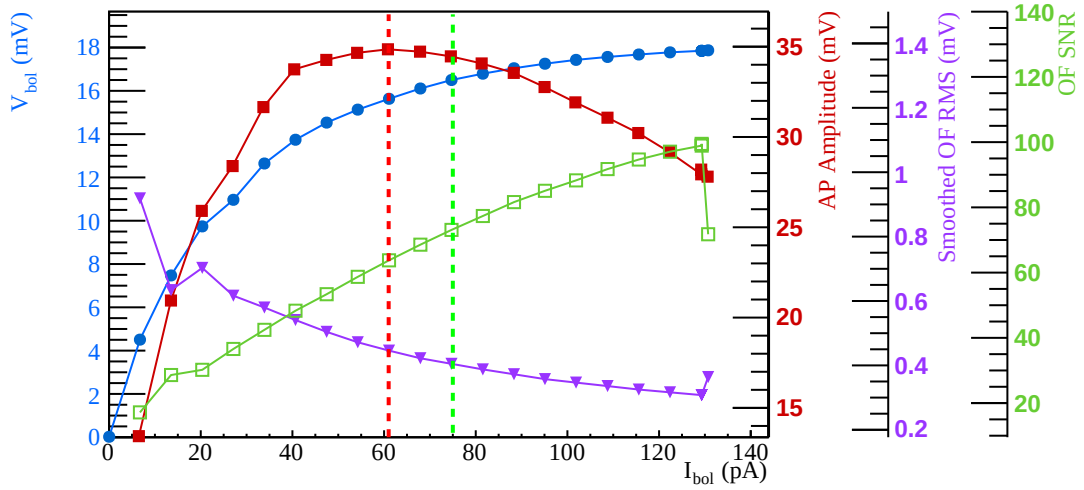

Figure 3.1.8: *Example of load curve plots from run 301018 channel 831. The dashed red vertical line indicates the maximum of pulse amplitude while green dashed line points to the maximum of SNR curve. Here the working point is set to the bias voltage value corresponding to the maximum of SNR curve. The RMS (and therefore the SNR) plot has been smoothened through the linear fit of the RMS vs R_{bol} distribution.*

amplitude while the green line points to the I_{bol} corresponding to SNR maximum. The V_B corresponding to this last point is the optimal working point.

Among the 988 CUORE bolometers, there are approximately 30 channel without a functioning heater which means that it is not possible evaluate the pulse amplitude as a function of the bias using the heater pulses. In case of channels without heater or with not enough good points on the load curves (less than 4 points on the load curves - approximately 20 channels), the algorithm provides a V_B for the working point at the conservative value of 3 V, which is lower than the average bias voltages applied to the other channels. In fact we prefer to have a slightly worst SNR or a lower pulse amplitude, than risk to have oscillating channels whose crosstalk could spoil also neighbouring channels.

Checking pulse shape at maximum SNR

The pulse shape has been investigated since it is a good figure of merit to identify channels getting to instability condition. Sometimes the selected working point is still in a region of high bias, where the pulses can be deformed due to the proximity to the inversion point. In order to prevent pulse deformation, a check on the pulses at maximum of the SNR curve

was made. In case the pulse at that point resulted deformed, the previous point on the SNR curve was taken as the optimal working point. This check was done iteratively on all the chosen working points up to the V_B corresponding to the maximum of the amplitude curve.

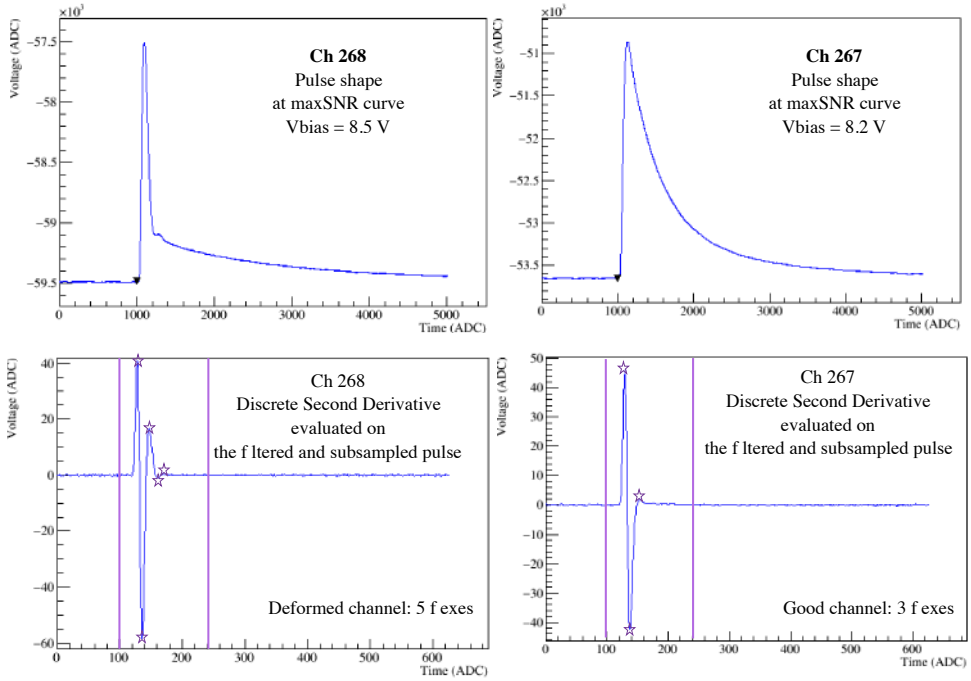

Figure 3.1.9: *Top: example of pulses from the load curve run 300899. Channel 268 (left) shows a clear deformed pulse shape while channel 267 (right) has the expected pulse shape when the optimal working point is set. Bottom: discrete second derivative of the top pulses for Vb_B corresponding to the maximum of SNR curves. The number of flexes identified on the second derivative - depicted here with a star - allows the discrimination between stable channels (ch 267 - 3 flexes) and unstable/deformed ones (ch 268 - 5 flexes).*

The pulse deformation was quantified in terms of number of flexes of the pulse. The waveform of each reference heater event was filtered to remove high frequency noise and sub-sampled to 125 Hz because we are only interested at deformations in the frequency range of the pulse. The flexes are found on the discrete second derivative of the resulting waveform of the pulser events. When the NTD is operating in stable conditions 2-3 flexes would be identified on its signal, depending on how much the decay time constants are coupled; deformed pulses would have instead more than 3 flexes.

In conclusion, following the guidelines presented up to know, we were able to choose for each channel the correct bias voltage, optimizing the pulse amplitude and the signal to noise ratio and avoiding pulse deformation. These bias voltage values applied to the bolometers at a base temperature of 15 mK are reported in Figure (3.1.10). The values cluster around voltage values distant about 300 mV due to the fact that the load curves have been acquired with a finite number of bias values.

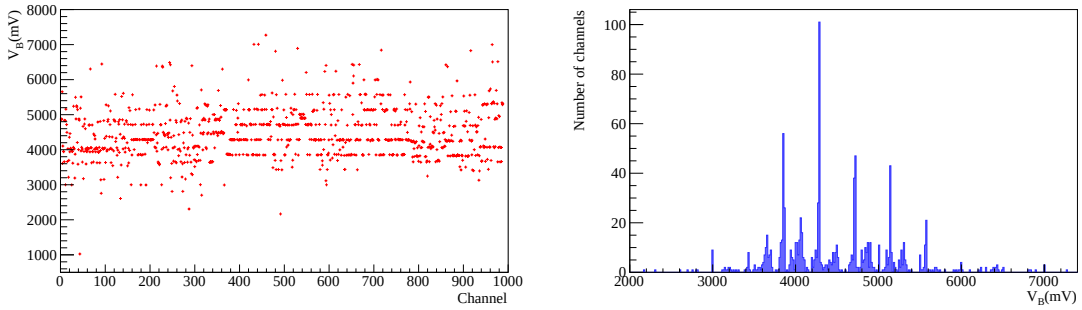

Figure 3.1.10: *Left: distribution of the bias voltages applied to the NTD as a function of the channel number. Left: overall distribution of the bias voltages.*

3.1.3 Working Point Measurement

Once the working point has been chosen, we can measure the static resistance of the NTD of each channel, which depends on the NTD itself, on the detector temperature and on the chosen bias voltage. The purpose of working point measurement is to understand the value of the NTD resistance and monitor it in time to verify its stability. This is why this measure is done not only after the load curves, but it is also repeted periodically.
In order to obtain this measurement for all bolometers we can use the same Diana sequence used for the Load Curves, with some differences in the procedure:

- the pulser is never fired since only noise events are needed;
- the bias voltage remain fixed;
- the sleep time after each electronics change, either bias setting or polarity inversion, is longer (usually about 1200 s).

The last point is extremely important in order to have an accurate measure of the NTD resistance and offset: every change in the electronics has the unwanted effect of worming

up the entire system, thus we have to wait enough time so that the bolometers have the time to return to their base temperature. If we do not wait enough time the measured resistance will not correspond to the sensor resistance during data taking.
In general, the overall duration of a Working Point run is much shorter than the Load Curves runs since there is only one bias value to measure and one polarity inversion. Also here, like for the Load Curves, the Diana sequence that allows to acquire the data and drives the slow control also writes into the data files some configuration IDs: to each electronics configuration taken, it is assigned a different configuration ID with the exception of the transition periods between one configuration and the next which assume a null configuration ID. In this way it is very easy in the offline analysis to filter out the moment in which the electronic parameters are changing, that usually correspond to chunk of very noisy waveform on all the channels of each FE board, due to the crosstalk.

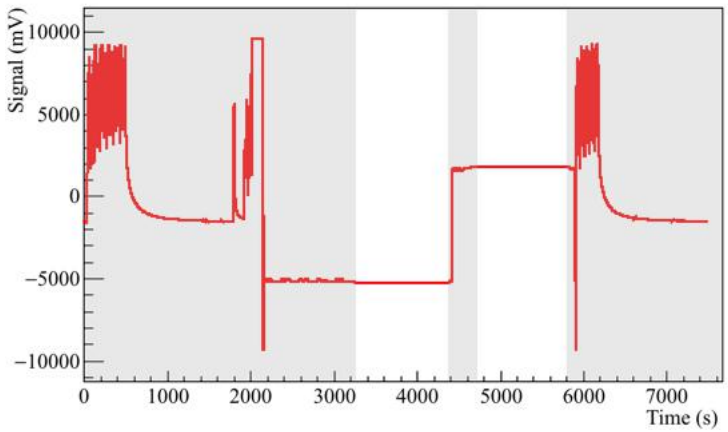

Figure 3.1.11: *Example of a working point run for one channel. The red line is the signal waveform; the grey shaded areas indicate where the signal is ignored by the offline analysis; the remaining waveform is divided in two regions: the first has negative polarization of the bias circuit, the second has positive polarization.*

Figure (3.1.11) report an example of working point run for one channel: the shaded areas are ignored by the offline analysis since they have a null configuration ID.
In order to measure the voltage for the negative and positive polarity, only noise events with no pulses in them are selected. The average signal of the negative polarity part of the waveform is the V^{-}_{OUT} while the average of the positive polarity section of the signal is V^{+}_{OUT}. V_{bol} and I_{bol} are obtained from Equation (3.1.2) and Equation (3.1.3), respectively, and the static resistance of the thermistors is computed from Equation (3.1.4) and the two previous equations.

Finally in Figure (3.1.12) the distribution of the so obtain bolometer resistances are shown.

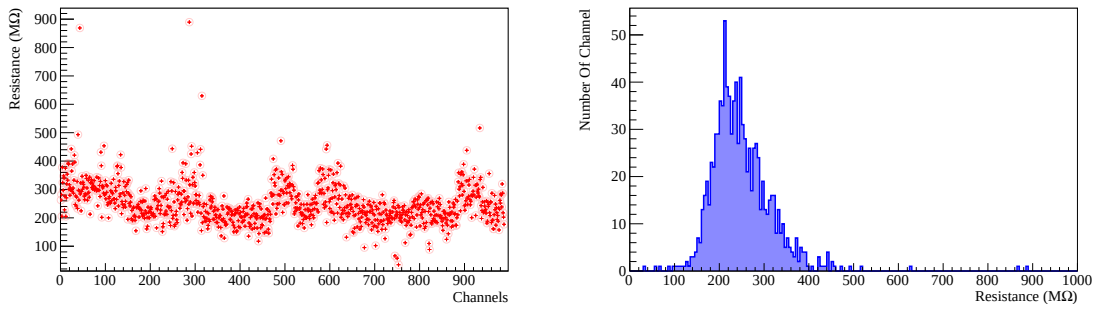

Figure 3.1.12: *Left: graph representing the static NTD resistance for each channel in the detector. Right: overall distribution of the resistances at the optimal working point - the wide spread of the resistance values is due to the use of three different types of NTD with slightly different behaviour.*

3.2 Derivative Trigger Thresholds

Given the low sampling frequency, CUORE exploits an online derivative trigger which runs at the level of the DataReader on the shared memories (see Section (2.4.2) for more details). The derivative trigger role is identifying particle induced pulses at all energies. An online trigger is necessary to have an immediate validation of what is happening in the detector, but if necessary, the continuous data are also saved and can be retriggered offline with the derivative trigger or other triggering algorithms available within the Apollo software. The trigger position is then used by the EventBuilder to save the event in the RawData files, input of the offline analysis. CUORE bolometers have a variety of behaviours, thus their characteristic noise is often very different; the derivative trigger must take these differences under consideration and the algorithm must be able to adapt to the peculiar needs of each detector channel. This is the reason why the parameters of the derivative trigger algorithm must be tuned channel by channel. In CUORE-0, that had only 52 channels, this operation was done by hand; since now we have slightly less than 1000 channels, it is understandable that this tuning cannot be perform anymore by hand but an automatic procedure is necessary.

In this Section I will present the procedure that I developed to find, optimize and then check the derivative trigger parameters.

3.2.1 Derivative trigger algorithm

The derivative trigger works on the derivative of the waveform. There are four parameters that characterize the derivative trigger algorithm, itemized and accompanied by a brief description in the following list:

- *threshold* (mV/ms): minimum derivative of the signal to get the trigger to fire;
- *average* (ms): region in which the derivative is computed;
- *debounce* (ms): time for which the derivative must be above threshold in order to save the trigger flag into the event;
- *dead time* (ms): establishes the minimum time length between a trigger and the next one.

In this implementation of the trigger algorithm, we have a trigger if the statement

$$\frac{(signal[i + average] - signal[i])}{average} > threshold \tag{3.2.1}$$

is true for at least a minimum number of consecutive samples. The number of samples, or the corresponding time in milliseconds[5], for which the requirement must be true, is called *debounce* (see figure Figure (3.2.1)). The index i runs on all the signal samples that are in the circular buffer of the shared memories. For the pulses that pass this requirement the derivative trigger flag is positioned at the first $signal[i + 1]$ for which the trigger condition is true.
This implementation of the trigger requires the pulse slope to be always above threshold and therefore it acts only on the rise time of the pulse that for CUORE is between 100 and 250 ms long or even less for small pulses in noisy channels, where the noise highly influence the pulse shape.
Indicatively we want the average and debounce set to a fraction of the rise time, the dead time as a fraction of the decay time of the pulse and the threshold slightly above the baseline noise in order to identify also low energy events.

3.2.2 Derivative trigger parameters

The procedure to find the optimal trigger parameters is divided in two phases: a first phase designed to pick a guess value for all the parameters and a second phase to identify the optimal values around the guessed ones.

[5] All derivative trigger parameters are defined in the time domain in order to be independent from the specific choice of sampling frequency.

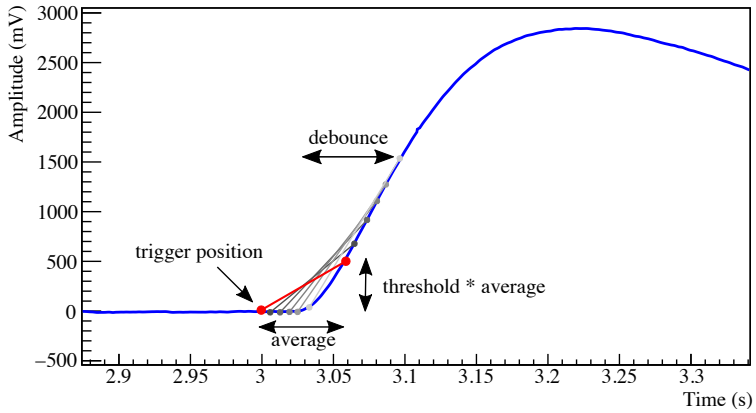

Figure 3.2.1: *Functioning scheme of the derivative trigger algorithm.*

In the first phase, the choice of the initial derivative trigger parameters is based on the autocorrelation of the characteristic noise of each channel.

We need to acquire a noise run, namely a run where the rate of the noise events acquired is higher than average (one noise trigger every 10 - 20 s). This kind of run allows to have enough statistics on the noise of each channel in a short time (few hours). During the offline processing of the noise run aforementioned, only noise events are selected. For each noise event of a specific channel the signal is modified in order to have flat waveform with null mean (see Figure (3.2.2)), then the autocorrelation of the signal is calculated as

$$R_{y,y}(x) = \frac{1}{N}\Sigma_{n\epsilon\mathbb{Z}}\, y(n) \cdot y(n-x) \tag{3.2.2}$$

with n that runs over all the samples of the waveform and N the total number of samples (1000 samples for the current DAQ configuration). The resulting signal is then averaged over all the events of a single channel. Figure (3.2.3) report the resulting autocorrelation for two channels, showing how much the autocorrelation function reflects the characteristic noise of the event.

If we do not want to trigger on noise oscillations, the *average* has to be larger than the period of the dominant frequency of the channel or the region with the highest autocorrelation: the best situation is when the *average* on which the signal derivative is calculated corresponds to the distance between the maximum and the first minimum of the autocorrelation in order not to be sensitive to the noise frequencies that dominate the channel (see figure Figure (3.2.4)). This however is not always possible because the sum of *average* and *debounce* has to be within the rise time of the pulse and at the same time it has to be

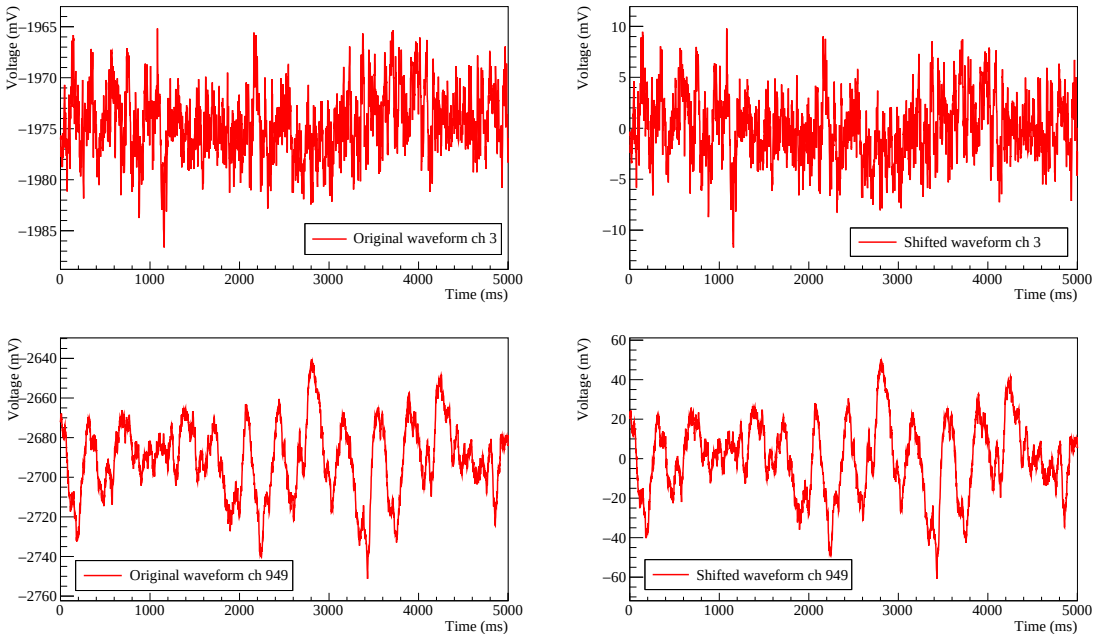

Figure 3.2.2: *Example of a noise event for two channels with a different characteristic noise. Left: the original signal. Right: the original signal has been flattened and the waveform has been shifted in order to obtain a signal with null mean.*

enough to get a meaningful sample of the rise time of the event:

$$average + debounce < max\_position - trigger\_position \tag{3.2.3}$$

where $max\_position$ is the time of the sample corresponding to the maximum of the pulse and $trigger\_position$ is time of the position of the trigger flag. *Average* and *debounce* are hence bounded to be within the range 20 ms - 100 ms. The y component of the *threshold* is chosen instead to be the square root of the maximum value of the autocorrelation, which is proportional to the baseline RMS of the signal.

After introducing the algorithm used to automatically find the derivative trigger parameters for 988 channels, we can go back to reality: the first problem is the noise variability. In fact some channels experience a sudden change of the noise condition, reaching double or half of their initial baseline RMS sometimes after small earthquakes or due to induced vibrations on the detectors or because of some change in the environmental conditions of the FE electronics. Whichever the cause, this unstable condition of the channels noise was strongly attenuated after the optimisation campaign that happened between the first and the second period of the data taking used for the analysis presented in this Thesis.

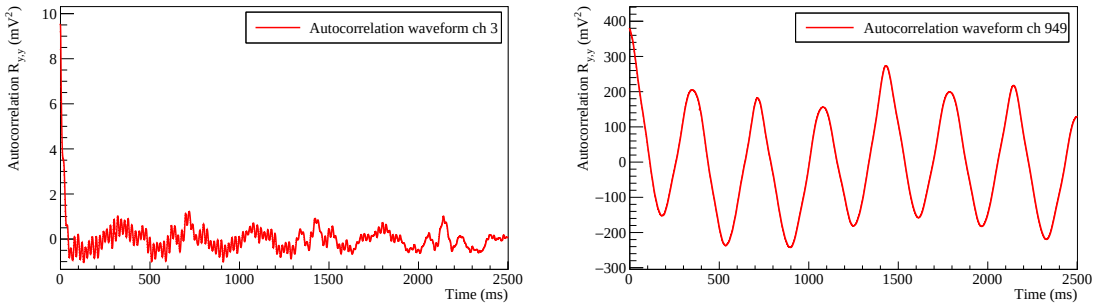

Figure 3.2.3: *Example of signal autocorrelation computed from the two noise events of Figure (3.2.2).*

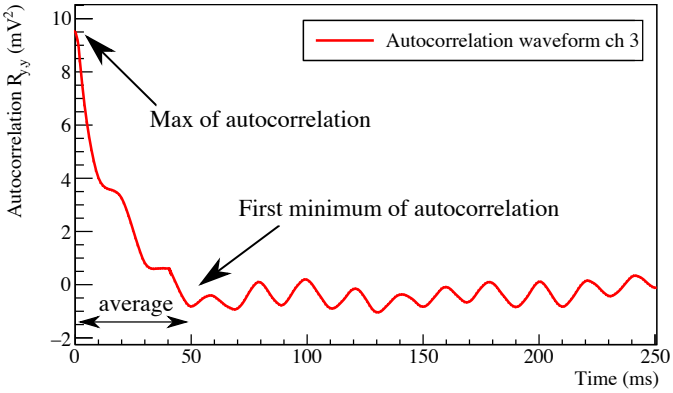

Figure 3.2.4: *Scheme on how the derivative trigger parameters are set.*

However this problem pointed out that having all the trigger parameters noise dependent it was not always an advantage, and conversely the fact of having so many free parameters was making the trigger algorithm unreliable. The second problem is that often the value found for *average* is above or below the range limits, hence forcing their value to be either 20 ms or 100 ms. For all the above reasons *average* and *debounce* have been set to the value used in CUORE-0: 40 ms. In CUORE-0 the *dead time* was set to 1000 ms, but for CUORE we choose to set it to 800 ms which is a fair value considering that the decay time of a pulse is within few hundreds of milliseconds to few seconds. In fact the *dead time* must be long enough to let the trigger algorithm to work and don't trigger twice on the same pulse and at the same time it must be short enough to be sensitive to pileup events that may happen on the decay time of the previous pulse.

The only remaining parameter to be set is the *threshold* which initial value is

$$Thrs_0 \equiv \frac{dV}{dt} = \sqrt{R_{y,y}(0)} \; . \tag{3.2.4}$$

where $R_{y,y}(0)$ is the maximum of the autocorrelation. The second phase of the procedure to set the derivative trigger parameters regards indeed the evaluation of the optimal trigger threshold starting from the guessed value from Equation (3.2.4).
We select again only noise events from the noise run. The threshold is varied around its guessed value on both directions and each time we use the set of trigger parameters obtained to apply to the noise events an offline algorithm that simulates the online `Apollo` derivative trigger. For each value of the threshold around the initial value, for each channel the trigger rate on the noise events is computed and written to file. Later, for each channel, we build a curve representing the trend of the trigger rate with respect to the threshold value. An example of such curve is depicted in Figure (3.2.5) (left).

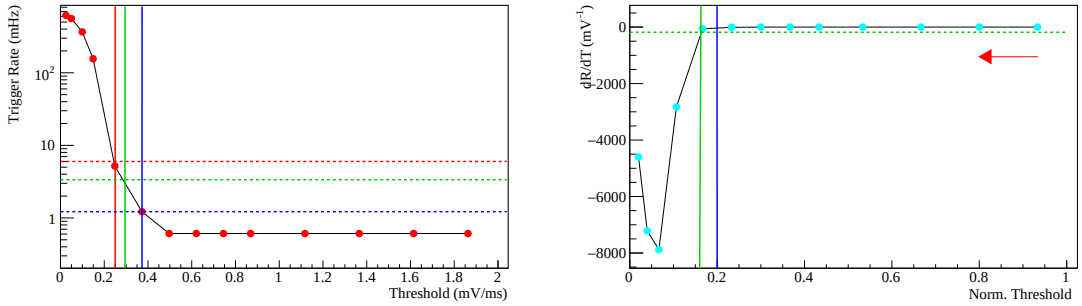

Figure 3.2.5: *Left: trend of the trigger rate on noise events as a function of the derivative trigger threshold. The blue vertical line indicates the initial value for the threshold, while the green and red lines are the thresholds corresponding to condition 1) and 2) of Equation (3.2.5), respectively. Right: derivative of the trigger rate with respect to the normalized threshold where the blue vertical line indicates the threshold initial value and the green one corresponds to condition 1) of Equation (3.2.5). The red arrow point the direction of the algorithm iterations to check the over-mentioned conditions.*

If the current threshold is too low we start triggering on the noise up to the maximum event rate which is established by the *dead time*: when the threshold is too low, the trigger fires as soon as the *dead time* ends, hence every 800 ms. If the current threshold is instead too high either the trigger never fires or it fires only few times, whenever it finds a pulse in coincidence with a noise event. The optimal threshold is placed in the middle of this two extreme situations, preferably in the point in which the trigger rate on the noise events is going to become constant, thus where the slope changes. To find such

point we use two possible criterion: the one that is first found to be true, determines the derivative threshold value. The first criteria utilizes the first derivative of the event rate versus threshold curve of Figure (3.2.5) (left), normalising the abscissa values to one, for computational reasons. This derivative is reported in Figure (3.2.5) (right). We divide the curve of the rate derivative in 1000 steps and, starting from the maximum of the abscissa, we step back towards lower values and at each step we check if both the following condition are complied:

$$\begin{aligned} &1) \quad dR/dT \leq -150\, mV^{-1} \\ &2) \quad T \leq T_{max} \equiv 6\, mHz \end{aligned} \tag{3.2.5}$$

where R is the trigger rate, T is the current value of the threshold and T_{max} is the maximum value of the trigger rate on noise acceptable during background data taking. The limit value of -150 mV^{-1} in Equation (3.2.5) have been chosen empirically without following any particular criterion, while 6 mHz has been chosen because it is approximately of the same order of the expected signal trigger rate. As soon as one of the two conditions is not satisfied anymore the algorithm stops and saves the corresponding threshold value as the optimal derivative trigger threshold. In Figure (3.2.5) (left) the thresholds corresponding to condition 1) and 2) are marked respectively with a green and red vertical line. Figure (3.2.6) reports in green (triangular markers) the optimal derivative trigger threshold for all the channels and for comparison, in blue dots, the correspondent initial guess values.

From this last figure is clear that this second phase of the procedure to find the derivative trigger thresholds allows to lower the energy thresholds, thus making accessible the lowest part of the energy spectrum.

In Chapter (4) I will describe the analysis of two datasets, each one approximately one month long. To each dataset is associated an identification number, in this case DS 3018 and DS 3021 for the first and second dataset respectively. Between the first and the second dataset we stop taking data for one month, dedicated to the detector and analysis optimization. It is out of the purpose of this section to describe the differences of these datasets, but I want to point out that for the first dataset (DS 3018) we set the trigger parameters using only phase one of this procedure, while for the second dataset (DS 3021) we used the complete procedure which results in lower energy thresholds and better reliability as you will be shown at the end of Section (3.2.3).

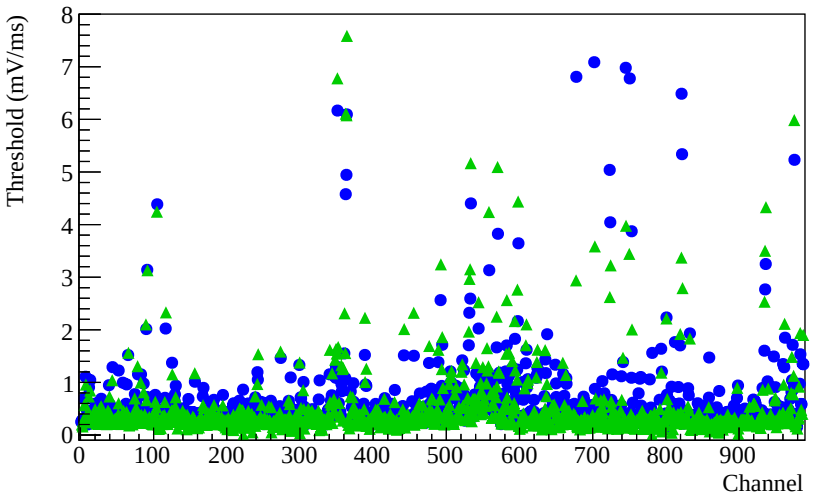

Figure 3.2.6: *Distribution of threshold parameters used in the derivative trigger algorithm, as a function of the channel number. The blue dots are the initial guess values obtained with the signal autocorrelation, while the green triangles are the optimal values obtain with the second phase of this procedure.*

3.2.3 Evaluating Derivative Trigger Efficiency

Few test runs were acquired after setting the derivative trigger parameters to check the trigger efficiency for each channel. As a figure of merit for the quality of energy thresholds we used the 90% of the trigger efficiency. The rest of this section will be dedicated to describe the procedure to get the distribution of the energy thresholds at 90% of trigger efficiency.

The test runs used in this study are called *NPulser* runs and are characterized by multiple heater pulses at different amplitudes in the low energy part of the spectrum. The number of different values of pulser amplitudes and the number of repetition of each amplitude is determined by the uncertainty that we aim to obtain on the trigger efficiency uncertainty and the resolution that we want to achieve in the evaluation of the energy thresholds. However, in order to accommodate the data taking schedule, we must try to keep the measure short. In this case we adopt a configuration with 8 different pulser amplitudes from few keV to about 1000 keV, each one repeated in average 12 times during the duration of the run ($\sim$ 14 h).

The *NPulser* runs used to check the energy thresholds are run 301120, for dataset 3018, and run 301511 for dataset 3021. The analysis procedure was carried out up to the energy evaluation so that we can extract the energy corresponding to each pulser amplitude (see

Section (4.1) for detailles on data production). For the channels failing one of the steps of the analysis sequences, the energy of each pulser amplitude is assigned using the average energy found for the same pulser amplitudes in other channels. For the channels that for some reason fail one of the steps of the analysis sequences, the energy of each pulse amplitude is assigned using the main energy of that pulse amplitude found on the energy spectrum of every other channel together. These values are reported in Table (3.2.1) for the two datasets.

Pulser Amplitude	Energy (keV) Dataset 3018	Energy (keV) Dataset 3021
100	6	4.5
200	19	23
250	35	41
300	53	63
350	79	92
400	110	128
600	300	338
1000	970	1064

Table 3.2.1: *Indicative energies for each pulser amplitude for the first and second datasets. The energy is the mean of the energy distribution for each pulse amplitude, using calibrated data.*

The analysis procedure selects only events that are pulser events, with no pileup in it and with only one trigger. Note that in case of pulser events, if a second flag from derivative or noise trigger is found within 100 ms from the pulser flag, the event still considered single triggered. On the selected pulser events, the analysis procedure checks if the derivative trigger has fired within 100 ms from the heater flag, and in that case it sets the event variable `Triggered` to true. At the same time the analysis procedure counts the number of pulser events for each pulser amplitude of each channel. Then the algorithm compares, for each pulser amplitude - channel pair, the number of pulser events detected with the number of pulser events expected, providing the detection efficiency. The pulser detection efficiency is therefore defined as

$$Eff(ch, A) = \frac{\tilde{N}(ch, A)}{N(ch, A)} \tag{3.2.6}$$

where ch is the channel ID, A indicates the amplitude of the pulser, enumerated in Table (3.2.1), $\tilde{N}(ch, A)$ is the number of heater events detected for each channel and each pulser amplitude while $N(ch, A)$ is the number of expected pulser events for each channel

and pulser amplitude.

The efficiency uncertainty is the binomial standard deviation:

$$Eff\_err(ch, A) = \sqrt{\frac{Eff(ch, A) \cdot (1 - Eff(ch, A))}{N(ch, A)}} \tag{3.2.7}$$

Note that to easily fit the efficiencies, to the point with null uncertainty (efficiency=1 or efficiency=0) the uncertainty was assumed equal to:

$$Eff\_err(ch, A) = \sqrt{\frac{[(N-1)/N] \cdot [1 - (N-1)/N]}{N}} \quad if\ efficiency = 1 \tag{3.2.8}$$

$$Eff\_err(ch, A) = \sqrt{\frac{1/N \cdot (1 - 1/N)}{N}} \quad if\ efficiency = 0 \tag{3.2.9}$$

where $N \equiv N(ch, A)$ for better readability of the equations.

Plots in Figure (3.2.7) represent the efficiency value as a function of the channel, for three of the eight pulser amplitudes, from the highest to the lowest respectively from top to bottom. After obtaining the efficiencies, we need to quantify the position of the energy thresholds resulting by applying the derivative trigger parameters found following the procedure described in Section (3.2.2).

The efficiency as a function of the pulser energy was fitted using a logistic (or sigmoid) function:

$$f(x) = \frac{1}{1 + e^{-k(x - x_0)}} \tag{3.2.10}$$

with k and x_0 left as free parameters and indicating the steepness of the curve and x-value of the sigmoid's midpoint, respectively. The fitted function was inverted in order to evaluate the function at 90% of the efficiency and obtaining the desired energy threshold value.

$$x = f^{-1}(y) = x_0 - \frac{1}{k} ln\left(\frac{1 - y}{y}\right)\Bigg|_{0.9} \tag{3.2.11}$$

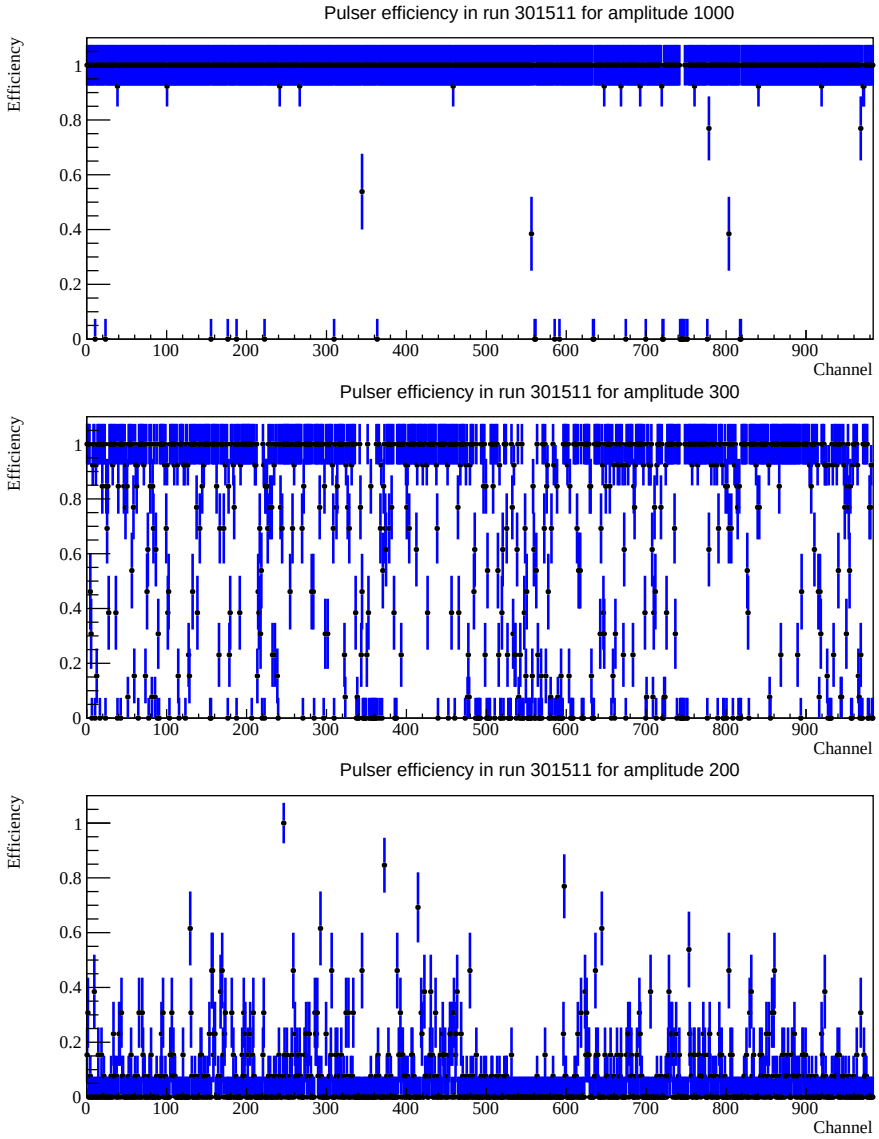

Figure 3.2.7: *Efficiency for all the channels at three of the eight different pulser amplitudes: from top to bottom amplitude 1000 (∼1 MeV), 300 (∼60 keV), 200 (∼ 20 keV). The channels that in the top figure have zero efficiency are the channels without a functioning heater chip.*

In Figure (3.2.8) are represented two examples of efficiency curves: each point represents the detection efficiency for that particular channel at a specific energy. The vertical green line in both plots of Figure (3.2.8) represents the position of the energy threshold value at 90% of trigger efficiency. The only channels for which we do not have a quantitative estimate of the energy threshold are those without heater for which is impossible to see

any pulser event and are hence excluded from this analysis.

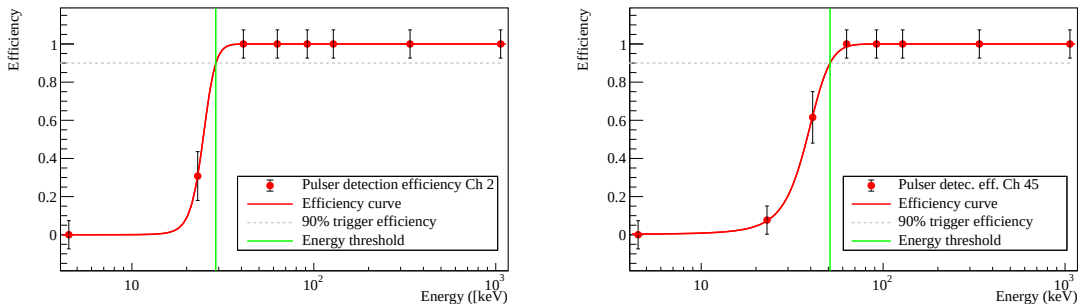

Figure 3.2.8: *Example of trigger efficiency curve (red line) and threshold (green line) for six different channels.*

Finally all the values calculated for the energy threshold at 90% trigger efficiency can be collected in the distribution of Figure (3.2.9). This distribution gives a quantitative idea of the overall goodness of the energy thresholds.

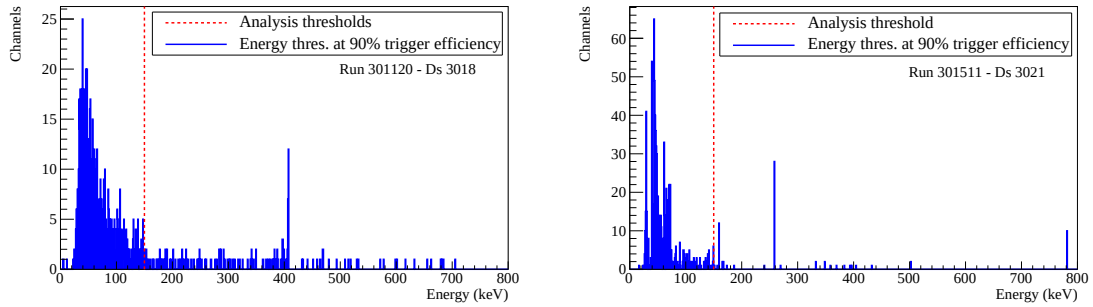

Figure 3.2.9: *Distribution all the energy thresholds at 90% trigger efficiency found in this check using the NPulsers run 301120 (left) of dataset 3018 and the NPulser run 301511 of dataset 3021 (right). Note that the channels without heaters are not present in this distribution since this method does not allow to know their energy threshold.*

Figure (3.2.9) (left) shows a spike around 400 keV and Figure (3.2.9) (right) shows few spikes for example at energies around 260 keV and 800 keV. These spikes are an artefact caused by the finite number of pulser amplitudes chosen for the NPulser runs. This problem is emphasised at high energies because there are only 3 amplitudes (3 points) that cover the region between 100 keV and 1000 keV. In that region, every time that the real energy threshold is positioned between the fourth and fifth point, or between the sixth and the seventh point and the efficiency of the previous points is zero, the fit and then the algorithm

to find the 90% trigger efficiency finds always the same value. To explain this concept we attach in Figure (3.2.10) and Figure (3.2.11) two efficiency curves of channels from the spike at 260 keV and the spikes at 800 keV from Figure (3.2.9) (right). In conclusion, for noisy channels having high energy thresholds, the NPulser runs aquired so far are not sensitive enough to appreciate the correct value of the energy thresholds, but can only find an upper limit.

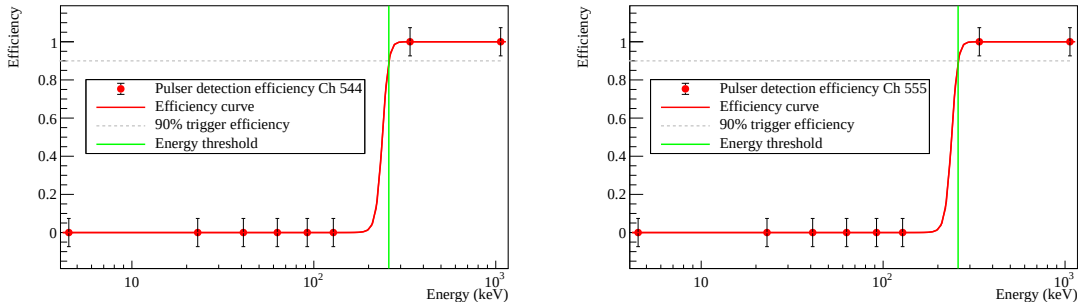

Figure 3.2.10: *Example of trigger efficiency curve (red line) and threshold (green line) for two channels (544 and 555) from run 301511, belonging to the peak at 260 keV in Figure (3.2.9). The energy thresholds of these three channels results exactly the same because there are only few points above 100 keV to fit the efficiency curve. The real thresholds could be anywhere between 120 keV and 300 keV.*

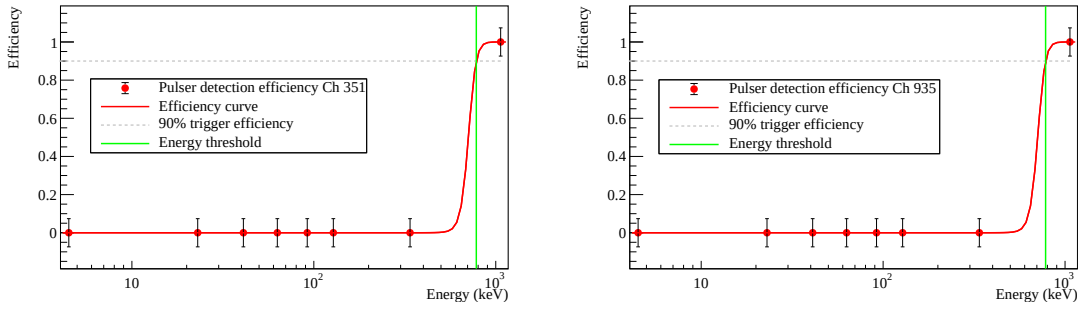

Figure 3.2.11: *Example of trigger efficiency curve (red line) and threshold (green line) for two channels (351 and 935) from run 301511 belonging to the peak at 800 keV in Figure (3.2.9). The energy thresholds of these two channels results exactly the same because there are only one points above 300 keV to fit the efficiency curve. The real thresholds could be anywhere between 300 keV and 1000 keV*

3.3 Pulse Tubes Noise Cancellation

The Pulse Tube cryorefrigerators are one of the main source of vibrations, which are transmitted to the detector through the cryostat. In Section (2.3.4) we saw how the movement of the PTs rotating valves induce a vibration on the cryostat at 1.4 Hz and its harmonics. The actual rotation frequency of the valves is not exactly 1.4 Hz but it has an error associated with it, thus the relative phases of the PTs slowly evolve with time. The superposition of these vibration frequencies emitted by the active PTs, combined with the complexity of cryostat suspension system, creates an interference pattern whose main components are modulated with periodicity as short as few tens of seconds, up to several hours. The PT induced noise is transmitted down to the detector and appears to influence the bolometers in different ways, depending from their position and their coupling with the rest of the cryogenic system. This noise is particularly dangerous because its typical frequencies are in the same range of the signal induced by particle interactions (from 1 to 10 Hz), hence it is not possible to filter it out with a low pass filter. Therefore, the PT noise could spoil the bolometers performances in term of energy resolution.
A series of countermeasures have been adopted in order to mechanically decouple the detector from the PTs. Nonetheless the rotating valves and the pressure waves generated by the compressed He that powers the PTs still remain a significant source of mechanical vibrations. In fact the Average Noise Power Spectrum (ANPS) of the detector channels still shows the presence of the typical PT induced noise frequencies.
In order to complete the detector optimization and to obtain better detector performances, the suppression of the residual amount of vibrational induced thermal noise is critical. This Section is indeed dedicated to the description of an active noise cancellation system [62] which exploits a low-noise microstepping motor to drive the PT rotating valves. We study the induced vibrations on the detectors in terms of relative phases between the active PTs to identify the configuration that allows to achieve the best coherent vibration addition in terms of noise suppression; then a LabView based program allows to control the microstepping motor and to lock the system on this phase configuration.
This noise cancellation technique, has been applied in its first rough version to the dataset 3018, acquired in May - June 2017 and in its final optimized version to the second dataset (3021) acquired in August 2017.

3.3.1 Linear Drive

To drive the rotating valves CUORE uses a microstepping power supply called Linear Drive (LD) instead than the more common motor embedded in Cryomech compressor

devices, which is not optimized for vibration reduction. The LD is a voltage generator with a linear amplifier for the output stage, designed as a motion control device for applications that need a low vibration environment. It provides the power to the rotating valves with an extremely high precision without sharp voltage changes, thus reducing the vibration produced by the glitchy rotative motion of the valves. The high precision is given by the number of steps in which the rotational motion is divided: in this case 25600 steps per period, giving a precision of 0.014°. In addition to the microstepping precision, the Linear Drives (LDs) allow also to change and control the working frequency of the rotating valves.
In CUORE the switch from the Cryomech motor to the LD microstepping motor happened only after the cool down because the LDs are not designed to operate on a warm cryostat. In fact in the first phase of the cool down, the power consumption is greater than usual due to the higher resistivity encountered by the rotating valves moving in the helium gas at high temperatures. Thanks to this delayed switch we were able to catch this moment and visualizing its effect on the detector. In Figure (3.3.1) is reported the output from the noise thermometer[6], positioned on the MC, during the switch to all 5[7] PTs driven by the LDs: in this plot is clear that the switch causes an immediate improvement in terms of base temperature stability.
Despite the visible reduction in amplitude of the temperature oscillations, driving the rotating valves by LDs still does not guarantee the working frequencies of different PTs to be exactly 1.4 Hz. The small residual working frequency differences between the PTs causes the relative phases of the pressure waves to slowly evolve in time, which induces variations in the noise induced on the bolometers signal, measurable from the NPS of the detector channels. In the rest of this Section we will exploit the control of the LDs to cancel out this residual effect and to minimize the noise on the bolometers.

Firstly, we must demonstrate that we can maintain this induced noise constant in time, which translates in being able to freeze the system to a given PT phase configuration, identified by a set of four phase differences between the five PTs. To ease the representation and the implementation of the sequent procedure, we choose a reference PT for the relative phases[8].
Gaining the complete control over the LDs needs however few steps done using software tools developed in LabVIEW programming language specifically for this purpose, within

[6] Magnetic Field Fluctuation Thermometer (MFFT-1) from Magnicon.
[7] During the first tests of the PT active noise cancellation method and during the first dataset (3018), we were using all 5 PTs, while later one was switched off and kept as spare.
[8] Up to the drafting of this Thesis we have always used PT number 5 as reference because it is used for the thermalization of the ^{3}He mixture at roughly 3 K.

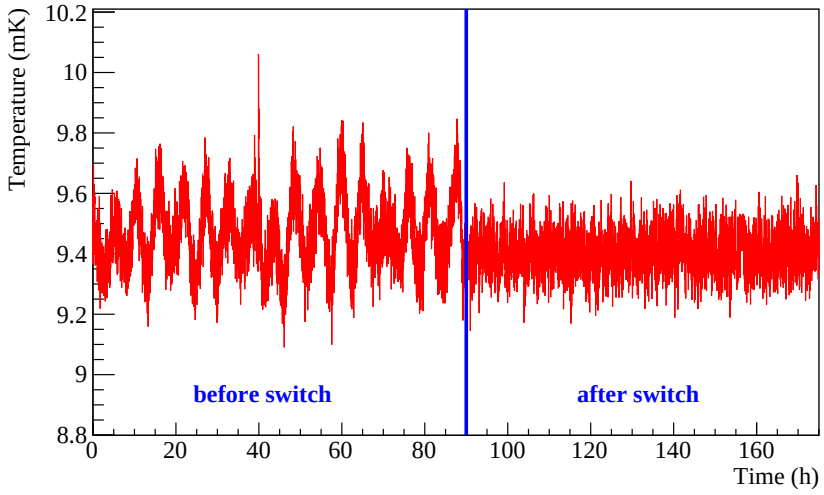

Figure 3.3.1: *Signal of the noise thermometer on the MC during the switch to the LDs. On the left of the vertical blue line none PTs were fed by LDs and the base temperature clearly shows beatings between the slightly different working frequencies of the 5 PTs fed by Cryomech motors. The beatings show periods of the order of* $\sim$ *6.8 hours and* $\sim$*40 hours. On the right of the blue line all 5 PTs are fed by the LD motors and the beatings are visibly strongly reduced in amplitude and period.*

the CUORE collaboration.

First of all we need to know the conversion factor between the number of steps and the actual phase shift from the reference PT, in degrees. This is done during a sort of "calibration" procedure, by acquiring the pressure inside the PT flexlines, equipped with pressure sensors[9], and calculating the phase difference between the pressure waves of all the PTs with respect to the reference one. At the same time a software does the same with the number of steps to then find the conversion factor between the number of steps and the phase difference. After the calibration we can comfortably forget about the number of steps and measure the phase shifts in degrees, thus we can drive the rotating valves directly in the phase-shift domain.

Secondly a phase control software tool was developed, which allows to move from one phase configuration to another. The algorithm applies a small correction (either acceleration or deceleration) to the working frequency of the rotating valves until the desired phase configuration is reached. The control transient takes from hundreds of milliseconds to several seconds because the frequency corrections never exceed 80 mHz, hence the PT working frequency always remains between 1.32 Hz and 1.48 Hz.

[9]The sampling rate of the pressure sensor is maximum 2 kHz.

In order to guarantee that the phase configuration does not evolve in time as it was doing before, we adopt a PT phase stabilization tool, that acts as a feedback system. This tool applies a series of little corrections to align the working frequency of the selected PT to the frequency of the reference one, then reads the so obtained phase configuration and applies a new frequency correction if the phase shifts are still out of the predefined range, and so on. In this way we can keep the same phase configuration within a certain precision, for the entire duration of the data taking. In order not to spoil the stability and the low noise environment, the corrections on the rotating valve velocity never exceed 20 mHz, so that the phase changes are as smooth as possible.

The effectiveness of the switch to the LDs first and the phase stabilization after, can be verified by analysing the data from the noise thermometer on the MC, in part using the same data from Figure (3.3.1). From the signal before and after the switch to the LDs, as well as from data acquired with the phase stabilization in operation, we can get the correspondent Power Spectrum (PS) whose shape and integral indicate the huge improvements in temperature stability that we obtained with these two countermeasures. These PS are depicted in Figure (3.3.2) where in blue and red are reported respectively the data from before and after the switch to the LDs and in green are the data with both LDs and phase stabilization in operation.

From the integral of the average PS of the temperature fluctuations of the MC, we can infer that LDs usage not only attenuates the amplitudes of the dominant frequencies, but reduces also the overall RMS from 0.118 mK to 0.092 mK. However the LDs introduce some higher frequency oscillations in the cryostat and we need to use the stabilization tool in order to get rid them. Unfortunately we do not have data acquired at 9 mK with the stabilization tool in operation to compare with the previous cases, therefore we will use the average PS of the noise thermometer on the MC at 11 mK (green PS in Figure (3.3.2)). We can see that when the stabilization tool is active, all residual beating peaks are suppressed and the RMS decrease from 0.092 mK at 9.4 mK to 0.074 mK at 11 mK. Since the noise thermometer RMS scales as the root square of the temperature and the RMS of the overall temperature measurement scales the temperature itself, we can estimate the equivalent RMS that the signal would have with the stabilization at 9.4 mK: it result being around 0.067 mK, giving an improvement in the noise of about 27% (we refer to reference [62] for the explicit extrapolation of the temperature RMS from 11 mK to 9.4 mK).

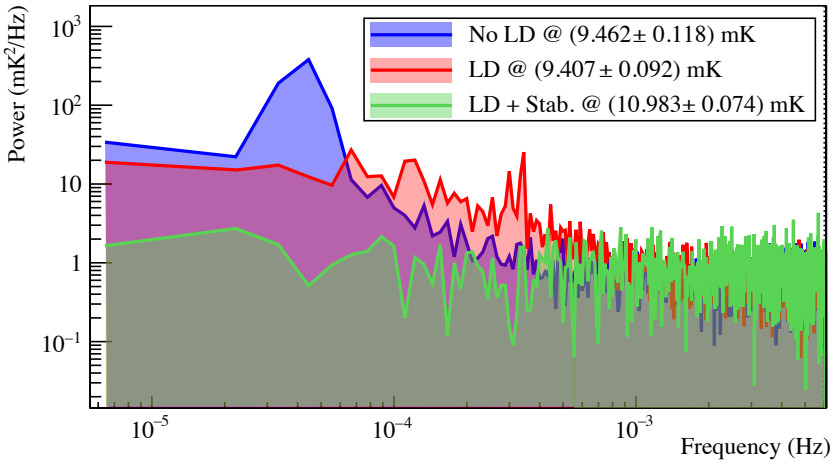

Figure 3.3.2: *Comparison of the average PS of the signal from the noise thermometer positioned on the MC. In blue are the data acquired at about 9.4 mK before the switch to the LDs; in red the data acquired also at about 9.4 mK after the switch to the LDs; in green are the data acquired at about 11 mK with the phase stabilization in operation. The noise has been computed averaging several 25-hours windows. This allows to recognize the main peak in the blue spectrum at ∼45 μHz due to the 6.2 h oscillations.*

3.3.2 Feasibility Study

Up to now I presented the technique used to control the LDs and the outcome of the stabilization on noise thermometer, thus on the temperature oscillations measured on the MC. At this point we wonder what happens to the bolometers signal, before and after the stabilization, and how far we can go with this active noise cancellation technique. In the very first period of data taking, during the development of the LabVIEW program designed to interface with the LDs and to handle the PTs rotating valves phases, a feasibility study was performed to demonstrate that the PT induced noise was indeed possible to isolate. Furthermore this study pointed out that, by controlling the microstepping motor, we were capable not only to stabilize the relative phases, but also to choose a phase configuration in which superposition of the vibrations from the different PTs would completely cancel out their characteristic noise (1.4 Hz and its harmonics), or at least strongly reduce it.

The test runs acquired for this feasibility study are noise runs similar to the ones used in Section (3.2): runs with an high frequency of noise trigger[10]. The runs have been analyzed

[10]For this analysis to each trigger is associated a 5 s long event window, instead of the standard 10 s one used for background data taking.

selecting only noise triggers and eliminating events with coincidence pulses in it or on the tail of pulses in order not to introduce signal-like frequencies in the NPS.

Then for each noise event we compute the NPS and get its amplitude at different frequencies (1.4 Hz, 2.8 Hz and the following harmonics up to 8.4 Hz). An example of NPS for an event is reported in Figure (3.3.3) in both logarithmic (left) and linear scale (right) where we indicate the peaks of the PT-induced frequencies that are visible for this channel at the time of the event.

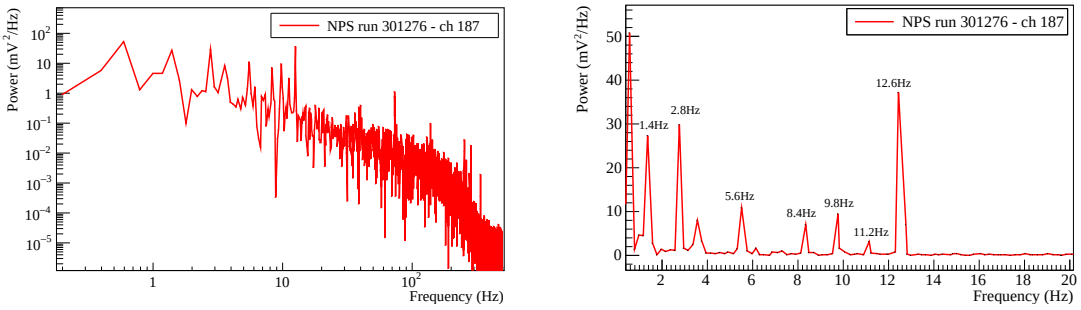

Figure 3.3.3: *NPS of an event from run 301276 - ch 187. Left: the NPS is reported in a broad range in logarithmic scale. Right: the same NPS is reported in linear scale, zooming on the low frequencies; the peaks of the frequencies induced by the PTs are indicated by the corresponding value in Hz. Since they vary with time, not all the frequencies are visible here and they do not have always the same amplitude.*

Later in the analysis chain we plot the frequencies amplitudes as a function of the time of the corresponding events, monitoring their trend in time. Examples of such plots is shown in Figure (3.3.4). At first we acquire data while letting the phases of the PTs, driven by the LDs, free to vary. An example of what happen to the selected frequency components of the noise signal is shown in Figure (3.3.4) (left): the intensity of each frequency component is modulated creating a periodic pattern. The cyan graph indicate the sum of all the selected frequencies amplitudes and highlights that within the modulated pattern there are phase configurations that induce a very high noise on the detector, but at the same time there are configurations in which all the noise components are at their minimum, indicating that the noise components induced by the active PTs cancel each other out. This is exactly what we want to obtain from this study: identifying a phase configuration that minimize the noise and keep it constant throughout the data taking. In the 14 h of data taking reported in Figure (3.3.4) (left) we can for example identify a minimum after about 4 h from the beginning of the run.

Figure (3.3.4) (right) depicts the trend in time of the amplitudes from the same frequencies

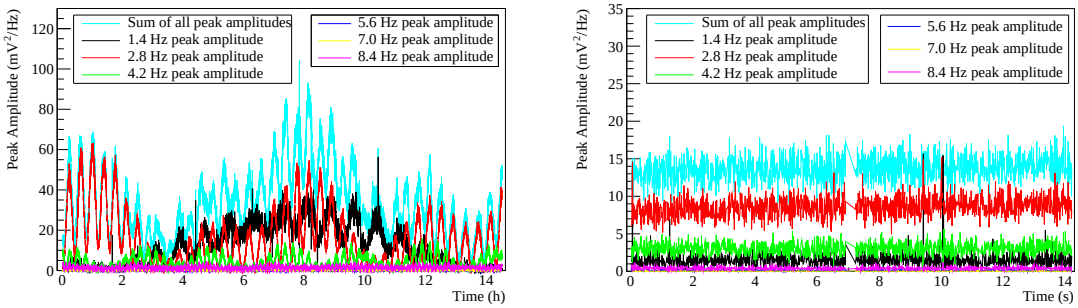

Figure 3.3.4: *Evolution in time of the NPS amplitude at 1.4 Hz peak and at its harmonics. Left: channel 187 of run 300697 where the PTs phases are left free to vary. Note that the spikes are probably due to small pulses int he noise events that have not been identified from the derivative trigger nor from the offline pulses identification algorithm. Right: channel 187 of run 300727 where the phase stabilization tool is operational and it maintains the amplitude of each peak constant in time. Note that the gap at about 7h is due to the interruption of one run and the start of a new run.*

and same channel of the plot on the left, but this time the phase stabilization tool is active, keeping the channel in a configuration close to the minimum. This time we observe almost no variation in time of the noise due to these frequencies. The first dataset acquired by CUORE (dataset 3018) was indeed only stabilized to a phase configuration that was on average good for data taking.

Nevertheless this is not enough for a good noise minimization. In fact the PTs induced noise has a different effect on every bolometer and thus we cannot assume that the optimal configuration for one channel is valid also for the others. This is demonstrated in Figure (3.3.5) where we compare the sum of the amplitudes of all the selected frequencies of two channels. Despite the fact that the two bolometers are physically close in the detector (they belong to the same tower and same column), the configuration of minimum noise does not overlap.

This task becomes therefore more arduous: not only we must sample all possible phase configuration for the active PTs but we have also to find the best configuration that minimize the average noise on all the channels, thus indirectly the configuration that optimize the sensitivity. In addition, if we want to explore all phase configurations for all channels, leaving the phases free to vary it would take something of the order of few years! To accomplish this task we conceived instead a phase scan that forces the PTs in all the possible configurations while taking data. Then offline we find the configuration that minimizes the noise induced from the PTs to the detector.

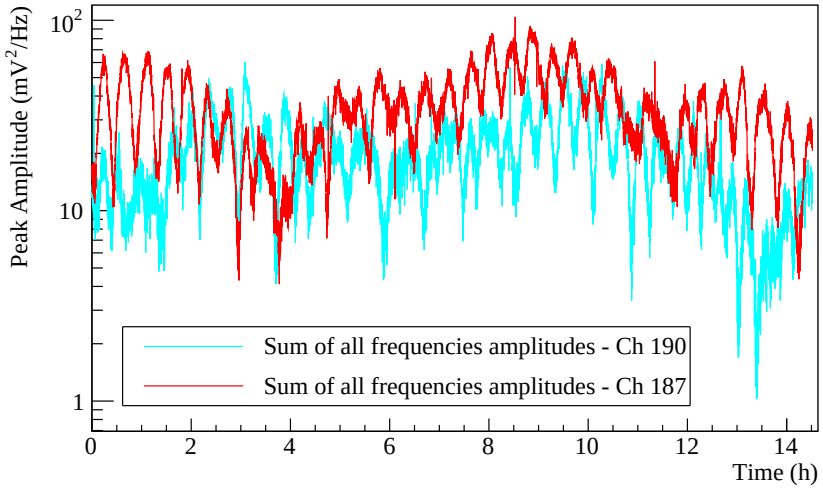

Figure 3.3.5: *Evolution in time of the sum of all selected NPS amplitudes for two different channels of the same noise run (channels 187 and 190). Note that the minimum is located in different moments for the two channels even though the bolometers are physically placed very close in the detector: channel 187 has a minimum in the configuration that is about 4 h after the beginning of the run, while channel 190 has the minimum about 13.5 h after the beginning of the same run.*

3.3.3 Phase scan

Via the calibration, control and stabilization tools that handle the LDs we can assume any phase configuration and keep it as long as we need. We can therefore use these tools to study different phase configurations searching for the best one.

The algorithm developed for the phase scan sets one configuration at the time and communicates to the DAQ the configuration change so that the DAQ can write into the data a *phaseID* that univocally identifies each set of phase differences. Ideally we would like to try all the possible configurations for the 5 PTs, but we must consider the time constrain that we had for the scan to comply with the data taking schedule. In fact the time needed to perform a complete phase scan depends on the number N of active PTs, from the time t spent in each configuration and from the scan step size S in degrees. We can write the time to complete the scan as a function of these parameters as follows:

$$T_{scan} = D \cdot t \cdot \underbrace{\left(\frac{360}{S}\right)^{(N-1)}}_{n_p} \tag{3.3.1}$$

where D is a coefficient representing the delay introduced by the algorithm dead times

which is about 1.1, n_p is the number of possible phase shift configurations. Each phase difference varies in the range [-180°, 180°[and is referred to PT5. The time t has to be long enough to acquire more than one noise trigger so that for each configuration we can average the NPS to remove random noise variations. Since the noise events last 5 s, for this scan we decided to take t=47 sec.

The maximum step size we can use to have a phase scan with good resolution is 20°. Assuming to have 5 PTs active the duration of the scan would be 57 days and this is not acceptable because this is only one of the many study performed on the CUORE signal and we must also take background data in steady operation mode for the $0\nu\beta\beta$ decay analysis. The only parameters on which we can act is the number of active PTs: since the CUORE cryostat has enough cooling power to work with only four active PTs out of five we decided to turn off PT 3 and work with N=4. This reduces the amount of time needed for the phase scan from 57 days to about 3.2 days.

The four active PTs are PT1, PT2, PT4 and PT5 giving three phase shift variables, namely x_1 ≡PT5-PT2, x_2 ≡PT5-PT1, x_3 ≡PT5-PT4. If each variable proceed in steps of 20° from -180° to +160°, the resulting possible phaseIDs are 18^3=5832, where 18=360°/20°. Each phaseID can be written following a base-18 positional notation:

$$phaseID = \sum_{i=1}^{3} \tilde{x_i} \cdot 18^{i-1} \tag{3.3.2}$$

where

$$\tilde{x_i} = \frac{180° + x_i}{20°} \quad i = 1, 2, 3 \tag{3.3.3}$$

For example, phaseID = 3038 corresponds to a set of phase configurations (100°, -60°, 0°).

We plot in Figure (3.3.6) the phase difference of the He gas pressure in the flex lines measured during part of the phase scan.

The tool developed for the phase scan change only one phase shift at the time, increasing the phase shift of 20° at the time and taking data for ∼47 s, while keeping all the other phase differences constant. Once all possible configurations are acquired, one of the two constant phase shift change and we explore again all possible configurations with the first phase shift and so on until we have acquired 47 s of noise events for each one of the 5832 phaseIDs. The scan is divided in multiple runs for an easier offline analysis. The noise triggers are simultaneously acquired on all the 988 CUORE bolometers every 5 s and we use event windows of 5 s each. In addition to the phaseID the DAQ assigns also a bad flags to noise events triggered during the transition time between different phase configurations.

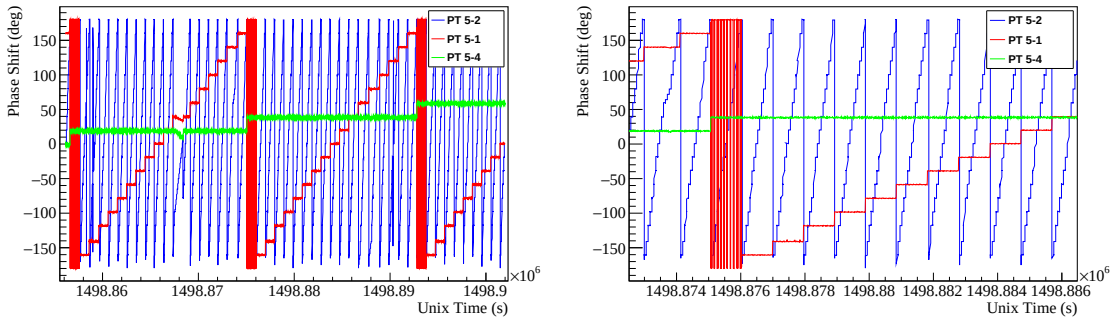

Figure 3.3.6: *Phase differences of the He gas pressure in the flex lines of the active PTs with respect to the reference one. From this plot and its zoom in (on the right) the various configurations (phaseID) of the PTs phase scan are visible. Each phaseID corresponds only to one change in the phase configuration.*

3.3.4 Analysis of the Phase Scan

In the feasibility study we left the phase differences free to vary, therefore we tested only few phase configurations. This time we have data for each one of the 5832 phaseIDs and hence we can perform systematic study on all the possible phase configurations. This analysis aims to find an optimal phase configuration that minimizes the noise on the whole detector. The first part of the analysis procedure is very similar to the one of the feasibility study but this time, instead that plotting the amplitude of the 1.4 Hz peak and its harmonics as a function of time, we plot it as a function of the phaseID. Moreover all the NPS of events belonging to the same phaseID, are averaged together in order to have a more reliable result on the ANPS amplitudes at the selected frequencies. In Figure (3.3.7), the 1.4 Hz noise is shown for one of the CUORE bolometers as a function of the phaseID. A similar behaviour can be observed for the first 10 harmonics of the 1.4 Hz peak and in each one we can identify numerous maxima and minima.

For each channel the 10 NPS amplitudes of all the events belonging to the same phaseID are corrected for the FE gain and weighted for their contribution in the PS of the channel AP[11]. In this way frequencies that are not present in the bolometers signal are suppressed in the noise minimization procedure while dominant frequencies in the signal spectrum see their importance enhanced (especially the two lowest harmonics 1.4 Hz and 2.8 Hz).

Finally, for each event we sum the 10 AP-weighted NPS amplitudes in order to get a unique value that quantifies the noise level for each event, which from now on we will indicate

[11] See Section (4.1) for more details on the average pulse.

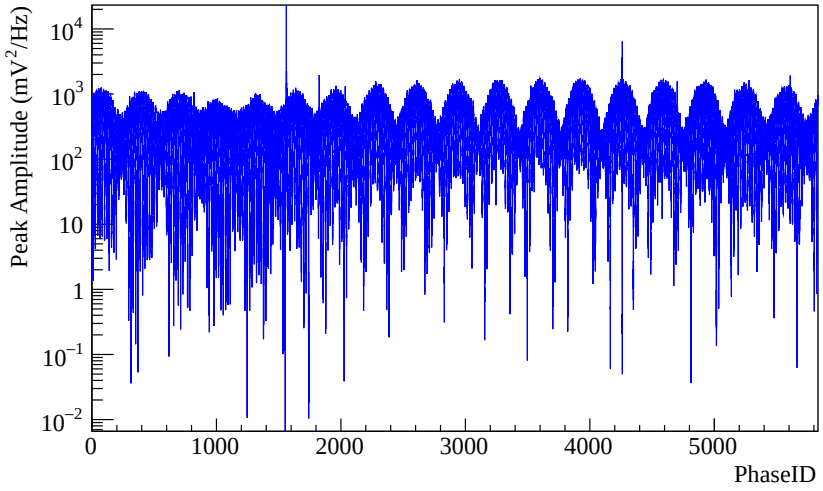

Figure 3.3.7: *Amplitude of the 1.4 Hz peak of the channel 65 ANPS, as a function of the phaseID.*

with the following notation:

$$\mathcal{A}^{(i)}_{ph,ch} = \frac{1}{G_{ch}} \sum_{n=1}^{10} AP_{ch}(f_n) \cdot \mathcal{A}^{(i)}_{ph,ch}(f_n) \ . \tag{3.3.4}$$

In Equation (3.3.4) *ch* is the CUORE bolometer channel that ranges from 1 to 988, *ph* is the PhaseID that ranges from 0 to 5831, i is the event number within the same phaseID (in fact within the 47 s of each phaseID there are usually from 1 to 9 events with a valid DAQ flag). G_{ch} is the gain characteristic of each event, $AP_{ch}(f_n)$ is the weight from the average pulse for each selected frequency and f_n is the n-th frequency of the 10 1.4 Hz harmonics. In order to get a single figure of merit that quantify the noise level for each channel-phaseID pair, we compute the median of the AP-weighted sum of the amplitudes of each event for all the events:

$$\mathcal{A}_{ph,ch} = \text{median}\left(\mathcal{A}^{(i)}_{ph,ch}; i\right) \ . \tag{3.3.5}$$

We chose in Equation (3.3.5) to use the median to eliminate possible outliers due to earthquakes, undetected pulses or other accidental causes that could influence the NPS. We refer to $\mathcal{A}_{ph,ch}$ as unnormalised noise.

From the experience on the PT induced noise acquired up to now, we know that there is a big variety of effects that the same vibration has on different channels: there are channels that picks up very clearly the typical PT frequencies while there are others that show

almost no sign of such frequencies thanks to their position and/or coupling with the rest of the cryostat and electronics. Accordingly we define a variable that quantifies the impact of PT vibrations on each single channel by computing the median of the $\mathcal{A}_{ph,ch}$ distribution across all phaseIDs of the same channel:

$$\mathcal{A}_{ch} = \text{median}\left(\mathcal{A}_{ph,ch}; ph\right) \ . \tag{3.3.6}$$

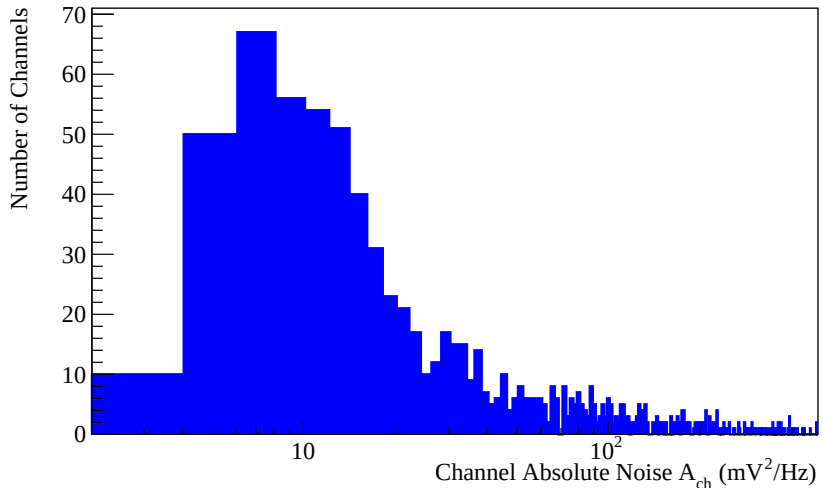

Figure 3.3.8: *Distribution of the total absolute noise $\mathcal{A}_{ch}$ for all the active channels of the CUORE detector. Note that most of the channels have low noise and there is only an handful of channels in the high noise tail of the distribution.*

The ensemble of these values, which we referred to as channel absolute noise, creates a set of typical channel noise values reported in Figure (3.3.8). We can observe that the absolute noise is not uniform among the channels, but that most of the channels exhibit luckily a very low noise level.

If the unnormalised noise is used to find the optimal configuration, the risk is to neglect those channels weakly susceptible to PT-induced noise, which are the majority, and to base the choice of the optimal phase configuration only on the few channels that pick up the PTs induced vibrations.

The solution to this problem is the creation of a normalized quantity that flattens the noise distributions among the channels, for which we use the notation $\widetilde{\mathcal{A}}_{ph,ch}$. This figure of merit is obtained by normalizing for each channel the noise level $\mathcal{A}_{ph,ch}$ in the range [0,1] without including the lower and upper 2% of the $\mathcal{A}_{ph,ch}$ distribution[12]. The normalized

[12]Phase configurations that are trimmed away would either exhibit a negative or greater than 1 $\widetilde{\mathcal{A}}_{ph,ch}$

noise $\widetilde{\mathcal{A}}_{ph,ch}$ allow to compare the characteristic noise of all channels on the same scale. Figure (3.3.9) (top) summarises how the detector noise state of each channel for each set of phase configurations: the color scale represents the normalized noise level of the channel-phaseID pair. It is clear that in Figure (3.3.9) (top) a pattern is present: there are vertical bands (in phaseID) of lower and higher noise levels for all the channels, as well as regions where it is not clear which phaseID minimize the noise on the full detector.
Figure (3.3.9) (bottom) shows the overall trend of the detector normalized noise as a function of the phaseID and it is obtain by doing the median across all channels of $\widetilde{\mathcal{A}}_{ph,ch}$.

$$\widetilde{\mathcal{A}}_{ph} = \text{median}\left(\widetilde{\mathcal{A}}_{ph,ch}; ch\right) \tag{3.3.7}$$

In other words is like projecting the plot of Figure (3.3.9) (top) on the abscissa. $\widetilde{\mathcal{A}}_{ph}$ represents the detector typical normalized noise to each particular phase configuration. The 2 bands that extend out of range are due to earthquakes and are excluded from the optimization procedure. The absolute minimum of this plot is the phase that minimize the noise on the full detector: looking at $\widetilde{\mathcal{A}}_{ph}$ we can already identify by eye two possible regions of low noise around a phaseID of 200 and around a phaseID of 5800.
We could use the absolute minimum of the plot in Figure (3.3.9) (bottom) to select the optimum phaseID, but means that we give equal importance to channels weakly and strongly affected by PT noise. Our priority is however the suppression of the noise in those channels that are strongly influenced by the PTs, secondly in all the others. Therefore we developed an iterative procedure designed to find the ideal phaseID for as many channels as possible, grouping the channels for their noise level.
The procedure starts from the absolute noise distribution $\mathcal{A}_{ch}$ defined earlier in this paragraph and repeated in Figure (3.3.10). For each iteration of the procedure we set a threshold q to the $\mathcal{A}_{ch}$ distribution and we remove all the channels below the threshold, keeping only the channels in the high noise side of the distribution:

$$ch \in \{\mathcal{A}_{ch} > q\} \ . \tag{3.3.8}$$

Note that the first iteration has $q = 0$, thus we include all the channels, then the value of q progressively increases reducing the number of channels. We build for the subset of selected channels a plot representing the normalized noise $\widetilde{\mathcal{A}}_{ph,ch}$ as in Figure (3.3.9) (top) and then collapse it on the abscissa by finding for each phaseID the median among all the channels that appear in this plot, as was done for Figure (3.3.9) (bottom). From the so obtain plot we select the phaseID that shows the minimum normalized noise. Then we

value.

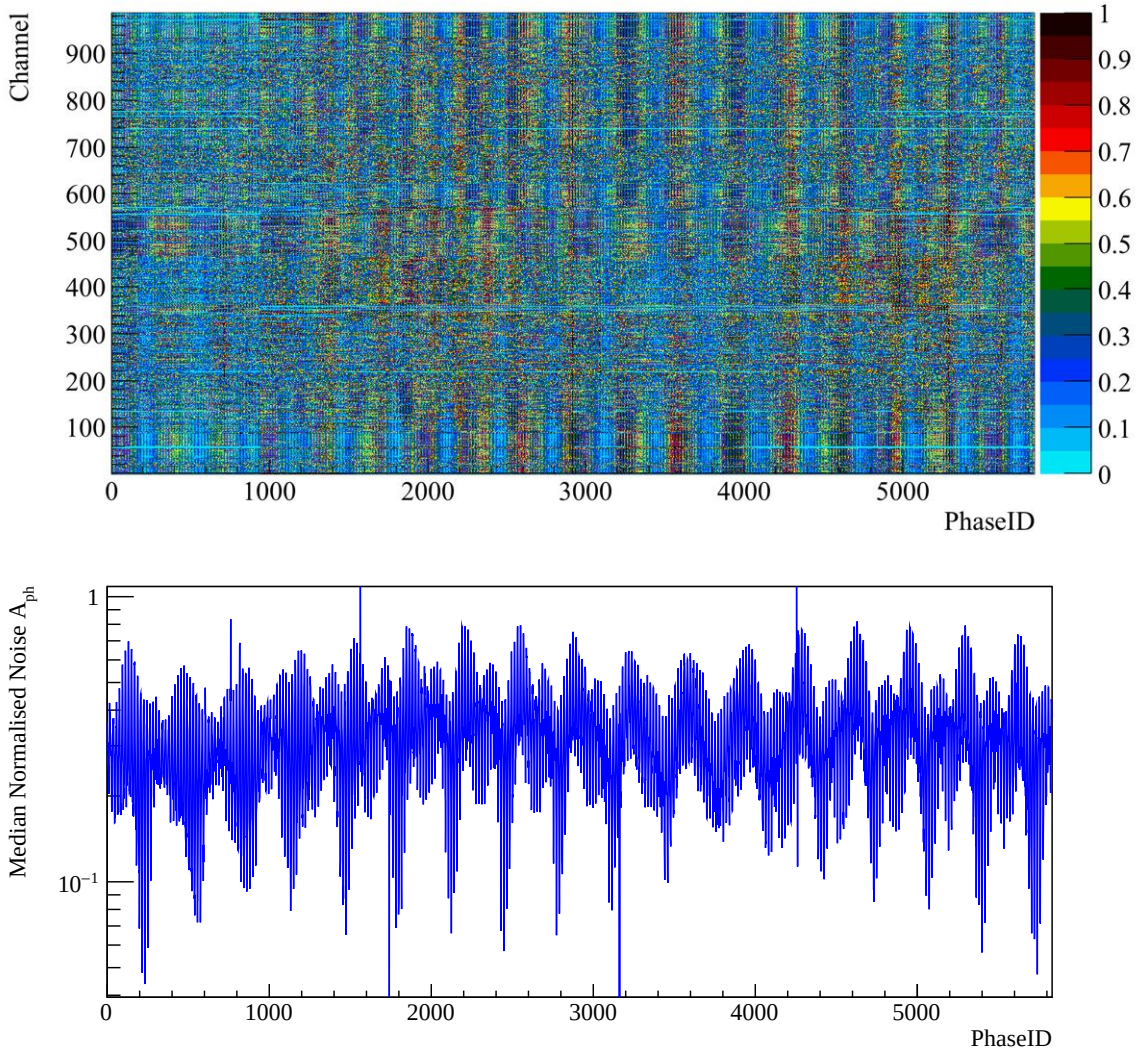

Figure 3.3.9: *Normalized total AP-weighted sum of the 1.4 Hz harmonics noise,* $\widetilde{\mathcal{A}}_{ph,ch}$. *Top: each bin uniquely identifies a channel-phaseID pair and its color indicates the normalized value of the noise. Bottom: median across all channels of* $\widetilde{\mathcal{A}}_{ph,ch}$ *to give an overall trend of the detector normalized noise as a function of the phaseID.*

begin the second iteration by moving the threshold q upwards, in order to include less channels, and so on, until we exclude all the channels.

The phaseIDs selected at each step of the iteration is shown with two different representations in Figure (3.3.11): when there are only few low-noise channels the preferred phaseID is around 5000, but as soon as the number of channels increases the favoured phaseID stabilises first on phaseID 216 and then on phaseID 233, when the number of channels

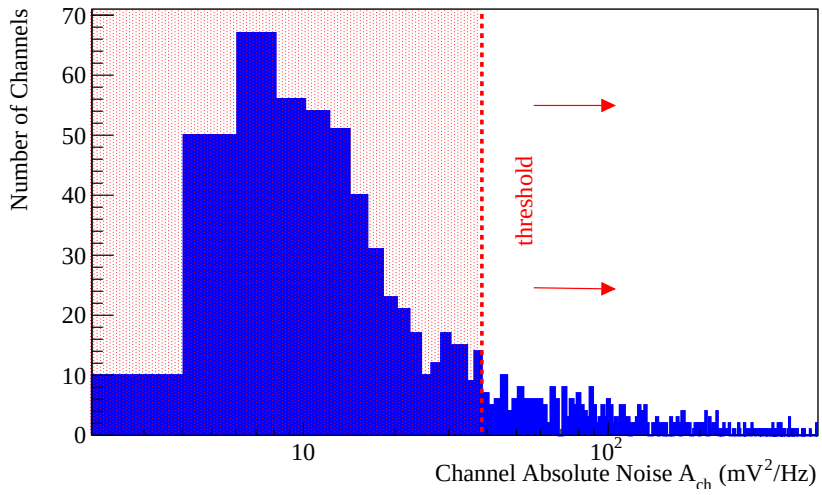

Figure 3.3.10: *Distribution of the total absolute noise $\mathcal{A}_{ch}$ for all the active channels of the CUORE detector. During the optimization process, only the channels above threshold (vertical red line).*

included overpass 457.

From Figure (3.3.11) we can infer that there are two phaseID that satisfy the condition of minimum PTs induced vibrations for the majority of the channels, namely phaseID 216 and phaseID 233. These correspond to the phase configuration reported in Table (3.3.1).

PhaseID	phase shift [deg]		
	$PT^{(2)}$-$PT^{(5)}$	$PT^{(1)}$-$PT^{(5)}$	$PT^{(4)}$-$PT^{(5)}$
216	-180°	+60°	-180°
233	+160°	+60°	-180°

Table 3.3.1: Optimal PT phase configurations.

At last, only with the purpose of satisfying our curiosity, we can compare the distributions of the number of channels as a function of the absolute noise for the two optimal phaseIDs with the distributions of all the other phaseIDs. This is illustrated in Figure (3.3.12): the color scale of the 2D distribution represents the phaseID density while the red and black histograms are the distributions of phaseID 216 and 233 respectively. As you can see from this figure, the two selected phase configurations are those that maximize the number of channels having the minimum absolute noise.

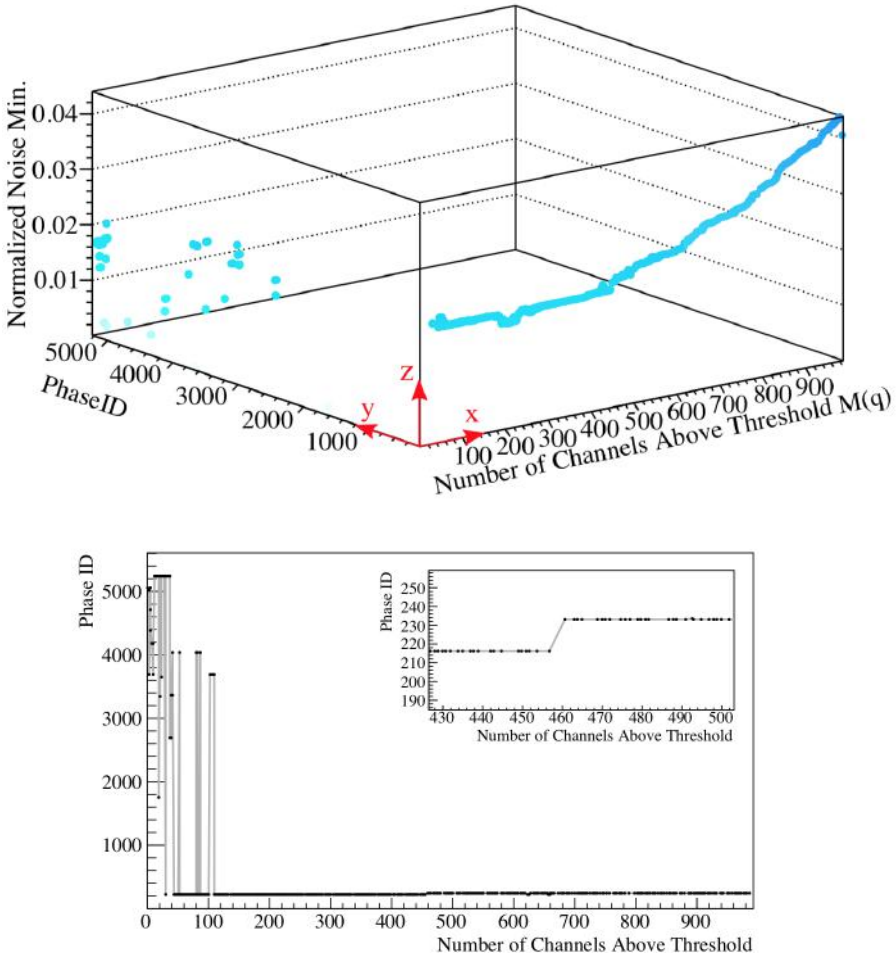

Figure 3.3.11: *Optimal PhaseID identification. Each selected threshold q in the iterative process of the phase optimization corresponds to a point in the two plots and identifies a subset of channels above threshold (x-axis) whose minimum normalized noise (z-axis) occurs at a particular phase configuration (y-axis). Top: the colors of the z-axis minimum normalized noise values respect the same color scale used in Figure (3.3.9). Bottom: same of the top plot projected onto the x-y plane.*

In conclusion in this section I presented the technique that CUORE uses to actively cancel out the vibrational noise introduced by the four active PT cryocoolers. The data in the second dataset (3021) has been acquired using the stabilization tool on phaseID 233 and the outcome will be evident in the next chapter where I will describe the analysis procedure for the $0\nu\beta\beta$ decay analysis.

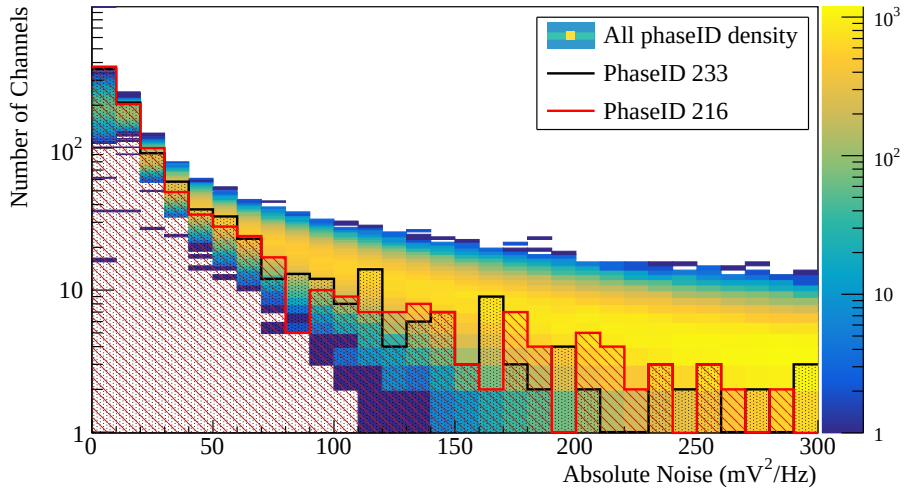

Figure 3.3.12: *This figure shows a density histogram of the median noise across all channels for each individual phase configuration binned by the typical AP-weighted noise value. The colored z-axis shows the number of PhaseID histograms per pixels. We see that a majority of phase configurations do have a few hundred channels with low noise but that there is a long tail typically to the fall off of noise. In contrast the two best performing PhaseIDs (233 in black and 216 in red) are at the top of the profile at the very lowest values and fall quickly to the lower edge of the profile as the noise bins increase in value. This is the response one might expect for configurations that minimize noise.*

Chapter 4

Analysis

This Chapter is dedicated to the analysis of the first two dataset acquired by CUORE. In Chapter (3) these two datasets have been introduced when talking about the detector optimization. Now we will use their data to extract a limit on the half life of ^{130}Te . The data presented here have been acquired at (15.0±0.1) mK.

The data taking started with dataset 3018 at the beginning of May with the opening calibration which lasted 5 days, from May 6^{th} to May 11^{th} 2017. After the opening calibration we took data in a stable mode for 24 days (until June 4^{th}). We called this period physics data taking. The dataset is closed by a second calibration which lasted 4 days, from June 6^{th} to June 10^{th}. This dataset was triggered initially with event windows of 5 s each but in the summer of 2017 it was proven that it was possible to improve the energy resolution with event windows of 10 s each, hence the continuous data from dataset 3018 was retriggered with 10 s windows. The rest of June and July 2017 have been dedicated to detector optimization and test runs to retrieve the data taking at the end of July with the dataset 3021. As usual the first few days have been devoted to the initial calibration (4 days from July 30^{th} to August 2^{nd}), followed by 27 days of background runs (from August 4^{th} to August 31^{st} 2017), and other 6 days of closing calibration. Given the previous experience, this second dataset was acquired directly saving event windows of 10 s. In addition to the longer event windows, the improved noise situation and the lower derivative trigger thresholds resulted in a better energy resolution and and higher number of channels that reached the final steps of the analysis.

In both datasets the active channels where 988, but during the analysis some of the channels had to be removed for several reasons: some of the channels where too noisy to trust their triggered events, others failed one or more than one of the analysis steps that will be described in this Chapters, some others did not have enough events in the energy

calibration spectrum in order to get a proper energy calibration detector response and so on. Removing these problematic channels, the analysis was performed on 876 channels for dataset 3018 and on 935 channels for dataset 3021. Accordingly the contribution from these channels was also removed from the exposure computation yielding an exposure of TeO_2 of 37.6 kg·yr for dataset 3018 and of 48.7 kg·yr for dataset 3021, obtaining a total exposure of 86.3 kg·yr, more than twice the exposure of CUORE-0.

4.1 Data Production

In this section we will face all the steps needed to go from triggered data to the final set of NTuples used for the high level analysis, $0\nu\beta\beta$ search in our case, but also other rare events searches such as excited states, axions, dark matter and so on. This section is divided in two parts: first of all we will describe how to get from the QRaw data to the CUORE energy spectrum in both background and calibration data, namely the low level data processing; then I will give an overview of the techniques used in CUORE to find those events that are not in coincidence with others and that have the expected pulse shape, also called high level data processing.

4.1.1 Low level processing: from raw data to energy

QRaw data files are the product of the `Apollo` triggering algorithm[1]. They contain signal, noise and heater triggers of both bolometers and thermometers. From now on we will we use only bolometer signals and we will refer to the bolometers as *channels*.
Before starting to process the data the shifter inspects the channels baselines with an interactive monitoring tool and selects periods of time in which the baseline was unstable or very noisy (for example because of an earthquake). By the end of dataset 3021 an automated tool was developed to perform the same task, but selecting the Bad Interval more efficiently than the visual inspection that was used before. Therefore at the end hence at the end the tool was run on both dataset For each channel these periods of time, called Bad Intervals, are inserted in the database and eliminated from the data analysis. The exposure is computed taking the Bad Intervals under consideration so that it actually reflects the effective active time of the bolometers. Note that removing the Bad Intervals only reduces the exposure by 1%.
QRaw data are processed with a modular program called `Diana` which loops over each event and execute the module task that can be from computing quantities to filtering events.

[1]The data acquisition software is described in Section (2.4.2) and the derivative trigger algorithm is described in Section (3.2).

It possible to group different modules in what we call *sequence*. Each sequence can contain different modules and filters, but it must have a reader that load the data (either QRaw or the output of a previous sequence) and a writer that writes to file and eventually merges the output of the current sequence into previous data production files.
The low level processing takes care of transforming the QRaw triggers in a usable NTuple for data analysis, computing a set of parameters for each event, stabilising the thermal gain of each event and calibrating the spectrum with some known spectral lines.

Preprocessing

The first `Diana` sequence is the *Preprocess*. Few important variables that will be used throughout the entire data processing are evaluated here: baseline parameters and the number of pulses.
The baseline parameters are evaluated for each event in the first 3/4 of the pre-trigger, in our case precisely 2.25 sec of the event window. The baseline is a proxy for the detector condition right before the particle interaction in the detector. The most used baseline parameters are *baseline*, *baseline slope* and *baseline RMS*. The first one gives the output voltage (in mV) of the NTD and it is proportional to the operating temperature of the bolometer if the offset remains constant. The baseline slope and baseline RMS are computed by fitting the samples of the pre-trigger with a linear regression: the former is given by the angular coefficient of the linear regression and the latter is the RMS of the residual of each sample about this line.
An other important parameter the is computed in this sequence is the number of pulses. This does not correspond to the number of trigger in the event window and it is evaluated with a different algorithm with respect to the trigger procedure. In fact here we differentiate the signal of the selected event and a pulse is counted whenever the derivative exceed a threshold in unit of the derivative RMS.

Amplitude and Signal Filtering

We refer to *Amplitude* as the height of the pulse corresponding to the event trigger. However the Amplitude is not evaluated on the signal as it is, but after filtering the waveform from unwanted frequencies using the Optimum Filter (OF).
The OF evaluates the amplitude of a pulse maximizing the SNR. We assume that a detector waveform $y(t)$ can be written as:

$$y(t) = A \cdot s(t) + n(t) \tag{4.1.1}$$

where $s(t)$ is the known signal time evolution, A the signal amplitude and $n(t)$ the detector noise. Both the detector response $s(t)$ and the detector noise $n(t)$ are presumed to be stationary during the dataset. Given that the OF works on sampled data, Equation (4.1.1) becomes:

$$y_i = A \cdot s_i + n_i \tag{4.1.2}$$

We want to attenuate as much as possible the noise component of Equation (4.1.2). The transfer function that we use to filter the data is, for a given frequency ω, directly proportional to the SNR [63]:

$$H(\omega_k) = h\frac{s^*(\omega_k)}{N(\omega_k)}e^{j\omega_k i_{max}} \tag{4.1.3}$$

where $s(\omega_k)$ is the Discrete Furier Transform (DFT) of the ideal signal s_i, i_{max} is the position of the maximum of s_i, $N(\omega_k)$ is the ideal detector noise power spectrum and h is a normalization constant required to leave the signal amplitude unchanged

$$h = 1/\frac{\sum_k |s(\omega_k)|^2}{N(\omega_k)} \tag{4.1.4}$$

Building this transfer function required the prior knowledge of the detector response and the detector noise for each channel in each dataset.
We construct the detector response using events of the ^{208}Tl line in calibration data acquired at the beginning and at the end of each dataset. The selected signal pulses are normalised and averaged together so that the noise present in the waveforms cancels out. In CUORE-0 it was a standard procedure to align the maximum of the pulses before averaging them, but in CUORE we decided not to do so because for channels with elevated level of high frequency noise the alignment was happening not at the maximum of the pulse, but at the maximum amplitude of the noise frequency. The alignment procedure was causing the coherent sum of some noise components in the average pulse, spoiling the performance of the OF. The detector response just described takes the name of AP.
The detector noise is called ANPS. It is built from random noise events, selecting those events that show a small baseline slope, to make sure that the selected events is not taken from the tail of a pulse (this will introduce signal-like frequencies in the ANPS). The selected noise events are transformed in the frequency domain with the FFT and then averaged together. Figure (4.1.1) shows an example of AP and ANPS before and after the filtering process with the OF.
Once the waveform of the current event is filtered, `Diana` evaluates the amplitude in two

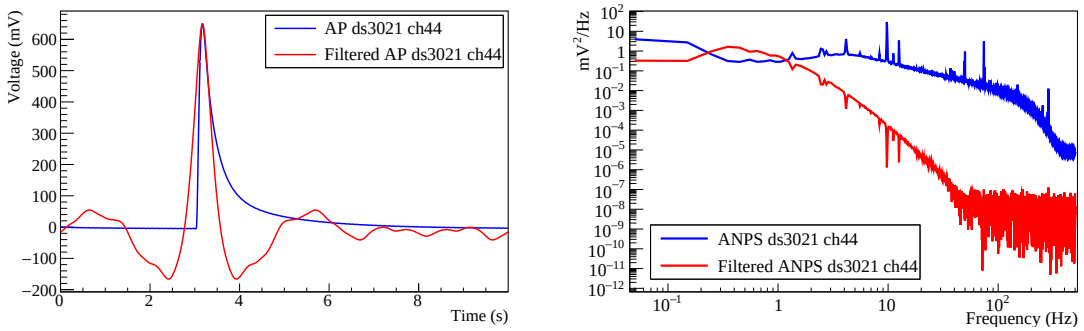

Figure 4.1.1: *Left: Average Pulse (AP) - Right: Average Noise Power Spectrum (ANPS). Both figures show in blue the original waveform and filtered in red, of channel 6 in dataset 2088. As can be seen the in red the filtered one. The filtered AP shows a quasi-symmetric shape and a zero baseline (the original pulse is moved to have zero baseline for an easier comparison with the filtered one). The acquisition windows are 10000 samples long, corresponding to 10 sec.*

steps: it finds the peak and interpolates the samples close to the maximum with a parabola to find the real maximum of the pulse as the position of the maximum of the fitted parabola.

Stabilization

Our data now has the Amplitude variable but, does this amplitude correspond to an energy? Not yet. In fact the thermal gain of the bolometer depends on the operating temperature of the detector and a small variation in temperature could change the measured amplitude during data taking. CUORE adopt a thermal gain stabilization technique to address this problem. This technique is implemented in two different ways, conceptually very similar, but technically different: the heater thermal gain stabilization (heater-TGS) and the without heater thermal gain stabilization (calibration-TGS).

The heater-TGS exploit the constant energy heater pulses events, studying the trend of their amplitude with respect to the baseline. The baseline value is a proxy for the temperature, while the amplitude of the pulser, varies with the operating temperature. `Diana` stabilization algorithm derives a gain function by a linear regression on the amplitude versus baseline distribution of heater events, produced by releasing always the same energy in the bolometers. The energy of the heaters events is in general slightly above the 2615 keV ^{208}Tl line, usually around 3000 keV. In this procedure we are assuming that the gain dependence is linear in the small range in which the temperature is varying. The gain function is evaluated independently for each channel-run and the coefficients are stored and used later to correct the amplitude. The amplitude A found in the previous section is therefore

corrected for the gain instabilities and remapped to an arbitrary value of 5000 a.u.:

$$A_S = 5000 \cdot \frac{A}{GainFunc(baseline)} \tag{4.1.5}$$

The corrected amplitude variable A_S takes the name of *stabilized amplitude*. An example of the heater events before and after the pulser gain stabilization is reported in Figure (4.1.2).

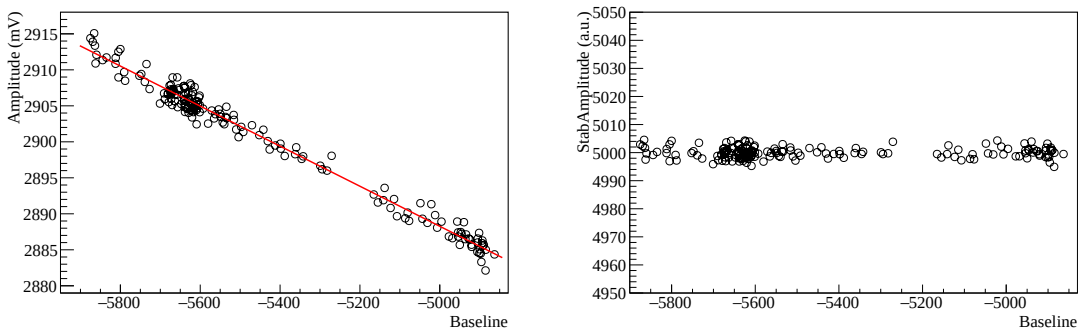

Figure 4.1.2: *Heater events of Channel 850, Tower 17 in Run 301484 of Dataset 3021. Left: the amplitude versus baseline distribution shows a linear decreasing trend, fitted to find the gain function. Right: the same data of the left plot, after the amplitude has been corrected.*

The calibration-TGS is similar the standard stabilization, but this time instead of using the pulser heater events to trace the temperature gain dependence, we use the events from 2615 keV ^{208}Tl line from calibration runs. For each channel the amplitude versus baseline is fitted with a quadratic function to account for non linearities in the gain temperature dependence. This algorithm allows to create coefficients valid for the entire dataset, but it requires a careful accounting for voltage offset and gain, measured during the Working Points runs, in order to determine the absolute baseline voltage. The amplitude is corrected with the same equation used for the pulser thermal gain stabilization, but this time the pulses have known energy and are therefore remapped to 2615. The corrected amplitude variable takes the name of *stabilized amplitudes without heater*.
In summary, at this point we have in our data (both background and calibration) a stabilized amplitude without heater variable for every channel and a stabilized amplitude variable for all channels with a working heater.

Calibration

The stabilized amplitude is transformed to energy by mean of the calibration sequence.

The first and last few days of a dataset are devoted to energy calibration with ^{232}Th γ-ray sources. During the calibration data taking 12 Kevlar strings, populated with beads made of low-intensity ^{232}Th sources, are lowered into the detector volume so that all towers get a uniform illumination. See the DCS paper [55] for more details. We use six γ lines from the ^{232}Th calibration sources to estimate the mean stabilized amplitude of each line and create a map from stabilized amplitude to physical energy, namely a calibration function for each channel in each dataset. The six γ lines range from the 239 keV ^{212}Pb line to the 2615 keV^{208}Tl line, but not all of them are necessary for a successful calibration. In fact four of these peaks are called *primary* and the remaining are *secondary*. The calibration module first identifies the six peaks from the ^{232}Th calibration sources: starting from the closest peak to the heater pulser we have 2615 keV^{208}Tl line, 969 and 911 keV lines from ^{228}Ac, 583 keV line from ^{208}Tl , 511 keV electron-positron annihilation line and finally the 239 keV ^{212}Pb line. The identification of three out of four primary peaks is mandatory in order to get the calibration algorithm to work. If less than two peaks are located by the peak finding algorithm the sequence ask for human intervention and the user must manually select the peaks with a GUI. An example of a typical energy spectrum from a good channel is reported in Figure (4.1.3): in this case all the peaks are easily identified, but sometimes we get only few tens of events in each peak.

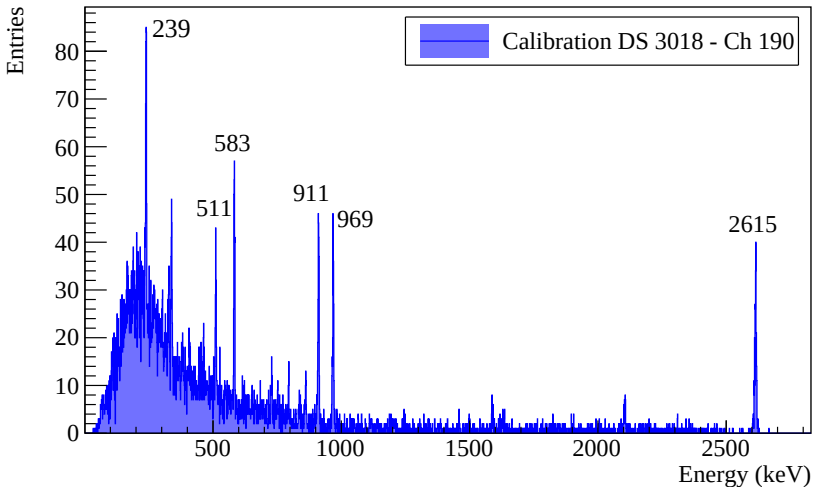

Figure 4.1.3: *Example of energy spectrum from the initial and final calibration of dataset 3018, channel 190.*

The second step of the calibration procedure is the lines fit. Each peak is fitted with a CrystalBall function plus a linear background and the best-fit value for the peak position

is found. The peak positions in unit of stabilized amplitude are then used to regress the calibration function. The calibration function that we used is a second order polynomial passing through the origin:

$$Energy = a \cdot A_S + b \cdot A_S^2 \tag{4.1.6}$$

where a and b are the calibration coefficients that for each channel are written to file and applied to the stabilized amplitude variable of the physics data to get the *Energy_ OF* variable. The exact same procedure is applied to the stabilized amplitude without heater, so that when the calibration procedure is over we end up with two energy variables that here we will call *Energy_ OF* for the standard one and *Energy_ WoH* for the energy that comes from the amplitude stabilized without heater.

4.1.2 High level processing: from energy to the final set of data

Blinding

After the calibration sequence we blind the data, for the following steps of data production and for the subsequent analysis, by introducing an artificial peak at $Q_{\beta\beta}$. The blinding algorithm is designed to mask any possible signal or statistical fluctuation in the Region of Interest (ROI) and at the same time to preserve the integrity of the spectrum that we use for testing all our later analysis steps. The blinding technique that we adopted is also called data salting technique. It consists in randomly shifting to $Q_{\beta\beta}$ the reconstructed energy of a fraction of events within 10 keV from the ^{208}Tl peak, by subtracting 87 keV. Simultaneously we shift the same fraction of events from within 10 keV around $Q_{\beta\beta}$ to the ^{208}Tl line, by adding 87 keV. This fraction can be as high as 40%. In fact, the intensity of the ^{208}Tl peak in physics data is very low, as shown in Figure (4.1.4), therefore we are forced to use such an high event fraction to ensure to have enough data to cover the ROI effectively. The visible effect of the salting procedure is a peak at $Q_{\beta\beta}$ as shown in Figure (4.1.4). The true energies of the events that have been shifted is encrypted and stored until unblinding.

Energy Variable Selection

We are now in the inconvenient situation of having two energy variables (Energy_OF and Energy_WoH), but it is necessary at this point of the data production to converge in having only one energy variable for each channel. For channels that do not have a functioning heater the choice is obligated and we must use Energy_WoH, but can we improve the overall energy resolution, therefore the sensitivity, by selecting one or the other energy

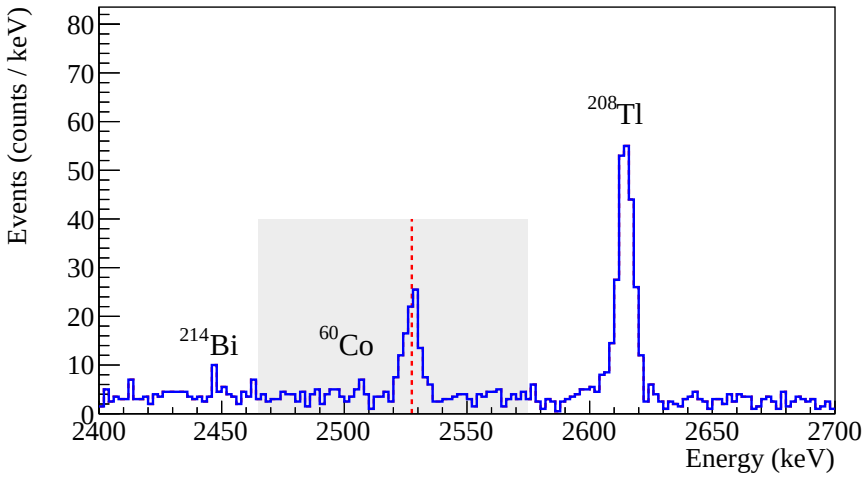

Figure 4.1.4: *Region of the blinded background spectrum that includes both the ROI and the ^{208}Tl line. The grey shaded line is the ROI and the red dotted line indicates the position of $Q_{\beta\beta}$. A fraction of events in the ^{208}Tl line have been shifted down by 87keV and vice-versa, resulting in a fake peak at $Q_{\beta\beta}$. Beside the ^{208}Tl line, also the ^{60}Co and the ^{214}Bi lines are visible.*

variable on the rest of the channels? The answer is yes and I will now explain how this choice is made.

For each channel-dataset we take all events that belong to the ^{208}Tl line that we compute the energy variance for both energy variables. We will call the variances σ_{OF} and σ_{WoH} for Energy_OF and Energy_WoH respectively. For each channel-dataset we then build a figure of merit W to quantify which one of the energy variable is better, by computing the ratio of the of the two energy resolutions, normalised by the exposure

$$W = \frac{\sigma^2_{WoH} \cdot \epsilon^2_{OF}}{\sigma^2_{OF} \cdot \epsilon^2_{WoH}} \tag{4.1.7}$$

where ϵ_{OF} is the exposure of the channel using the Energy_OF variable and ϵ_{WoH} is the exposure using the Energy_WoH variable. Finally we define a condition for choosing one energy estimator over the other, that we define in with the following expression:

$$W < 1 \quad \wedge \quad Z = \frac{(1-W)}{\sigma_W} > 1 \tag{4.1.8}$$

where σ_W is the uncertainty over W given by error propagation.

Figure (4.1.5) shows the distributions of Z as a function of W for both datasets. Only the channels highlighted in the circles show a clear improvement in energy resolution with

the use of Energy_WoH, all the other channels will default to Energy_OF. From now on there will be only one official energy variable, called *Energy*.

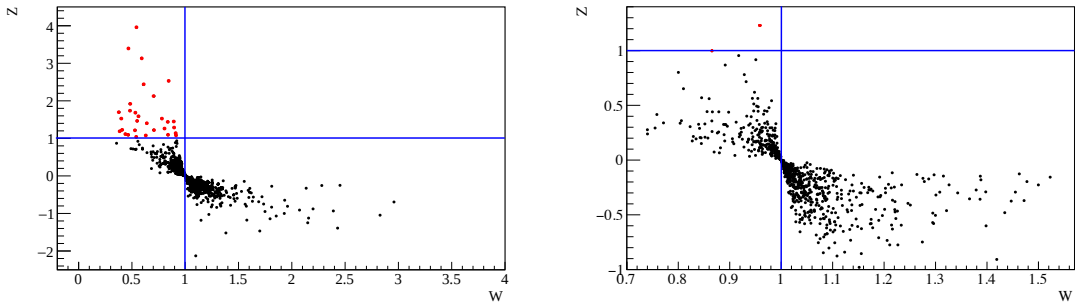

Figure 4.1.5: *Energy variable selection criteria. In this ZW space, are marked in red the channels for which the selected energy is Energy_ WoH; all the other channels default to Energy_ OF. Left: energy variable selection for DS3018. Right: energy variable selection for DS3021.*

Coincidences

We expect that a $0\nu\beta\beta$ decay is contained in a single bolometer with 88.35±0.09% efficiency[2]. This means that, in first approximation, we do not expect this rare decay signal to fire more than one crystal at the time. This allow us to reject physical events that cause two or more signal at the same time, such as multiple scattering from γ rays or surface α depositing energy in two neighbour crystals. Therefore we search for coincidences between different channels and we reject events with a multiplicity greater than one. For multiplicity we intend the number of channels whose trigger fires within a narrow time window, and whose event pulses are above a fixed energy threshold. The energy variable used for this sequence is the one selected by the Energy Variable Selection procedure and thus it can be Energy or Energy_WoH depending on the channel-dataset considered. In this analysis we chose an energy threshold of 150 keV, because it is above the energy trigger threshold of most of the channels, but this value can be lowered in future analysis, for example when we will be able to lower the trigger thresholds by mean of the Optimum Trigger (OT) [63, 64]. It is worth mentioning that no geometric cut is imposed in this analysis, hence any coincident event, even if on the opposite side of the detector, is rejected. In future analysis we foresee the implementation of a geometric cut so that the coincidences can be computed on a subset of close packed channels, in order to increase the efficiency of

[2]The $0\nu\beta\beta$ containment efficiency is obtained by the CUORE Monte Carlo.

anti-coincidence cuts and minimise the rejection of separate physical events happening at the same time in different regions of the detector.

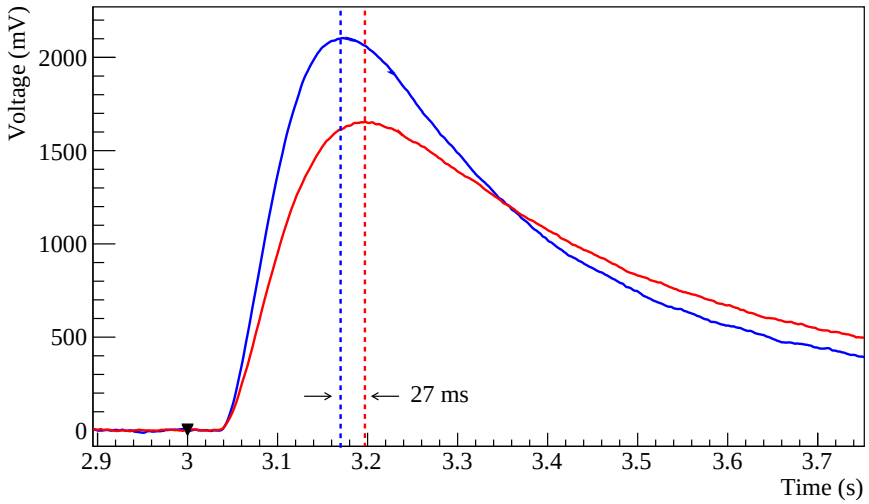

Figure 4.1.6: *The red and the blue pulses are events from channels of the same tower. These pulses belong to the same true coincidence but they have different delays due the diverse response of the bolometer. The former has a slower response compare to the latter. The vertical dotted lines indicate the position of the maximum of each pulse and the arrows indicate a jitter of about 27 ms.*

The coincidence sequence is divided in two steps: the first is measure the time jitter between channels, the second is the actual identification of events that happen at the same time within a narrow time window. The jitter is the delay between two events truly in coincidence. The spread in time is due to difference in response of each crystals: the rise time of the pulse can differs, between one crystal and the other, by up to tens of milliseconds. Figure (4.1.6) shows the comparison of two truly coincident events in the same tower and the two dotted lines put in evidence the jitter between this two pulses due to difference in response of the two bolometers.
If the jitter is not taken into account we must consider time windows of about 100 ms, while taking into account the jitters allow us to narrow this time window of about one order of magnitude. Jitters are measured using truly coincident events from ^{208}Tl line in calibration data. We run the coincidence module for one tower at the time, with wide timing windows, and we isolate the events which energy sum up to 2615 keV and thus are likely to be multiple Compton scatterings of the same 2615 keV γ-ray from ^{208}Tl . We then compute the time difference for each channel belonging to that tower, relative to a reference channel (there is one reference channel for each tower). To complete the picture

we now need to estimate the delay between the reference channels of the 19 towers. The delay between the reference channels is found by analysing the delay of heater events, after aligning the triggers. By combining the delays within each tower with the delay between reference channels of different towers we can now compute the delay between all the channels of CUORE and with it correct the pulses peak time. This allow us to use a narrow coincident time window and limit the number of accidental coincidences.
Finally `Diana` scans all the events that are close in time (within 10 ms time window), finds the coincidences and stores the multiplicity and the total energy (sum of the energies for coincident pulses) in each event.

Pulse Shape Analysis

CUORE bolometers do not allow particle or bulk-surface identification, therefore it is not possible to distinguish an α from a β/γ interaction. It is however possible to discriminate between physical, clean pulses from other events that may induce the DAQ to trigger. We call this analysis Pulse Shape Analysis (PSA). Thanks to six pulse shape variables we can check the quality of the pulse shape and selectively reject for example noise spikes, pile-up events (two events that happen in the same time window) or very noisy events. In Figure (4.1.8) there some example of events that are eliminated applying cuts on the PSA variables.

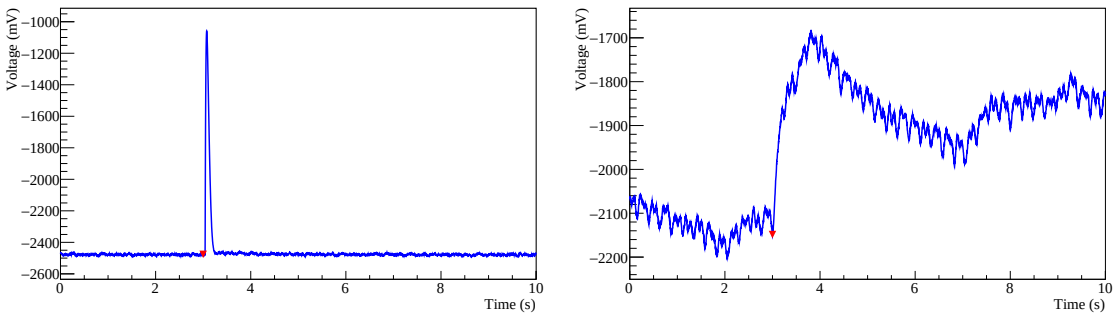

Figure 4.1.7: *Example of two events removed thanks to the PSA variables. Right: noise spike with very low rise time and decay time. Left: very noisy event in which all the PSA variables deviates from their mean. The small red triangle indicates the trigger position.*

The parameters computed and studied are the following:

- Pulse *rise time*: time difference in milliseconds between the time when the pulse is at 10% of its height and the one at 90%. Electronic noise spikes have a very short rise time that is not possible for physical pulses.

- Pulse *decay time*: time difference in millisecond taken from the pulse to fall from 90% to 30% of its height. On one hand noise spikes have a very short decay time that is not possible for physical pulses because after a particle interaction the bolometer must thermalise with the thermal bath. On the other hand pile-up that is not identified by the number of pulses variable because the two events are too close, cause the extension of the decay time.

- *baseline slope*: best-fit value for the angular coefficient of a linear fit to the first 3/4 of the pre-trigger of each event. If the baseline slope deviates too much from zero, means that the current event is situated on the tail of a previous pulse that falls out of the triggered window. In this case pulses parameters such as baseline and amplitude are badly reconstructed.

- Peak *delay*: time difference between the beginning of the event window and the maximum of the pulse. We have already seen in the coincidence paragraph that this quantity varies from channel to channel because of difference in bolometer response, but for those events in which the delay strongly deviated from its average value, the amplitude and therefore the energy are poorly reconstructed.

- *Test Variable Left (TVL)* and *Test Variable Right (TVR)*: χ^2 statistic for how much the filtered pulse looks like the filtered template pulse, or AP, on the left and on the right side of the pulse respectively.

Typically, the distributions of these shape parameters change from channel to channel because of diverse response among the bolometers, but at the same time they also change with energy and even from one dataset to an other.
For this reason the PSA algorithm models for each channel the energy-dependence of the pulse shape parameters and normalise their values. The normalised variables are built to remove the energy-dependence and place energy-indipendent cuts on the pulse shape parameters.
For each channel-dataset, the distribution of each pulse shape parameter of all events from selected spectral lines (from both background and calibration data), are plotted as a function of energy. First we use the physics data to build a signal-like event sample from events that reconstruct within 10 keV of the γ lines from ^{40}K at 1461 keV and ^{60}Co at 1173 keV and 1332 keV.
Because of outliers in the distributions, only events with Multiplicity=2 are selected to study the energy dependence. In fact events with physical coincidences are likely to be physical and not due to noise spikes, while the shape of the pulse is not influenced by the

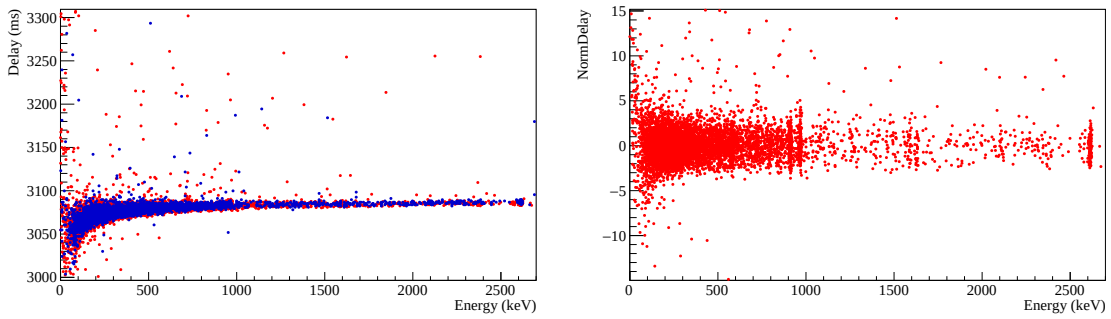

Figure 4.1.8: *Example of delay energy distribution for one channel-dataset. Left: in red the energy distribution of delay for events with multiplicity=1 and in blue for multiplicity=2 - the distribution shape is the same but there are less outliers. Right: normalized delay distribution for the same events with multiplicity=1 - the distribution is now symmetric around zero.*

coincidence. For each energy bin of these distributions we compute the median and the Median Absolute Deviation (MAD), which are both energy-dependent. Since no model can currently predict the shape of the parameter distributions, we determine the energy dependence by fitting both the medians and the MADs with phenomenological functions. Now that for each pulse shape parameter, for each channel, for each dataset, we have the energy functions for median and MAD, it possible to obtain linearised variables that do not depend on the pulse energy, using Equation (4.1.9)

$$NormPSA_i = \frac{P_i - P_{Med}(E)}{P_{MAD}(E)} \tag{4.1.9}$$

where P is any of the aforementioned pulse shape parameter and E is the energy of the event i to linearise. Note that the new linearised PSA parameters are evenly distributed around zero, at least for the physical pulses.

4.2 Data Selection

Before proceeding to high level analysis it is crucial to reject from the final set of data all the events that for one reason or the other do not comply with the expected criteria for the subsequent analysis.

4.2.1 Quality cuts

The first set of cuts are called *quality cuts* and they ensure basic data quality. We remove from the final set of data all events that are not triggered as signal events (noise and heater

events). Then we reject all the pulses which trigger time falls within a Bad Interval (time interval of high noise in the detector); in fact high noise level can influence the amplitude estimation and thus lower the overall energy resolution of the detector. Events with more than one signal trigger in its 10 sec window are also discarded together with events having a number of pulses greater than one; again the presence of more than one pulse in the same event window can lead to a wrong amplitude estimation. In future we foresee to develop an algorithm that allows the use of events with more than one pulse, providing that the two pulses are distant enough not to spoil the amplitude evaluation. Accepting events with more than one pulse in it might produce a negligible effect in the physics data (given that the event rate is very low) but it could be a significant improvement in calibration data where many events are rejected due to pile-up.

The last cut included in these quality cuts is *bad for analysis*. This cut is produced by applying some flags that for each channel are stored in the database. Each of these flags correspond to a failure of the event in one of the analysis step described above. For example a channel that is so noisy that has a very high trigger threshold could not have any good event triggered and thus it is not possible to build an AP; this channel in the database will have an AP flag and will be removed from the analysis, for one dataset, by the bad for analysis cut. The same happen if the channel fails the stabilization or if, for any reason, it is not possible to calibrate its energy.

Figure (4.2.1) shows the background energy spectrum before and after the base cuts.

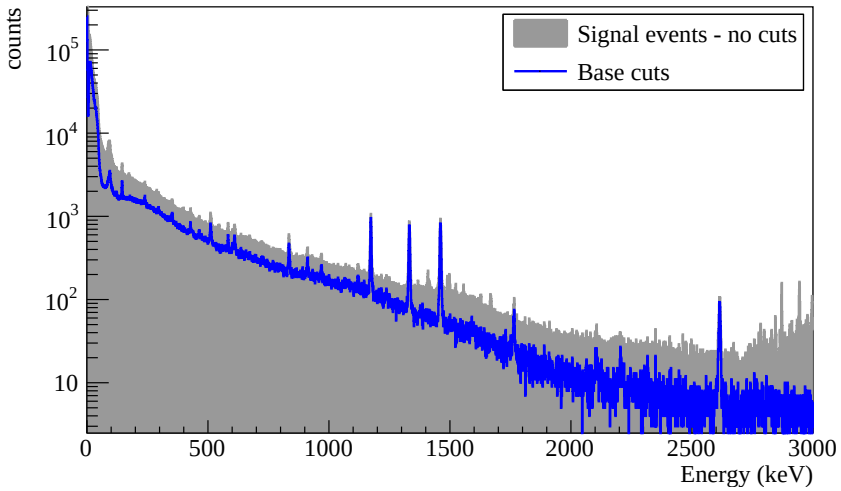

Figure 4.2.1: *In grey the energy spectrum of physics data before the base cuts, showing only signal events. In blue the energy spectrum after the base cuts.*

4.2.2 Analysis cuts

The last two reasons why an event can be rejected are its multiplicity and its pulse shape. The multiplicity cut is specific of the kind analysis: in this case we are searching for a rare event that has an high probability of being fully contained in one crystal. Therefore we select only events with multiplicity equal to one with an energy threshold of 150 keV, meaning that the selected events do not have any event in coincidence of energy greater than 150 keV, within a time window of 10 ms. Figure (4.2.2) (left) shows the background energy spectrum before and after the multiplicity cut.
The second analysis cut is the one on the pulse shape, which requires the shape of each waveform to be consistent with that of a true signal-like event. The PSA cut allows to remove pulses with features that deviates from the average signal: noise spikes, pile-up, etc. Because of the numerous pulse shape parameters, the optimization of this cut it is not straighforward as any other one-dimentional cut might be. In fact the six pulse shape parameters are usually correlated and the some of the cuts might be interchangeable, thus very difficult to optimize. To address this problem, we consider each event a point in this six-dimentional space and calculate the distance between this point and the centroid of this six-dimentional distribution. This is called Mahalanobis distance D_M [65]. We choose the upper limit on D_M that maximizes the discovery sensitivity [66].

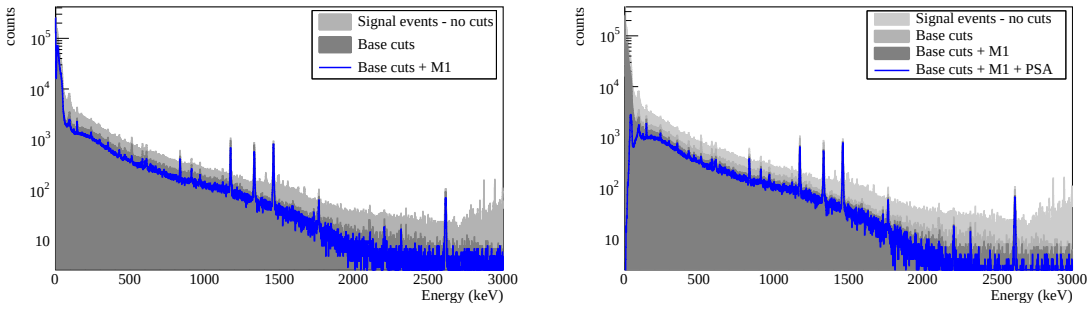

Figure 4.2.2: *In grey the energy spectrum of physics data before the base cuts, showing only signal events. In blue the energy spectrum after the base cuts.*

4.3 Detector Response

CUORE peak identification capability in the Region Of Interest (ROI 2465 - 2575 keV) highly relies on the good energy resolution of its 988 TeO_2 crystal bolometers, which in the ROI is typically of the order of $\sim$ 0.3 %. Together with the energy resolution, the

understanding of the detector response is also critical in order to use the proper line shape in $0\nu\beta\beta$ decay fit to the physics data. Obviously these two parameters are highly correlated and a correct modelling of the detector response is mandatory to obtain a reliable estimate of the energy resolution.

We establish the detector response function, and therefore also the energy resolution, using a γ line near $Q_{\beta\beta}$, namely the 2615 keV ^{208}Tl line from calibration data. The ^{208}Tl photopeak is a natural choice because it is a monoenergetic high-statistics line close to the ROI and it lies in a region where the line does not overlap with other outstanding spectral lines. CUORE detectors do not allow to do any particle discrimination, however it is worth noting that a $0\nu\beta\beta$ decay signal would not necessarily have the same line shape as the 2615 keV ^{208}Tl line because these two processes involve different types of radiation: two beta particles for the $0\nu\beta\beta$ and a single gamma for the ^{208}Tl photopeak. Indeed there are features of the ^{208}Tl line that we do not expect in the ROI such as the Compton scatter continuum and the 30 keV X-Ray escape line. However we include these components in the line shape fit with the purpose of showing our understanding of the background around the ^{208}Tl line and to increase the quality of the fit. Moreover, when applying calibration-derived line shape to the ROI fit of physics data, it is important to note that the energy resolution (or the width of the line shape) scales with energy and there might be a different from calibration and background: it is therefore necessary to fit other background spectral lines, leaving the width scale factor a free parameter and extrapolate in this way the final energy resolution at $Q_{\beta\beta}$. On the contrary it is not possible to evaluate a channel by channel detector response directly on the background spectral lines because of lack of statistics (on average there are only few events per channel per dataset in each spectral line).

CUORE detector response analysis mainly follows the CUORE-0 one described by Tom Banks in his internal note [67], and it is based on CUORE-0 code developed by Jon Ouellet for his PhD thesis [68]. We performed Unbinned Extended Maximum Likelihood (UEML) simultaneous fit separately on each tower with the Roofit software package.

4.3.1 Fit Function and Detector Response Model

In order to properly model the detector response we build for each channel a Probability Density Function (PDF) which is the sum five components described below:

$$\begin{aligned} ModelPDF(Ch, Ds) = & N_{Sig} \cdot PhotoPeak \\ & + N_{Comp} \cdot ComptonFunc \\ & + N_{XRay} \cdot XRayFunc \\ & + N_{Coin} \cdot CoincidentPeakFunc \\ & + N_{bkg} \cdot BkgFunc \end{aligned} \tag{4.3.1}$$

where *PhotoPeak* is the peak due to 2615 keV ^{208}Tl line; *ComptonFunc* is the Compton edge of the ^{208}Tl peak; *XRayFunc* is an X-Ray escape peak; *CoincidentPeakFunc* is a peak due to coincident γs; *BkgFunc* is a first order polynomial representing the background.

From preliminary studies of the calibration data at 2615 keV ^{208}Tl line, it was clear that CUORE detectors exhibit a slightly non-Gaussian detector response. This is not surprising giving that a similar effect was already observed in CUORE-0 [44] and Cuoricino [69, 70], however we do not have yet a univocal explanation for the origin of this structure.

Unlike CUORE-0, which used the sum of two gaussians as detector response model, we empirically describe the non-Gaussian behaviour with the sum of three Gaussians. In CUORE this behavior is however not evident in all the channels but only on those channels with higher resolution, while in other channels this effect is only suggested by a small excess of events in the low energy part of the ^{208}Tl photopeak. A CUORE collaborator, Tom Banks, in his internal note on energy resolution [67] tried to make some hypothesis on origin of this structure in CUORE, from some physical effect that has not been accounted for, to position dependent energy deposition in the crystals and phonon propagation, to problems that arise somehow from the DAQ electronics or analysis procedure. In the end the truth is that this feature of the ^{208}Tl photopeak is not well understood.

Other alternative functions have been tried before finalizing the line shape model the way I will present it here: first of all, given the poor energy resolution of the first CUORE data compared to CUORE-0, we tried to use simpler models to describe the ^{208}Tl PhotoPeak, but all fit results were worst than those obtained with the model chosen for this analysis. We found indeed that this model provides a better description of the CUORE first data compared to other models considered. In any case, since the choice of line shape is arbitrary and it is not based on any physical explanation, we will include in the systematics a term that represents our ignorance on the detector response model, which we discuss later in

this Thesis. Given the low background level in most of the channels, we also tried to remove the three extra components that do not contribute to the detector response, one at the time: the 30 keV X-Ray peak and the background and the coincident peak. In all three cases the fit results were worst without than with these extra components of the line shape model and for some towers the fit did not even converge. These three components are indeed not included in the detector response, but their presence in the fit is crucial for the quality of the fit, for the outcome of the detector response and to demonstrate that we understand our spectrum.
Now, after discussing the possible deviation from the model we choosed to used in this analysis, let us discuss the model itself. Each component of Equation (4.3.1) represents a feature of the spectrum in the region of 2615 keV ^{208}Tl line in calibration data. The following list describes the role and the explicit form of each component in the PDF that encloses the detector response model.

PhotoPeak

The PhotoPeak component represent the detector response function that will be used to fit the ROI and is therefore the only component that will be propagated to the subsequent steps of the $0\nu\beta\beta$ decay analysis of ^{130}Te . The PhotoPeak is modelled as the sum of three Gaussians, a primary Gaussian called *main-peak* and two secondary Gaussians called *sub-peaks*, one on the low and the other on the high energy side of the main-peak.

$$PhotoPeak = \frac{1}{\sqrt{2\pi}\cdot\sigma}\cdot e^{-\frac{(x-\mu)^2}{2\sigma^2}} + R_L\cdot e^{-\frac{(x-E_{RL}\cdot\mu)}{2\sigma^2}} + R_H\cdot e^{-\frac{(x-E_{RH}\cdot\mu)}{2\sigma^2}} \tag{4.3.2}$$

where μ is the fitted position of the ^{208}Tl full absorption peak (Q-Value of the ^{208}Tl line) and σ is its resolution, which is forced to be the same for the three gaussians; R_L is the events ratio with respect to the main-peak that goes into the low energy sub-peak; R_H is instead the events ratio with respect to the main-peak that goes into the low energy sub-peak. Accordingly, in the final fit of the spectrum in the ^{208}Tl region, the total number of events in the PhotoPeak, N_{Sig}, is given by the following expression:

$$N_{Sig} = N_{main}\,(1 + R_L + R_H) \quad \Rightarrow \quad \begin{cases} R_L = N_{sub-low}/N_{main} \\ R_H = N_{sub-high}/N_{main} \end{cases} \tag{4.3.3}$$

where N_{main} is the number of events in the main-peak, $N_{sub-low}$ and $N_{sub-high}$ are respectively the number of events in the low energy and high energy sub-peaks.
In Equation (4.3.2) E_{RL} and E_{RH} are the energy ratio of the low and high energy sub-

peaks with respect to the position of the main-peak μ. The Gaussians of the sub-peaks results indeed centered at $E_{RL} \cdot \mu$ and $E_{RH} \cdot \mu$ respectively. In all three Gaussians the width is kept the same in order to limit the proliferation of degrees of freedom in the UEML simultaneous fit.

Compton continuum

The *ComptonFunc* component of the line shape fit is an effective representation of the Compton edge due to scattering γs from ^{208}Tl decay line. This is described by a smeared step function, which well describes the data in the energy region of the fit, namely the complementary error function reported in Equation (4.3.4)

$$ComptonFunc = \frac{1}{2} \cdot Erfc\left(\frac{x-\mu}{\sqrt{2}\cdot\sigma}\right) \tag{4.3.4}$$

where σ and μ are the same as for the PhotoPeak component of the PDF. The smeared step function is thus centred at the ^{208}Tl full absorption peak position.

X-Ray escape peak

The X-Ray escape peak is due to Te X-Ray emission following an incident 2615 keV γ ray from ^{208}Tl . The strongest Te X-Ray emission lines have energies ranging from 27 to 31 keV and, when escaping the crystal volume, the effect is a peak at about 30 keV below the 2615 keV PhotoPeak, composed by multiple adjacent X-Ray escape lines and thus not representable with a single Gaussian. The implementation of the X-Ray escape peak used in this analysis involves the six major known X-Ray lines, each one represented by a Gaussian with different intensity and position, but with the same width σ. Again, in order to restrict the number of parameters in the fit, σ is the same as for the PhotoPeak and for the Compton continuum. The PDF component for the X-Ray escape peak is the following:

$$XRayFunc = \frac{1}{\sqrt{2\pi}\cdot\sigma\cdot W} \cdot \sum_{i=1}^{6} R_i \cdot e^{-\frac{(x-\mu+E_i)^2}{2\sigma^2}} \tag{4.3.5}$$

where W is the total weight

$$W = \sum_{i=1}^{6} R_i \tag{4.3.6}$$

R_i are the intensities of each single X-Ray line, relative to the number of events in the^{208}Tl line; E_i are the energies of X-Ray emission lines of Te, so that the actual po-

sition of each of the six lines is given by the difference μ-E_i. The values for R_i and E_i, taken from the CUORE Monte Carlo, are reported in the Table (4.3.1).

i	R_i	$E_i(keV)$
1	$3.20{\cdot}10^{-4}$	27.20
2	$6.08{\cdot}10^{-4}$	27.47
3	$2.61{\cdot}10^{-4}$	30.96
4	$5.90{\cdot}10^{-6}$	31.22
5	$6.01{\cdot}10^{-5}$	31.65
6	$5.02{\cdot}10^{-6}$	31.80

Table 4.3.1: *Values of events ratio and energy differences for the six adjacent lines composing the X-Ray escape peak at about 30 keV below the Q-Value of the ^{208}Tl γ line.*

In the detector response model, the intensity of the X-Ray escape peak is expressed as the relative intensity to the ^{208}Tl PhotoPeak

$$N_{XRay} = N_{Sig} * R_{XRay} \tag{4.3.7}$$

Coincident peak

Within the energy range of the fit another peak is present at 2687 keV. This line is the effect of coincident absorption of the 2615 keV and 583 keV γs from ^{208}Tl , followed by pair production and the subsequent escape of a 511 keV annihilation γ. This peak is represented in the fit function with the Gaussian of Equation (4.3.8)

$$CoincidentPeakFunc = \frac{1}{\sqrt{2\pi}\cdot\sigma}\cdot e^{-\frac{(x-E_R\cdot\mu)^2}{2\sigma^2}} \tag{4.3.8}$$

where E_R is the ratio between the actual position of the 2687 keV coincident peak and the Q-value of ^{208}Tl (centred in μ), and σ is once again the same width of all other Gaussians present in this model. In the final line shape fit the number of events N_{Coin} belonging to this component is given by

$$N_{Coin} = N_{Sig} * R_{Coin} \tag{4.3.9}$$

where R_{Coin} is the ratio of the events in the 2687 keV coincident peak relative to the ^{208}Tl PhotoPeak.

Linear background

The linear background is mostly due to coincident events with a small contribution from degraded alpha. This continuum is modelled simply with a first order polynomial.

$$BkgFunc = p_1 \cdot x + p_0 \tag{4.3.10}$$

where p_1 is the slope of the polynomial and p_0 is the intercepts and it is determined by the normalization to the total number of events. The number of events that contribute to this flat background is N_{bkg}.

4.3.2 Simultaneous Fit and Parameter Initialization

The line shape is simultaneously evaluated on each channel-dataset pair, for each tower, with an UEML independent fit in the energy range 2530–2720 keV. A simultaneous fit over the full array is possible, but was not performed in this analysis for computational convenience. The caveat is that all those parameters that are supposed to be global, have been evaluated by tower. On one hand, creating 19 independent fit is also a workaround to avoid any assumption on the position-dependent background rate inside the detector, but on the other hand 52 bolometers are sufficient to properly fit all the features of the line shape: an independent fit on each channel is indeed not feasible because of the lack of statistics. This however did not influence the quality of the detector response since the PhotoPeak component is channel-dataset dependent.
The simultaneous fit runs over the sum of all the Ch-Ds PDFs related to that tower:

$$SimulFit(T) = \sum_{Ch-Ds} ModelPDF(Ch - Ds) \tag{4.3.11}$$

where T stands for tower and the Ch-Ds index runs over all the channel-dataset pairs. In the simultaneous fit there are parameters Ch-Ds dependent and other parameters that are Global, hence these are the only parameters that are fit across all the datasets and all the channels belonging to the tower in object. Global quantities are related only to the physics of ^{208}Tl decay and therefore do not change with time or spatial position. The only exception is the background ratio which in principle might depend strongly on the crystal position with respect to the calibration strings and it might change with time, but the statistics is not high enough to appreciate those effects.
The parameters needed to fit each tower are summarized in Table (5.2.1) where is also reported the number of parameters needed for each of the fit component given that the data acquired so far with CUORE is divided in two datasets. It is important to remark

that in the current implementation of the line shape fit the coefficients of all the model components are defined as event rates so that their value does not depend on the individual exposure of each Ch-Ds pair. The exposure is given by (livetime·mass) and is expressed in kg·yr. Following this change of notation the fit parameters that indicate the number of events in each component become:

$$\begin{aligned} \eta_{Sign}(Ch-Ds) &= N_{Sign}(Ch-Ds)/\epsilon(Ch-Ds) \\ \eta_{Comp} &= N_{Comp}/\sum_{Ch-Ds}\epsilon(Ch-Ds) \\ \eta_{Bkg} &= N_{Bkg}/\sum_{Ch-Ds}\epsilon(Ch-Ds) \end{aligned} \tag{4.3.12}$$

where (Ch-Ds) runs on the channels of a single tower at the time. Note that the exposure ($\epsilon(Ch-Ds)$) is different for each Ch-Ds for the reasons exposed in Section (4.2) and because there might be a very small difference in the crystal masses, but is constant and thus it does not contribute to the total numbers of parameters.

Parameter	Domain	Range	Par. Number
η_{Sig} (counts/keV/kg/yr)	Ch-Ds	–	104
μ (keV)	Ch-Ds	2608 – 2622	104
σ (keV)	Ch-Ds	–	104
R_L	Ch-Ds	0. – 0.7	104
R_H	Ch-Ds	0. – 0.9	104
E_{RL}	Ch-Ds	0.992 – 0.999	104
E_{RH}	Ch-Ds	1.0007 – 1.015	104
η_{Comp} (counts/keV/kg/yr)	Global	–	1
R_{XRay}	Global	10^{-4} – 10^{-2}	1
R_{Coin}	Global	10^{-10} – 10^{-2}	1
E_R	Global	1.0256 – 1.0294	1
η_{Bkg} (counts/keV/kg/yr)	Global	–	1
p_1 (counts/keV)	Global	-1 – 0	1
Total Parameter for 1 Tower			734
Total Parameter for full detector (19 Towers)			13 838

Table 4.3.2: *Values of events ratio and energy differences for the six adjacent lines composing the X-Ray escape peak at about 30 keV below the Q-Value of the ^{208}Tl γ line. The components that do not have a range associated are those that have been initialized with the data: their range is different for each Ch-Ds and it is computed from the initialization value.*

In order to help the convergence of the fit, it is necessary to find proper input values for some of the most important parameters of Table (5.2.1). This is why η_{Sig} , σ, η_{Comp} and

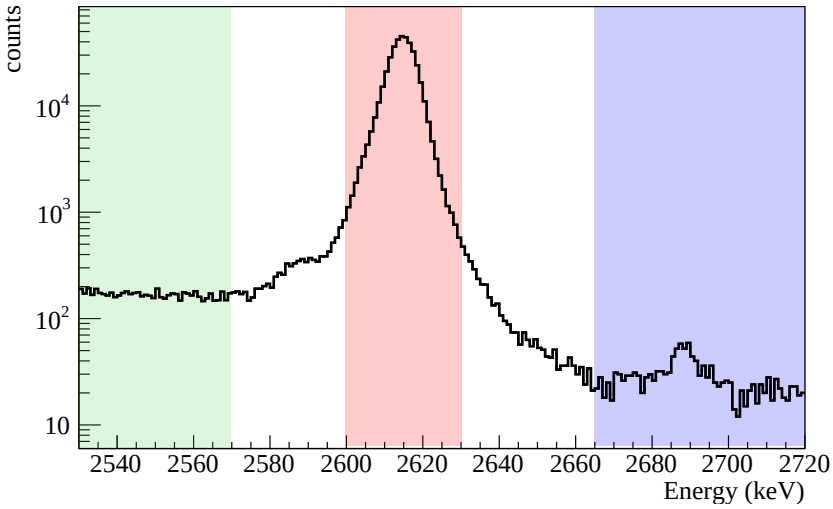

Figure 4.3.1: *Energy spectrum of all channel-datasets showing the 2615 keV ^{208}Tl line. The colors indicate the regions integrated to initialize some the fit parameters from data: green for the Compton, red for the PhotoPeak and blue for the background. Note that this plot is only illustrative of the initialization method.*

η_{Bkg} initialization values are obtained directly from the data by integrating different areas of the spectrum as shown in figure Figure (4.3.1).

η_{Bkg} and η_{Comp} are evaluated on the sum spectrum of the tower, while the η_{Sig} and σ are evaluated by Ch-Ds. The integral on the high energy side of the ^{208}Tl peak, marked in magenta in Figure (4.3.1), multiplied by the entire energy range, is the initialization value for the background. Instead the integral on the low energy side of the ^{208}Tl peak, marked in green in Figure (4.3.1) is the initialization value for the Compton. Finally the integral under the ^{208}Tl photopeak, from 2600 to 2630 keV is the initialization value of the peak signal rate, while the width of the peak is the initialization value of the σ. Without a proper initialization of the fit parameters the convergence of the fit is not guarantee.

There is also an other small trick to make all these parameters converge in the simultaneous fit. In fact some channels do not have prominent secondary peaks (or they are hidden within the peak resolution) and this cause the degeneracy between the primary and the two secondary Gaussians of the ^{208}Tl photopeak. The trick consists in running the fit multiple times in an iterative process: the first time the simultaneous fit is run, independently for each tower, keeping the parameters of the secondary peaks of the PhotoPeak component constant to some reasonable values. The second time we run the simultaneous fit, we seed the parameters with the results from the first round, this time keeping all the parameters

constant but those belonging to the two sub-peaks. Then the same procedure is repeated a third time fixing again the sub-peaks parameters and leaving all the other free. In this way we can obtain a full convergence and accurate error matrix for all the towers, without having to manually tune each parameter.

4.3.3 Detector Response Fit Results

Finally, the fit result on the 2615 keV ^{208}Tl calibration line shows that the detector response model of Equation (4.3.1) describe quite well the data. In order to show the complete set of fit results all 19 plots should report here, one for each tower with all the components. However for space convenience I chose to represent as fit results only one representative plot showing the sum of 19 tower-dependent UEML fits, together with the combined histogram of all calibration data around 2615 keV for both datasets. This sum is shown in Figure (4.3.2) in both linear and logarithmic scales, together with the ratio between data and model with the purpose to quantify the quality of the model. The ratio of Figure (4.3.2) is consistent with one at almost all energies confirming the good quality of the detector response model. However the ratio has some deviation from one in the energy range 2630–2680 keV indicating features of the line shape that are not well modelled by our fit function.

In Figure (4.3.3) is reported, for illustration purposes only, the ^{208}Tl line fit result for Tower 1 and in Figure (4.3.4) there are the fit results for two different channels as example of the channel-level fit. I remind here that the only component of the line shape fit that matters in the subsequent $0\nu\beta\beta$ decay analysis is the Ch-Ds PhotoPeak component.

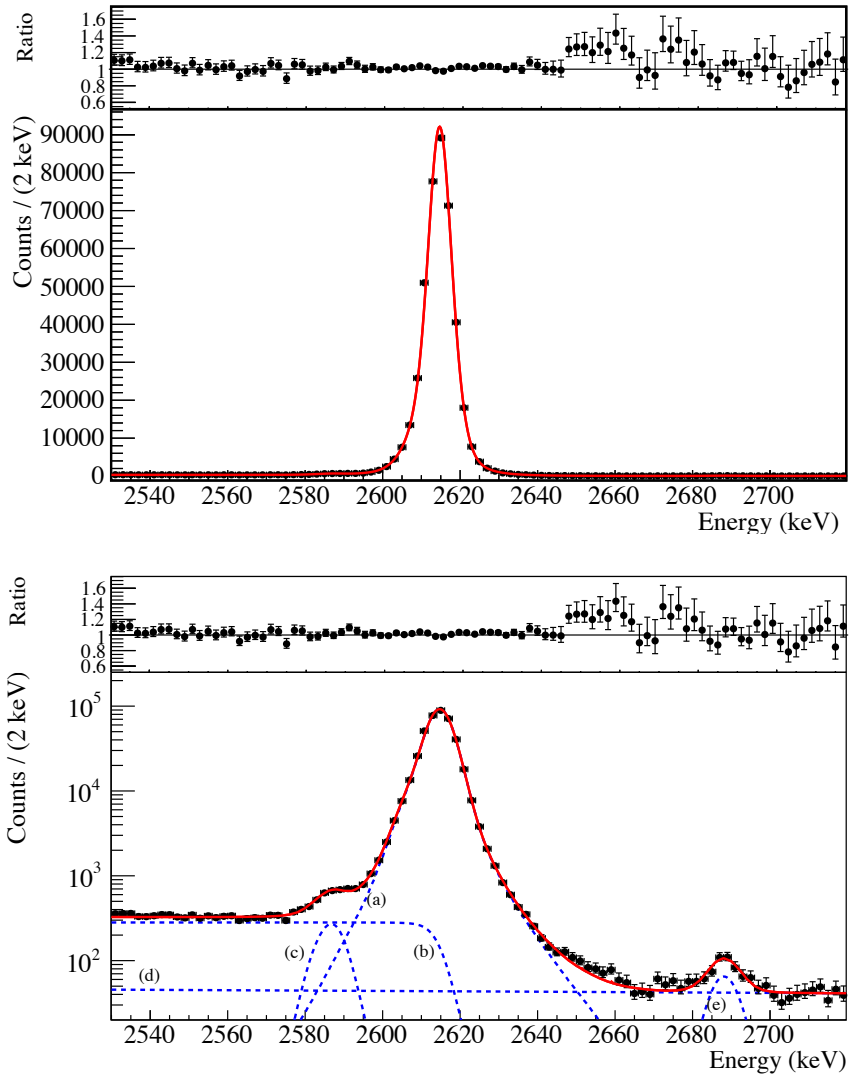

Figure 4.3.2: *Top: sum of the results of the 19 tower-dependent UEML fits we use to estimate the detector response of each channel–dataset in calibration data, in linear scale. The solid red line is the sum of the best-fit line shape model of each channel–dataset. Bottom: sum of the results of the 19 tower-dependent UEML fits we use to estimate the detector response of each channel–dataset in calibration data, in logarithmic scale. The components of this summed best-fit model are shown by the blue dashed lines. We identify (a) the multi-Gaussian photopeak that describes the detector response function, (b) a multiscatter Compton contribution, (c) multiple peaks due to 27–31 keV Te X-ray escape following an incident 2615 keV γ ray, (d) a linear continuum background due to coincident events, and (e) a line due to coincident absorption of 2615 keV and 583 keV γ rays from the ^{232}Th decay chain followed by escape of a 511 keV annihilation γ from pair production. On the top of these two plots is reported the ratio between calibration data and line shape model.*

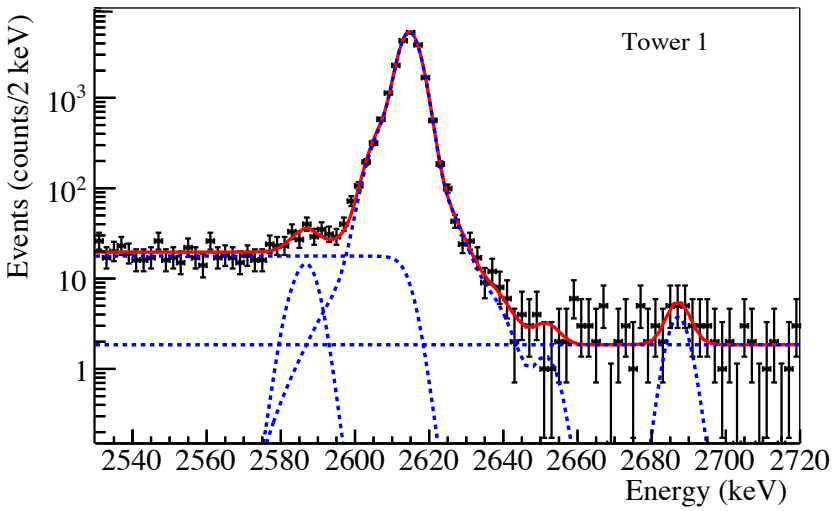

Figure 4.3.3: *Example of line shape fit for Tower 1 and its components: solid red line for the overall tower simultaneous fit, blue dashed lines for the photopeak, Compton, 30 keV X-Ray peak, 2687 keV concidence γ peak and linear background.*

In addition to the detector response, from the line shape fit is also possible to infer the energy resolution in calibration data for each channel-dataset pair. Figure (4.3.5) shows on the left the distribution of the Ch-Ds FWHM for the data used in this analysis and on the right the comparison of the same distribution for the two dataset separately. From this last plot it is clear that the optimization campaign described in Chapter (3) was effective. In fact the average resolution of dataset 3021 is higher than the one of dataset 3018 by 1.6 keV.

From the distribution of Figure (4.3.5) is possible to extract an important figure of merit for the experiment: the effective FWHM for the full detector. This figure of merit is obtained as the harmonic mean of the Ch-Ds FWHM weighted for their exposure:

$$FWHM_{eff} = \frac{\sum_{Ch-Ds} \epsilon(Ch-Ds)}{\sum_{Ch-Ds} \epsilon(Ch-Ds)/FWHM(Ch-Ds)} \tag{4.3.13}$$

where $\epsilon(Ch-Ds)$ is the channel-dataset pair exposure and $FWHM(Ch-Ds)$ is the channel-dataset pair energy resolution in calibration. Considering the data acquired up to now the effective FWHM in calibration is 8.0 keV.

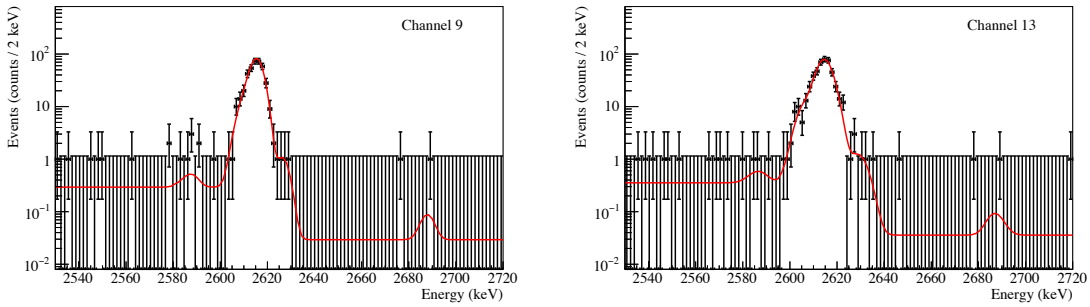

Figure 4.3.4: *Example of line shape fit for channels 9 and 13 from Tower 1, summed over of both datasets. The solid red line is the single channel simultaneous fit and the black dots represent the data histogram.*

4.4 Scaling the ^{208}Tl fit to the ROI

The ROI is a region of the spectrum around $Q_{\beta\beta}$, that ranges from 2465 keV to 2575 keV. In addition to the hypothetical line due to $0\nu\beta\beta$ decay, an other peak from the background lies in this region, namely the coincidence of 1173 keV and 1332 kev γ rays from ^{60}Co. The approach adopted in fitting these two peaks of the ROI is to shift the detector response obtained from Equation (4.3.2) down to the position of $Q_{\beta\beta}$. In doing so we want to freeze as many parameters as possible, leaving free only the expected position of the peak (only for the ^{60}Co) and the event rate, while setting to constant all the other features including the lines width (corrected for the proper scaling factor) and the low and high energy sub-peaks.
Before fitting the ROI, in this section we will estimate if there is a residual bias in the reconstructed energy estimator and possible systematic differences of the energy resolution in physics data with respect to calibration data, used to evaluate the detector response. Due to the higher event trigger rate during calibration data taking, it is indeed possible that the energy resolution differs from calibration to background.

4.4.1 Energy Resolution

To evaluate possible systematic differences in the detector energy resolution we fit the most prominent lines from the background spectrum with Equation (4.3.2) to model the peak and a linear function to model the background. Figure (4.4.1) shows which lines of the background spectrum are used for the evaluation of the energy resolution scaling factor and to evaluate the energy bias. Ranking for increasing energy the spectral lines are 835 keV from ^{54}Mn, 911 keV from ^{228}Ac, 1173 keV and 1332 keV from ^{60}Co, 1462 keV from ^{40}K and

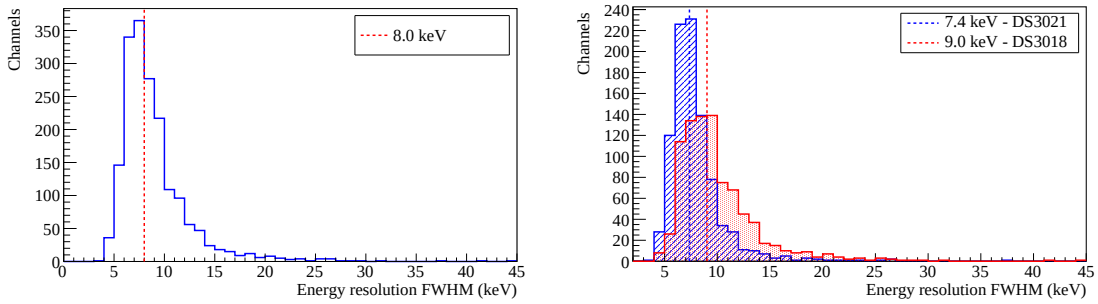

Figure 4.3.5: *Left: Energy resolution (FWHM) distribution for all the 889 channels present in the this analysis. The red dotted line indicates the mean value of the overall energy resolution evaluated in calibration data at 2615 keV. Right: energy resolution distribution evaluated at 2615 keV in calibration data for the active channels of dataset 3018 (blue) and dataset 3021 (red). The blue and red vertical dotted lines indicate the mean energy resolution for datasets 3018 and 3021 respectively.*

finally 2615 keV from ^{208}Tl .
Unlike the line shape discussed in Section (4.3), the fit is performed on the whole detector and not independently by tower, otherwise the statistics would not be enough to give reliable results. We use again a simultaneous UEML fit on all the channels-dataset pair where the fit function used for each channel and dataset is given by

$$BkgPeak(Ch, Ds; x) = PhotoPeak(\mu(Ds), r_\sigma(Ds)\sigma(Ch, Ds); x) + p_1 \cdot x + p_0 \quad (4.4.1)$$

where x runs over the an energy range of about 100 keV around the theoretical position of the spectrum line and μ and r_σ are dataset dependent parameters representing the mean of the peak and the scaling factor for the line width σ. The parameter σ is constant for each Ch-Ds and comes from the line shape fit together with position and intensity of the two sub-peaks of the detector response function. When summing the channels-dataset dependent fit functions into the PDF that represent the background peak model we assume that all the channels have the same event rate and hence the rate can be taken out of the sum

$$\begin{aligned} BkgPeak(x) &= \alpha_{Peak} \sum_{Ch,Ds} \epsilon(Ch - Ds) \cdot BkgPeak(Ch, Ds; x) \\ &= N_{Peak} \sum_{Ch,Ds} BkgPeak(Ch, Ds; x) \end{aligned} \quad (4.4.2)$$

where α_{Peak} is the signal rate. If one wants to get an accurate model of the spectral lines, the signal rate should be at least layer dependent, meaning that it should be a function

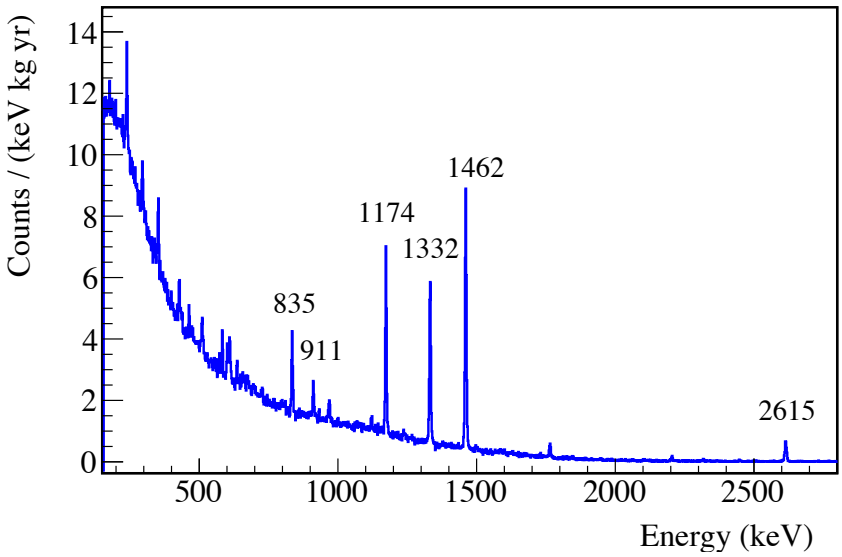

Figure 4.4.1: *Main lines of the background spectrum summed on all the channel-datasets, used to estimate the energy resolution scaling factor and energy bias.*

of the distance from the centre of the detector. In fact we expect the inner bolometers to have a lower trigger rate than the outer ones because the former are shielded by the latter from the radioactive background coming from the cryostat materials. However, after we found that accounting for layer dependence has little effect on our results, we decided for simplicity to stick with a model where the signal rate is uniform across the detector. Thus, for each of the six spectral lines there are six floating parameters: the peak position μ, two scaling factor r_σ (one for each dataset), two parameters p_1 and p_0 for the background modelling and the signal rate α_{Peak}.

The results of the fits to the six spectral line are shown in Figure (4.4.2).

We model the energy dependence of the scaling parameters as a quadratic function and then we extrapolate the scaling factor to $Q_{\beta\beta}$. In this way we account for two effect that we do not have under control: the first is the energy dependence of the resolution, since the $Q_{\beta\beta}$ is about 88 keV lower than the position of 2615 keV where the detector response is evaluated.

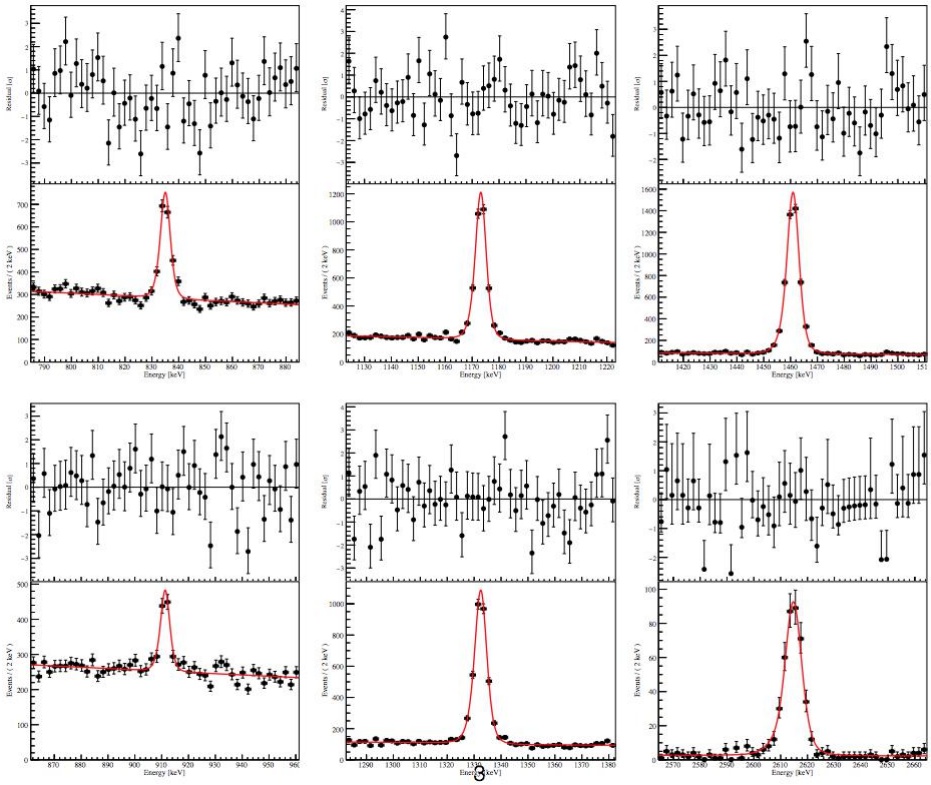

Figure 4.4.2: *Fit to the main lines of the background spectrum used to estimate the energy resolution scaling factor and energy bias. From left to right there are* ^{54}Mn *on the top and on the bottom* ^{228}Ac*, two* γ *line from* ^{60}Co*,* ^{40}K *on the top and* ^{208}Tl *on the bottom.*

The second, as already mentioned, is due to the difference between calibration and background: first of all the former has higher trigger rate than the latter therefore the cuts may have a different effect; secondly the duration of the physics data taking is longer, giving possible shifts in energy. The truth is that we do not fully understand either the energy dependence and the difference between calibration and background and thus we must model somehow our ignorance in an effective model. To do so, for each dataset we fit with a second order polynomial the scaling factor as a function of the energy which result is shown in Figure (4.4.3); then we evaluate the resulting fit function at $Q_{\beta\beta}$.

Afterwards we correct each Ch-Ds FWHM of the detector response for the extrapolated scaling factor ($FWHM(Ch, Ds) \cdot \tilde{r}_\sigma(Ds)$). Finally we evaluate the effective energy resolution in physics data of the two dataset with the harmonic mean of the corrected Ch-Ds

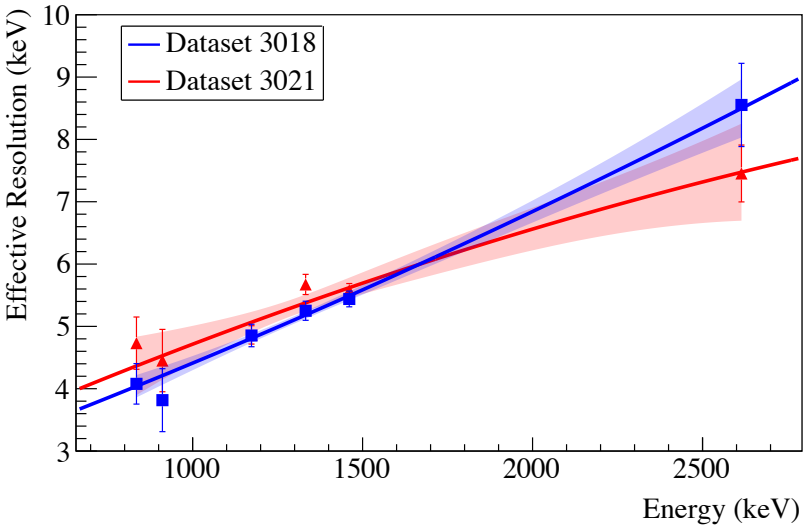

Figure 4.4.3: *Energy resolution trend in physics data. The blue marker represent the best fit position of the background spectral lines for dataset 3018 and the red markers represent the best fit position of the same background spectral lines for dataset 3021. The blue and red lines indicate the best fit of the energy resolution trends for dataset 3018 and 3021 respectively.*

FWHM weighted for the exposure which expression is given in Equation (4.4.3).

$$FWHM_{eff}(Ds) = \frac{\sum_{Ch} \epsilon(Ch, Ds)}{\sum_{Ch} \epsilon(Ch, Ds)/[\tilde{r}_{\sigma}(Ds) \cdot FWHM(Ch, Ds)]} \tag{4.4.3}$$

The effective energy resolutions are summarized in Table (4.4.1).

Dataset	$\tilde{r}_{\sigma}$	Eff. Energy Resolution (keV)
3018	0.929±0.072	8.3±0.4
3021	0.973±0.060	7.4±0.7

Table 4.4.1: *Effective energy resolution in physics data for the two datasets and the respectively scaling factor for the detector response width.*

In conclusion, to quote a single figure of merit for the energy resolution of our entire exposure, we combine the effective energy resolutions of Table (4.4.1), finding total a resolution of 7.7±0.5 keV FWHM.

4.4.2 Energy Bias

The fits to the six spectral lines, described in the previous section, allow us to measure another quantity, namely the energy bias that we introduce in calibration by using a Gaussian line shape instead of the fancy detector response function that we described in Section (4.3). We want to know the calibration bias as a function of energy so that if this bias is significant we are able to extrapolate the energy bias at $Q_{\beta\beta}$ and correct its position. To build the calibration bias trend we calculate the peak position residual from each one of the six spectral lines of Figure (4.4.2) as the difference between the best-fit position μ and the expected position for that line. We then fit this residual as a function of energy with a second order polynomial. The calibration bias is computed for the full exposure and not for each dataset independently, unlike the energy resolution in physics data. Figure (4.4.2) shows that after all, the peak residuals are consistent with zero, thus demonstrating that it is not possible to appreciate any coherent deviation from the energy value found in calibration.

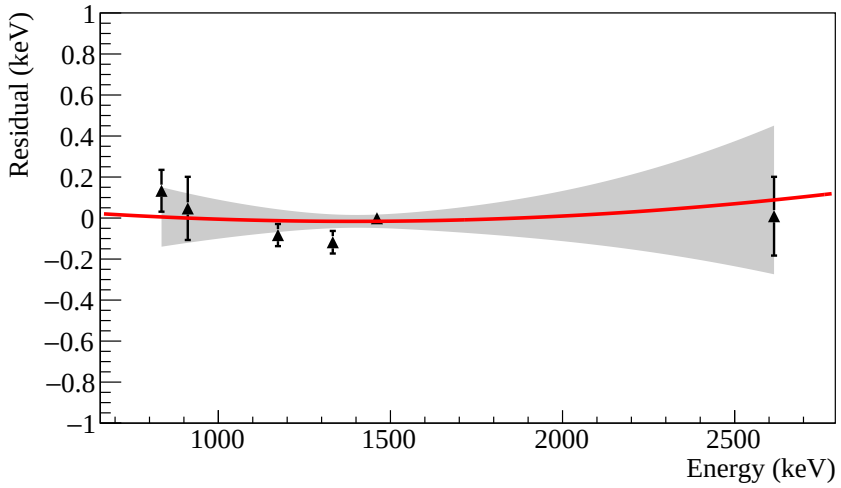

Figure 4.4.4: *Spectral lines peak residuals as a function of energy to evaluate the calibration bias in physics data. The peak residuals are computed for the entire exposure.*

In the end $Q_{\beta\beta}$ is not correct for the calibration bias, however an arbitrary systematic uncertainty of 0.5 keV is assigned to the $0\nu\beta\beta$ peak position as we will see later on in the next Chapter.

Chapter 5

Results

In this Chapter I will present the last steps of the $0\nu\beta\beta$ analysis. In Chapter (4) we went through the data production, analysis cuts, or event selection, and the evaluation of the channel-dataset dependent detector response. Now we will evaluate the efficiency of the event selection, in order to obtain a true measure of the signal rate for $0\nu\beta\beta$ decay hypothetical peak, we will fit the region in the energy spectrum which contains the Q-value of the $0\nu\beta\beta$ decay and from there we will proceed in the evaluation of the systematics introduced in this analysis, follow by the calculation of the limit on the decay rate of ^{130}Te in the $0\nu\beta\beta$ decay channel.

5.1 Efficiencies

The event selection carried out in the previous Chapter is composed by a number of cuts, each one designed to remove events that are not suited for our specific analysis. In theory these cuts are supposed to disregard undesired events and keep desired events only. Despite the careful tuning of the analysis cuts, their application to the data has also the drawback that accepts some bad events and removes some good ones. The former problem is solved by applying multiple cuts which are somehow redundant on the same population of bad events, while the for latter the only solution is to account for the good events thrown away, by evaluating the cut efficiency. Cut efficiency is defined as the fraction of good events passing the cut under examination.

We can categorise the cuts in base cuts and analysis cuts: the former have the role of rejecting events happening in intervals of low quality data, events that clearly show signs of pile-up and events whose energy is poorly reconstructed. The latter category includes pulse shape analysis and anti-coincidence cuts, ensuring that the pulse have the expected

shape for a particle interaction and that the interaction is not in physical coincidence with other events.
In the following Sections, I will describe the procedure for the efficiency evaluation of both basic quality cuts, using pulser signal, and the PSA and coincidence cuts, using background data. For further details on the event selection efficiency evaluation I refer to the internal note [71].

5.1.1 Efficiency of Basic Data Quality Cuts

The procedure for the efficiency of the basic data quality selection uses the events from the same heater pulser used for thermal gain stabilization, which has an energy close to the ROI. The quantity to be evaluated here are three: *Detection efficiency*, *Energy reconstruction efficiency* and *Pile-up rejection efficiency*. Only in the case of the basic quality cuts, for computational reasons, we evaluate the efficiency channel by channel for each run independently, and then we average the resulting efficiencies of each dataset separately to get a unique indicator for the selection efficiency of each dataset.

The *Detection efficiency* consists in the same procedure used in Section (3.2.3) where we evaluated the derivative trigger efficiency. The algorithm selects the stabilization pulser events from a given channel-run and checks if for each pulser flag there is also a derivative trigger flag. In addition, we noticed that because of a problem in few pulser board performances, it happened rarely that a pulser board did not fires, but the pulser flag was found anyway in the data. For what concerns the efficiency study we must decouple the performances of the pulser boards from the trigger mis identification of pulser events, thus we develop a cut that eliminates pulser events without pulses in it. In the end, after eliminating the events without any pulse, the detection efficiency is defined as the fraction of pulser events triggered $N_{pulser}^{triggered}$ over the total number of pulser events N_{pulser}

$$\xi_{Det} = \frac{N_{pulser}^{triggered}}{N_{pulser}} \, . \tag{5.1.1}$$

The *Energy reconstruction efficiency* is the only efficiency that is not based on a cut applied to the data but represents the portion of events which energy has been properly reconstructed by the data production. In fact the mis reconstruction of the energy variable, from our point of view, is equivalent to a selection cut: the consequence is a lesser number of events in the final energy spectrum or in particular in the ROI. To evaluate this efficiency we choose again to use pulser events since they ensure a constant power injection for each pulse, equivalent to pulses of the same energy. We study the spread in energy of these

events by building the energy spectrum associated with the stabilization pulser events and, assuming to have a gaussian distribution, we evaluate its mean and its width(σ). Events having their energy in a 3σ range from the mean of the distribution are classified as well reconstructed and compared with the whole ensemble of pulser events. The energy reconstruction efficiency result indeed the following

$$\xi_{En-Reco} = \frac{N_{pulser}^{3\sigma}}{N_{pulser}^{10\sigma}} \, . \tag{5.1.2}$$

The last efficiency evaluation, within the data quality cuts category, is related to the rejection of events showing in the same event window more than one pulse, caused by either signal or pulser, namely pile-up. Among the basic quantities computed in the low level data processing there are the variables NumberOfPulses and the SingleTrigger. The former one identifies with an offline algorithm the number of pulses in each event; the latter is a boolean variable indicating whether or not the online derivative trigger has found more that one trigger within the same event window (if more than one trigger is identified in the same event window, the SingleTrigger variable is set to false). These two variables are expected to give the same results, however we decided to keep both selections (NumberOfPulses == 1 & SingleTrigger) in our pile-up rejection cut, for redundancy.
Despite the simpleness of the related cut, the evaluation of *Pile-up rejection efficiency*, must take into account for several contributions. We define "good signal" an event without pile-up, with only one pulse in it; the probability to have a good signal, derives from the combined probabilities that there is no second signal neither an heater pulse in the same event window. The probability that giving an event window we can find a second signal pulse in it is equivalent to the probability of having a second signal pulse in a pulser event, since they both depend on the signal rate.

$$\begin{aligned} P(goodSignal) &= P(no2^{nd}signal|signal) \times P(noPulser|signal) \\ P(no2^{nd}signal|signal) &= P(no2^{nd}signal|pulser) = \frac{N_{pulser}^{no-pileUp}}{N_{pulser}} \end{aligned} \tag{5.1.3}$$

where $N_{pulser}^{no-pileUp}$ is the measured number of pulser events that have been triggered by Apollo and do not show pile-up, meaning that the condition (NumberOfPulses == 1 & SingleTrigger) is always true, and N_{pulser} is the total number of triggered pulser event for the channel-run pair that we are considering.
The probability that given an event window there are no pulser events in it, depends only on the pulser firing frequency with respect to the event window size. This is in fact equal to the probability that the current event window is not the one in which the pulser is firing.

Therefore we can rewrite:

$$P(noPulser|signal) = \frac{T_{pulser} - window}{T_{pulser}} \tag{5.1.4}$$

Combining the two contributions together we obtain the total pile-up rejection efficiency

$$\xi_{PileUp-Rej} \equiv P(goodSignal) = \frac{N_{pulser}^{nopile-up}}{N_{pulser}} \times \frac{T_{pulser} - window}{T_{pulser}} \ . \tag{5.1.5}$$

In conclusion I must make a note on the uncertainties on these efficiencies: we used the Clopper-Pearson interval to account for the statistical error on detection, energy reconstruction and pile-up rejection efficiencies. However, due to the high statistics of the pulser events the contribution of this uncertainty to the error on the overall combined selection efficiency is negligible being more than two orders of magnitude smaller than the uncertainty on PSA and coincidence.

5.1.2 Efficiency of Coincidence and PSA

The last two event selections on which we have to compute the efficiencies are PSA and coincidence. Differently from the efficiency related to the base quality cuts, this time we will compute the efficiencies directly on the signals of background data for each dataset, including in the calculations all the channel-run pairs. In spite of the method used in CUORE-0 which expects to tune the cuts on 50% of the data and compute the efficiencies on the other 50%, in CUORE, we prefer to increase the statistics on the efficiency evaluation and to tune the cuts on one spectral line and use an other to compute the efficiencies.
In particular, in the case of PSA event selection, the tuning is performed on the ^{40}K, thus the efficiency evaluation is done on the the 2615 keV γ-ray line of ^{208}Tl , which is the closest line to the ROI.
On the other hand, beyond the fact that the time jitter is found by coincidence sequence using the ^{208}Tl line, the 2615 keV γ-ray peak is also not suited for evaluating the anti-coincidence efficiency because its events occasionally occur in coincidence with other physical events due to the same decay. Therefore, we use for the efficiency evaluation of the anti-coincidence cut the 1462 keV γ-ray peak from ^{40}K decay, which is composed by truly individual events.
Since the efficiencies at the end are combined, we want to isolate only the effect of a single cut on the data, without replicate those efficiencies that have been previously calculated. Therefore, from the initial set of data used for the PSA efficiency evaluation all events that do not pass the base quality cuts have been removed. Likewise for the coincidence

efficiency evaluation, in which case we reject all events that do not pass the base quality cuts and the PSA event selection.
Despite the difference in the choice of the γ peak from the background spectrum and the different event selection, the procedure to calculate the efficiency is the same for both PSA and coincidence. Once we select the events from the chosen peak, the region of interest is divided into peak and sidebands. The sidebands are used to evaluate the background to be subtracted from the peak region, while the signal region is chosen to be equal to 3σ from the peak mean. Figure (5.1.1) is an illustrative schematics of this procedure: S_i is the number of events in the peak region and B_i is the number of events due to background in the peak region and it is estimated starting from the side bands region. The i index can be u or c representing respectively the number of entries before and after the cuts.

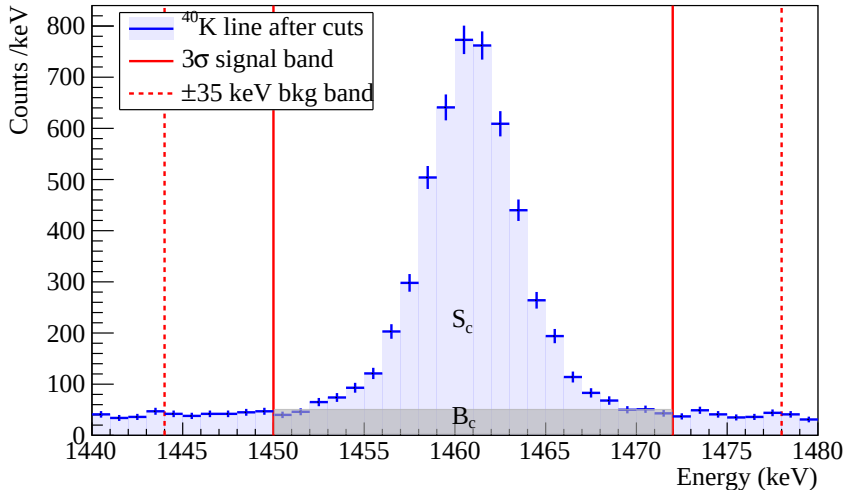

Figure 5.1.1: *Plot representing the ^{40}K peak in the background spectrum after all cuts. This plot has the only purpose of illustrating the procedure of the efficiency evaluation with the use of the signal and side bands.*

The width of the peak region plus the width of the side bands is fixed in order to maximize the portion of the spectrum used for the efficiency evaluation without encountering other adjacent lines of the background spectrum. It is $1460 \pm 35\,\text{keV}$ for ^{40}K and $2615 \pm 60\,\text{keV}$ for ^{208}Tl . Consequently, an enlargement of the peak region width implies a narrowing of the sideband region. Cut efficiency is then defined as

$$\xi_{PSA-coinc} = \frac{S_c - B_c}{S_u - B_u} \tag{5.1.6}$$

where the propagation of the errors follows the usual Poisson statistics.

A consistency check is performed for both PSA and coincidence to ensure that the choice of the signal band does not affect the efficiency calculation, as well as their statistical error: the same procedure has been repeated for an increasing number of σs so that the signal band increases at the expense of the side bands. Figure (5.1.2) demonstrate that this is not the case and the efficiency remain consistent for any choice of the signal band width.

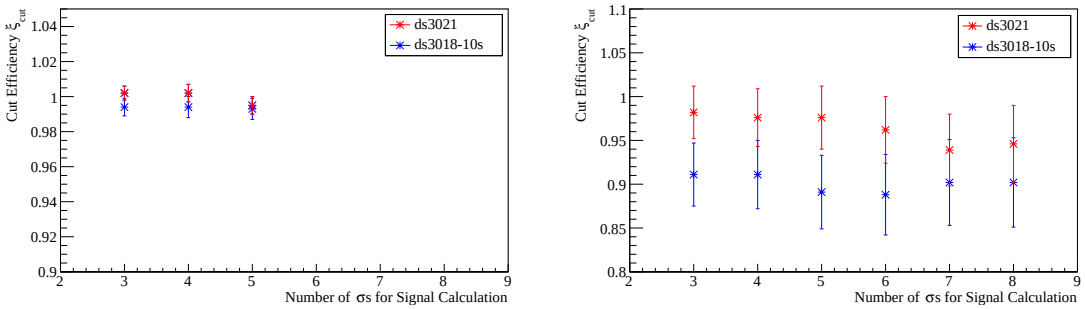

Figure 5.1.2: *Variations of the efficiency are well within the statistical error for the two datasets. Left: PSA cut efficiency. Right: anti-coincidence cut efficiency.*

Finally Table (5.1.2) shows the results for the efficiencies as function of the dataset. The global cut efficiency has been obtain combining the five single efficiencies described in this Section. Note that the higher global efficiency for the dataset 3021 with respect to the one of dataset 3018 is a further indication of the improvements obtain with the optimization campaign. In fact, for dataset 3018, the greater noise level and the higher energy thresholds cause more events to fail the analysis cuts, thus resulting in a lower selection efficiency. In the next Section we will refer to this global efficiency as ξ_γ.

Efficiency	Method	dataset 3018	dataset 3021
Detection	Pulser	0.998	0.997
Energy Recon.	Pulser	0.992	0.992
Pile-up Rejec.	Pulser	0.956	0.967
PSA	^{208}Tl	0.911 ± 0.036	0.982 ± 0.030
Coincidence	^{40}K	0.944 ± 0.005	1.000 ± 0.004
Global cut efficiency		0.8567 ± 0.0342	0.9396 ± 0.0289

Table 5.1.1: *Selection efficiencies for five different sources, averaged on all runs and channels of the same dataset and the overall cut efficiency obtained by combining the ones above. For each source of selection efficiency the method used to calculate it is also specified.*

5.2 Fit of the Region of Interest

5.2.1 Modelling the Region of Interest

The core of the $0\nu\beta\beta$ decay analysis is the fit of the ROI, a region that ranges from 2465 keV to 2575 keV including Q-value of $0\nu\beta\beta$ decay ($Q_{\beta\beta}$) at 2527.515 keV. The ultimate goal of the ROI fit is to test how likely it is to have some signal rate at $Q_{\beta\beta}$ which could indicate the presence of $0\nu\beta\beta$ decay events. A secondary target for the fit is the evaluation of the flat background rate in the ROI, figure of merit indicating if the level of residual radioactive contamination in the detector complies with the design expectation of 0.01 counts/(keV·kg·yr).

The chosen ROI range is wide enough to allow a proper fit of the flat background and posited peak centered at $Q_{\beta\beta}$, but it is sufficiently narrow not to include the tail of the 2615 keV ^{208}Tl line on one side and the 2448 keV line from ^{214}Bi . However, within the ROI region there is a small peak at about 2506 keV due to the coincident absorption of two ^{60}Co γ-rays, which we include in the ROI fit.

We model the ROI with a flat background dataset dependent and two peaks for the ^{60}Co and the hypothetical $Q_{\beta\beta}$ peak, using the line shape model obtained for each channel-dataset from the detector response fit on the ^{208}Tl line (see Section (4.3)). We can summarize the ROI model with the following expression:

$$\begin{aligned} f_{ROI}(E;Ch,Ds) = &\sum_{Ch,Ds} \epsilon(Ch,Ds)\xi_\gamma(Ds)R_{Co}e^{-t/\tau_{Co}} \cdot Co60Func(E;Ch,Ds) \\ &+ \epsilon(Ch,Ds)\xi_C\xi_\gamma(Ds)R_{\beta\beta} \cdot Q\beta\beta Func(E;Ch,Ds) \\ &+ \epsilon(Ch,Ds)R_{bkg}(Ds) \cdot BkgFunc(E) \end{aligned} \tag{5.2.1}$$

where $\epsilon(Ch,Ds)$ is the channel-dataset exposure which is fixed by the data taking, $\xi_\gamma(Ds)$ is the dataset dependent selection efficiency evaluated on γ lines from background spectrum computed in Section (5.1) and ξ_C is the $0\nu\beta\beta$ decay full containment efficiency, namely the probability that the decay is fully contained in a single crystal determined by Monte Carlo simulations. As already anticipated the two functions representing the ^{60}Co and $Q_{\beta\beta}$ peaks come from the detector response fit, namely the three-gaussian photo peak studied in Section (4.3). Their explicit form is reported below,

$$Q\beta\beta Func(E) = \frac{1}{\sqrt{2\pi}\cdot\eta\sigma}\cdot e^{-\frac{(E-\chi_{\beta\beta\mu})^2}{2\eta\sigma^2}} + R_L\cdot e^{-\frac{(E-E_{RL}\cdot\chi_{\beta\beta\mu})}{2\eta\sigma^2}} + R_H\cdot e^{-\frac{(E-E_{RH}\cdot\chi_{\beta\beta\mu})}{2\eta\sigma^2}} \tag{5.2.2}$$

$$Co60Func(E) = \frac{1}{\sqrt{2\pi}\cdot\eta\sigma}\cdot e^{-\frac{(E-q\chi_{Co}\mu)^2}{2\eta\sigma^2}} + R_L\cdot e^{-\frac{(E-E_{RL}\cdot q\chi_{Co}\mu)}{2\eta\sigma^2}} + R_H\cdot e^{-\frac{(E-E_{RH}\cdot q\chi_{Co}\mu)}{2\eta\sigma^2}} \tag{5.2.3}$$

where *eta* is the energy resolution scaling factor, computed at the end of the previous Chapter, which allows to shift the σ best fit from the detector response, for each channel-dataset, down to the ROI. All the parameters but $\chi_{\beta\beta}$, q and χ_{Co} are channel-dataset dependent and have been fixed by the detector response fit and shifted down to the region of interest. The energy ratio $\chi_{\beta\beta}$ is instead a global parameter that is fixed to $(2527.515\,\text{keV})/(2614.511\,\text{keV})$, hence the position of the $Q_{\beta\beta}$ posited peak is fixed at the Q-value: in fact we do not believe the $0\nu\beta\beta$ decay peak to have different quenching factor from the single γ lines used in calibration. At the same time, by expressing the peak mean as

$$\mu_{\beta\beta} = \chi_{\beta\beta}\cdot\mu \tag{5.2.4}$$

where μ is the best fit position of the ^{208}Tl peak for a particular channel-dataset pair, we correct for any possible bias in the energy calibration introduced by the use of a simple gaussian in the calibration procedure.

The same argument is valid also for χ_{Co}, which is a global energy ratio between the nominal sum of the ^{60}Co lines and the ^{208}Tl position: $(2505.720\,\text{keV})/(2614.511\,\text{keV})$. This time however the peak position is left free to vary in the fit, by mean of the parameter q, which accounts for a possible quenching factor due to the superposition of two γ interactions. The ^{60}Co peak position is thus

$$\mu_{Co} = q\cdot\chi_{Co}\cdot\mu \tag{5.2.5}$$

Finally the $BkgFunc(E)$ is simply a zero order polynomial representing the flat background in the ROI.

The remaining parameters of Equation (5.2.1) to discuss are $R_{\beta\beta}$ and R_{Co}. The former represents the $0\nu\beta\beta$ decay signal rate per mass unit while the latter is the ^{60}Co decay signal rate at the beginning of the first dataset; the time evolution of the ^{60}Co decay signal rate is modelled with an exponential decay where τ_{Co}=2.4·10^8 s is the ^{60}Co lifetime. Both parameters are expressed in counts/(kg·yr) and are allowed to float freely, even to negative values.

We summarize all the fit parameters in Table (5.2.1), reminding that conversely to the ^{208}Tl line fit, here we have only five floating parameters.

Parameter	Domain	Range	Par. Number
$R_{\beta\beta}$	Global	– counts/(kg·yr)	1
R_{Co}	Global	(0 – 2) counts/(kg·yr)	1
R_{Bkg}	Ds	(0.005 – 1) counts/(kg·yr)	2
q	Global	0.998 – 1.002	1
Parameter for full detector			5

Table 5.2.1: *Summary of floating parameters in the ROI fit. All the other parameters in the model describing the ROI have been determined by other studies and are therefore fixed in this fit.*

5.2.2 Fit Results

We perform on the ROI an UEML simultaneous fit, with the model described above, using the RooFit software package.

The $0\nu\beta\beta$ decay rate ($\Gamma_{0\nu}$) we aim to find can be derived from the $0\nu\beta\beta$ signal rate ($R_{\beta\beta}$) used in the fit model via the following relation:

$$\Gamma_{0\nu} = R_{\beta\beta} \cdot \frac{M_{TeO_2}}{a_I \cdot N_A} \tag{5.2.6}$$

where M_{TeO_2}= 159.6 g·mol^{-1} is the molar mass of TeO_2 , a_I=0.3417 is the ^{130}Te isotopic abundance and N_A=6.022·10^{23} mol^{-1} is the Avogadro's number. In other words, we are converting the TeO_2 mass in number of ^{130}Te atoms. We can therefore build the likelihood function using directly $\Gamma_{0\nu}$ instead of $R_{\beta\beta}$.

The likelihood function that we use to for the ROI fit is

$$\mathcal{L}(\text{Data}|\Gamma_{0\nu}, \boldsymbol{\theta}) = \frac{\lambda^N}{N!} e^{-\lambda} \prod_{Ch,Ds}^{N} f_{ROI}(Ds, Ch, E; \Gamma_{0\nu}, \boldsymbol{\theta}) \tag{5.2.7}$$

where θ are the floating parameters not explicitly written in the likelihood (R_{Co}, R_{bkg}, q), N is the number of events in the ROI and λ is the number of events expected in the ROI for a given set of parameters. The best fit for the floating parameters is found by RooFit maximizing numerically the negative log-likelihood of Equation (5.2.7).

During the development, debugging and optimization of the ROI fitting code we use the blinded data in order not to bias the results by doing an ad hoc optimization of the fit parameters. In Figure (5.2.1) we depict the result of the UEML simultaneous fit on the ROI of the blinded data. The salted peak at $Q_{\beta\beta}$ (indicated in Figure (5.2.1) by the red dotted line) is here much more prominent than the ^{60}Co , being constituted by a significant fraction of the ^{208}Tl peak in physics data.

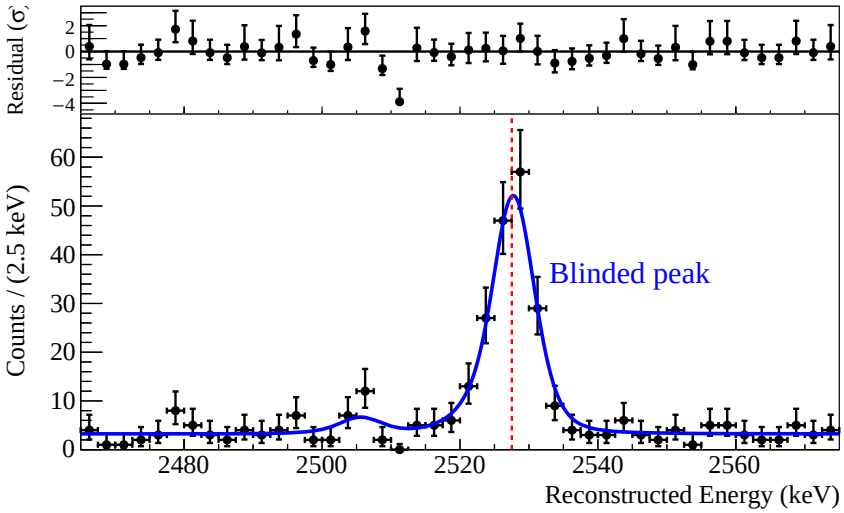

Figure 5.2.1: *Fit of the ROI using blinded data during the parameter optimization. Two peaks are thus evident: the first, due to ^{60}Co decay coincident γs, is barely emerging from the flat background while the second, centered at 2527.515 keV is the salted peak created by the blinding algorithm.*

After the unblinding the ROI fit is performed for the last time obtaining the best fit for the $0\nu\beta\beta$ decay rate and for the background rate for the two datasets. The best fit function is reported in Figure (5.2.2) and the best fit parameter values are summarized in Table (5.2.2).

Parameter	Best Fit	
$\Gamma_{0\nu}$ (yr^{-1})	$-1.0^{+0.4}_{-0.3} \cdot 10^{-25}$	
R_{Co} (counts/(kg·yr))	0.24 ± 0.08	
μ_{Co} (keV)	2506.4 ± 1.2	
	Dataset 3018	Dataset 3021
R_{bkg} (10^{-2} counts/(keV·kg·yr))	1.49 ± 0.18	1.35 ± 0.19

Table 5.2.2: *Best fit results from ROI fit, with statistical only uncertainties. Note: the quenching q of the cobalt peak has been included in the ^{60}Co peak position for a more straight forward reading of the results.*

In order to provide a unique figure of merit for the background index, we average the background rates of the two datasets weighting for the corresponding exposure. In the hypothesis of no signal[1] in the $0\nu\beta\beta$ decay posited peak, the so obtained background

[1]The background rate is computed replicating the ROI fit with the $0\nu\beta\beta$ peak signal fixed to zero.

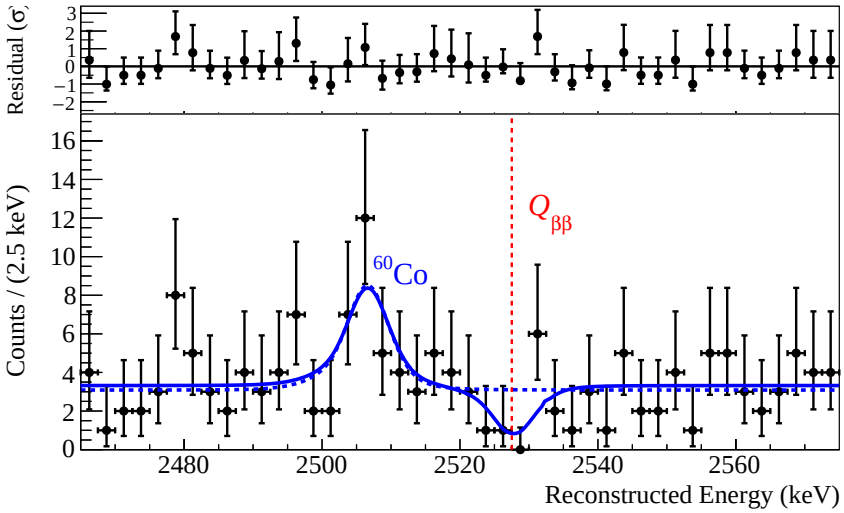

Figure 5.2.2: *ROI fit of the unblinded physics data. The dotted blue line indicates the ROI fit with the signal rate of the $0\nu\beta\beta$ fit fixed to zero, used to evaluate the background rate. The dotted red line indicates instead the position of the ^{130}Te $0\nu\beta\beta$ decay Q-value.*

average rate is thus

$$R_{bkg} = (0.014 \pm 0.002)\text{counts}/(\text{kev} \cdot \text{kg} \cdot \text{yr}) \ . \tag{5.2.8}$$

5.3 Systematics

This Section is dedicated to the systematic uncertainty which we must account for before we compute our final $0\nu\beta\beta$ limit.

In general we divide the systematics contribution in two types: a contribution proportional to the true decay rate, namely a systematic scaling σ_{sca}, and an additive contribution independent of the decay rate which we call σ_{add}.

There are several sources of systematics contributing to the $0\nu\beta\beta$ limit uncertainty. The first source of systematics is a scaling uncertainty on the signal selection efficiency ξ_γ; then we have the contribution of effects introduced by choices in the high level analysis, namely the evaluation of the detector response (whether or not the sub-peaks are necessary to describe the line shape), the energy resolution, the position of $Q_{\beta\beta}$ which is due to the energy scale, the shape that we choose to model the background and finally the bias introduced by the fit.

5.3.1 Computing Systematic Errors on $\Gamma_{0\nu}$

With the exception of the uncertainty due to the signal selection efficiency that is a straightforward scaling uncertainty, we estimate the systematics on the measured decay rate with a Monte Carlo approach. In few words the procedure simulates a large ensemble of pseudo-experiments and fits them with our model of the ROI (Equation (5.2.1)).

The procedure to compute the systematic uncertainties is a multistep process that starts from the best fit model obtained earlier in this Chapter (Section (5.2.2)). For each of the parameters on which we want to calculate the systematics, we modify by 1σ its value in the best fit model. Then we us the modified best fit model to generate a sample of Monte Carlo events with a simulated $0\nu\beta\beta$ signal with a decay rate in the range from 0 to $2{\cdot}10^{-24}\,\mathrm{yr}^{-1}$; we simulate many experiments for several values of the decay rate[2], each one having 155 events (equal to those observed) plus the number of events expected by the assumed decay rate. Each set of events is fit with our best fit model (with unmodified nuisance parameters) and the trend of decay rates resulting from the fit is studied: we fit the fitted decay rates as function of their true values with a first order polynomial to see how the slope differs from one and the intercept from zero. Two examples of such distribution are reported in Figure (5.3.1): on the left are plotted in blue the fitted decay rated from 6000 generated experiments to test the fit bias while on the right are plotted the fitted decay rates from 6000 experiments generating by neglecting the sub-peaks of the detector response.

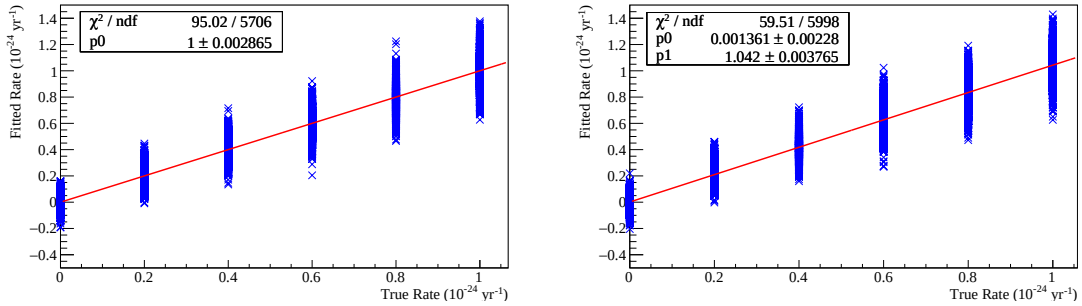

Figure 5.3.1: *Distribution of fitted decay rates from 6000 toy Monte Carlo experiments as a function of their simulated (true) values. In red is the linear fit from which we extract the slope and the intercept. Left: evaluation of fit bias using pseudo-experiments generated without varying any nuisance parameters; the fit is fixed to a zero intercept. Right: evaluation of line shape bias using pseudo-experiments generated ignoring the detector response sub-peaks; in this case the fit is not fixed to a zero intercept.*

[2]Typically we simulate 1000 pseudo-experiments for each chosen value of the decay rate.

Similarly we follow the same procedure for the energy resolution, the energy scale and the background shape (we try linear and parabolic background shapes). From the linear fit of the fitted decay rate versus true decay rate we derive the additive and scaling systematic uncertainties (σ_{sca} and σ_{add}) reported in Table (5.3.1).

	Additive (10^{-25} yr^{-1})	Scaling (%)
Line shape	0.02	2.4
Energy resolution	–	1.5
Fit bias	–	0.3
Energy scale	–	0.2
Background shape	0.05	0.8
Selection efficiency	2.4%	

Table 5.3.1: Systematic uncertainties on the best fit decay rate $\Gamma_{0\nu}$ in case of zero signal (additive) and as a percentage of nonzero signal (scaling).

As last step before extracting the final limit we must combine the systematic uncertainties from different sources, listed in Table (5.3.1). For each source of bias we calculate the error it introduces in our measurement with the following:

$$\sigma_{syst}(\Gamma_{0\nu}) = (\sigma_{add} + \Gamma_{0\nu})\sigma_{sca} \ . \tag{5.3.1}$$

Finally the uncertainties from the different contributions are combined in quadrature

$$\sigma^2_{syst}(\Gamma_{0\nu}) = (\sigma_{add,1} + \Gamma_{0\nu})^2\sigma^2_{sca,1} + (\sigma_{add,2} + \Gamma_{0\nu})^2\sigma^2_{sca,2} + ... \ . \tag{5.3.2}$$

5.4 $0\nu\beta\beta$ Limit

In this last Section I will describe the method used to extract a limit for decay rate of $0\nu\beta\beta$ decay in ^{130}Te . This is the last step of the analysis carried out in this Thesis which will leat to the most stringent limit published so far on ^{130}Te . We will finally combine this result with the previous limits obtained by the CUORE collaboration with the CUORE-0 and Cuoricino experiments.

5.4.1 From the Best Fit to the Limit

Given the best fit parameters of Table (5.2.2), which give no evidence for a positive $0\nu\beta\beta$ signal, we build a posterior Bayesian probability distribution for our data

$$\mathcal{P}^{post}_{stat}(\Gamma_{0\nu}|\text{Data}) = \mathcal{P}_{stat}(\text{Data}|\Gamma_{0\nu})\pi(\Gamma_{0\nu}) \tag{5.4.1}$$

where $\mathcal{P}_{stat}(\text{Data}|\Gamma_{0\nu})$ is known in statistics as profile likelihood which allows to reduce our multi-dimentional likelihood function in a function that only depends on the paramenters of interest (in this case $\Gamma_{0\nu}$) and not on the other nuisance paramenters. The profile likelihood, or likelihood ratio is obtained by evaluating

$$\mathcal{P}_{stat}(\text{Data}|\Gamma_{0\nu}) \equiv \frac{sup_{\boldsymbol{\theta}}\{\mathcal{L}(\text{Data}|\Gamma_{0\nu}, \boldsymbol{\theta})\}}{\mathcal{L}(\text{Data}|\widehat{\Gamma}_{0\nu}, \widehat{\boldsymbol{\theta}})} \tag{5.4.2}$$

where $\mathcal{L}(\text{Data}|\widehat{\Gamma}_{0\nu}, \widehat{\boldsymbol{\theta}})$ is the likelihood of Equation (5.2.7) evaluated at the best fit point, and $sup_{\boldsymbol{\theta}}\{\mathcal{L}(\text{Data}|\Gamma_{0\nu}, \boldsymbol{\theta})$ is a function obtained by iterating on all possible values of $\Gamma_{0\nu}$ and for each fixed value of $\Gamma_{0\nu}$ maximizing on the nuisance parameters $\boldsymbol{\theta}$. Equivalently we can take the profile Negative Log-Likelyhood (NLL), depicted with a red dotted line in Figure (5.4.1) and written as

$$-log\mathcal{P}_{stat}(\text{Data}|\Gamma_{0\nu}) \equiv -min_{\boldsymbol{\theta}}\{log\mathcal{L}(\text{Data}|\Gamma_{0\nu}, \boldsymbol{\theta})\} + log\mathcal{L}(\text{Data}|\widehat{\Gamma}_{0\nu}, \widehat{\boldsymbol{\theta}}) \ . \tag{5.4.3}$$

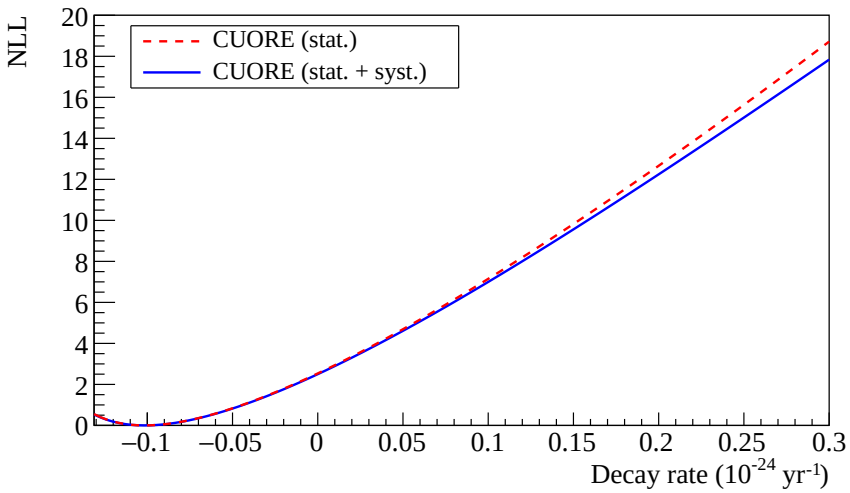

Figure 5.4.1: *Profile NLL obtained from the best parameters of the ROI fit for CUORE. The dotted red curve represents the profile likelihood with only statistic uncertainty while in blue the curve that includes both statistic and systematic uncertainties.*

Once the systematics are evaluated (see Section (5.3)), this NLL curve is modified accordingly. One of the standard results from statistics (see for example [72]) is that $-2log$(Profile Likelihood) converges in distribution to a chi-square random variable with a number of degrees of freedom equal to the number of parameters of interest (in this case only $\Gamma_{0\nu}$). We can therefore define a chi-square related to our profile likelihood which

includes statistic uncertainties only as

$$\chi^2_{stat}(\Gamma_{0\nu}) \equiv -2log[\mathcal{P}_{stat}(\text{Data}|\Gamma_{0\nu})] \tag{5.4.4}$$

and one chi-square statistic for the systematic uncertainty from Equation (5.3.2)

$$\chi^2_{syst}(\Gamma_{0\nu}) \equiv \frac{(\Gamma_{0\nu} - \widehat{\Gamma}_{0\nu})^2}{\sigma^2_{syst}} \tag{5.4.5}$$

We can now simply combine our statistics and systematics errors

$$\frac{1}{\chi^2_{tot}} = \frac{1}{\chi^2_{stat}} + \frac{1}{\chi^2_{syst}} \tag{5.4.6}$$

from which, inverting the procedure used in Equation (5.4.4), we can obtain a profile likelihood $\mathcal{P}_{tot}(\text{Data}|\Gamma_{0\nu})$ including both statistics and systematic uncertainties and plotted in blue in Figure (5.4.1)

$$\mathcal{P}_{tot}(\text{Data}|\Gamma_{0\nu}) = e^{-0.5\chi^2_{tot}} \ . \tag{5.4.7}$$

The prior $\pi(\Gamma_{0\nu})$ in Equation (5.4.1) imposes the decay rate to be positive, which is a reasonable physical requirement

$$\pi(\Gamma_{0\nu}) = \begin{cases} 1, & \Gamma_{0\nu} > 0 \\ 0, & otherwise \end{cases} \ . \tag{5.4.8}$$

The limit on the decay rate $\Gamma_{0\nu}$ of ^{130}Te at 90% C.L., considering only statistical uncertainty, is obtained by normalizing to unity our posterior probability distribution and integrating it up to the needed confidence level, in this case $\alpha_{C.L.}$=0.9.

$$\alpha_{C.L.} = \int_{-\inf}^{\Gamma^{limit}_{0\nu}} \mathcal{P}^{post}_{stat}(\Gamma_{0\nu}|\text{Data})d\Gamma_{0\nu} = \frac{\int_0^{\Gamma^{limit}_{0\nu}} \mathcal{P}_{stat}(\text{Data}|\Gamma_{0\nu})d\Gamma_{0\nu}}{\int_0^{\inf} \mathcal{P}_{stat}(\text{Data}|\Gamma_{0\nu})d\Gamma_{0\nu}} \tag{5.4.9}$$

The upper limit we get for $\Gamma_{0\nu}$ by solving this integral is

$$\Gamma_{0\nu} < 0.051 \cdot 10^{-24}\,\text{yr}^{-1} \text{ (90\% CL, syst. included)} \tag{5.4.10}$$

or equivalently we can write it as a lower limit for the half life of the $0\nu\beta\beta$ decay of ^{130}Te , given the relation $T^{0\nu-limit}_{1/2} = ln2/(\Gamma^{limit}_{0\nu})$

$$T^{0\nu}_{1/2} > 1.3 \cdot 10^{25}\,\text{yr} \text{ (90\% CL, syst. included)} \tag{5.4.11}$$

Once we obtain the decay rate at which the area under the curve is the 90% of the total, we can state that given the data and fit result, the rate of $0\nu\beta\beta$ decay of ^{130}Te is less than the determined value $\Gamma_{0\nu}^{limit}$ with a 90% probability, namely the Bayesian limit we aim to obtain from this analysis.

Starting from the same profile NLL curve to determine frequentist limit, evaluated by following the Rolke method [73, 74]. In this calculation we interpret once more the profile likelihood as a χ^2 statistic, and scan the curve from its true minimum until the rate corresponding to a 90% p-value is reached. In this interpretation, the percentage refers not to the value of the decay rate, which is unknown but absolute, but rather to a chance of observation in a large number of hypothetical re-runs of the same experiment.
The frequentist limit obtained for $\Gamma_{0\nu}$ is as expected slightly more optimistic than the correspondent Bayesian one, and is

$$\Gamma_{0\nu} < 0.033 \cdot 10^{-24}\,\mathrm{yr}^{-1}\ (90\%\ \mathrm{CL,\ syst.\ included}) \tag{5.4.12}$$

corresponding to a limit on the half life of ^{130}Te $0\nu\beta\beta$ decay of

$$T_{1/2}^{0\nu} > 2.1 \cdot 10^{25}\,\mathrm{yr}\ (90\%\ \mathrm{CL,\ syst.\ included})\ . \tag{5.4.13}$$

5.4.2 Combining This With The Previous Results

If we combine the results obtain in this analysis from CUORE, which had so far a total exposure of 24.0 kg·yr of ^{130}Te (the equivalent TeO_2 exposure is 86.3,kg·yr), with those of the previous experiments carried by the CUORE collaboration, we can get an even more stringent limit on $0\nu\beta\beta$ decay of ^{130}Te . We combine the limits by adding together the profile NLL curve of CUORE[75] with those from 9.8 kg·yr of ^{130}Te exposure from CUORE-0[43] and 19.8 kg·yr from Cuoricino [76], depicted in Figure (5.4.2) with a dashed red line and a dotted green line respectively. The so obtain combined profile NLL curve is shown with a solid black line in Figure (5.4.2).
From the combined profile NLL curve we can then obtain the new upper limit on the ^{130}Te decay rate at the 90% C.L., following the Bayesian method of Equation (5.4.9) described above:

$$\Gamma_{0\nu} < 0.047 \cdot 10^{-24}\,\mathrm{yr}^{-1}\ (90\%\ \mathrm{CL,\ syst.\ included}) \tag{5.4.14}$$

corresponding to a limit on the half life of ^{130}Te $0\nu\beta\beta$ decay of

$$T_{0\nu}^{1/2} > 1.5 \cdot 10^{25}\,\mathrm{yr}\ (90\%\ \mathrm{CL,\ syst.\ included})\ . \tag{5.4.15}$$

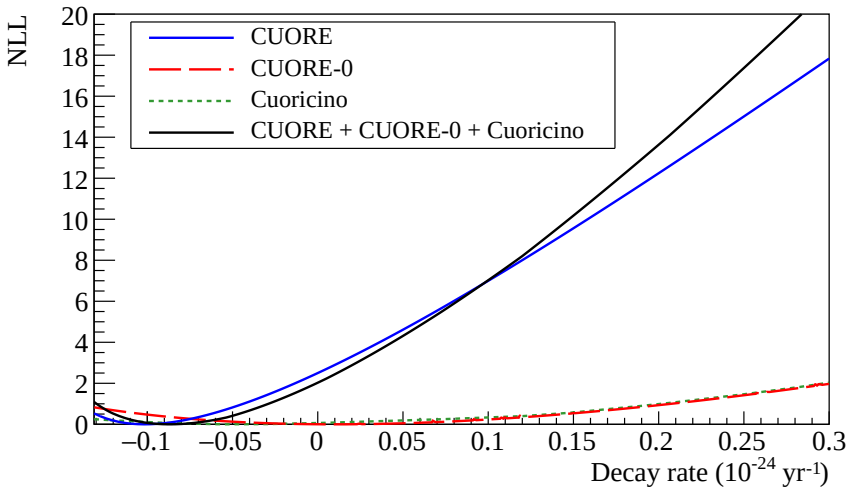

Figure 5.4.2:

Again we can use the same profile NLL to compute a combined limit of CUORE, CUORE-0 and Cuoricino, following the Rolke frequentist technique. This result yields a decay rate upper limit of

$$\Gamma_{0\nu} < 0.031 \cdot 10^{-24}\,\mathrm{yr}^{-1} \text{ (90\% CL, syst. included)} \tag{5.4.16}$$

equivalent to a lower limit on the ^{130}Te $0\nu\beta\beta$ decay half life of

$$T_{0\nu}^{1/2} > 2.2 \cdot 10^{25}\,\mathrm{yr} \text{ (90\% CL, syst. included) .} \tag{5.4.17}$$

Finally, as last step of this work of Thesis I will use the same procedure described in Section (1.4) and Section (1.5.1) to convert this result in a range in the effective Majorana mass, in the hypothesis that $0\nu\beta\beta$ decay is mediated by the exchange of light Majorana neutrinos. We will use the combined Bayesian limit on the $0\nu\beta\beta$ decay rate of Equation (5.4.14), the phase-space factors from Ref. [77] and the nuclear matrix elements from a range of different models [78, 79, 80, 81, 82, 83, 84]. For the calculation we assume an axial coupling $g \simeq 1.27$. The range of effective Majorana mass that will set a new upper limit for ^{130}Te in the $m_{\beta\beta}$ versus $m_{lightest}$ parameter space is $m_{\beta\beta} < (140 - 400)\,meV$ at 90% C.L.

This is so far the best limit obtained for ^{130}Te and it allows CUORE to enter in the game with the other big $0\nu\beta\beta$ experiments currently taking data.

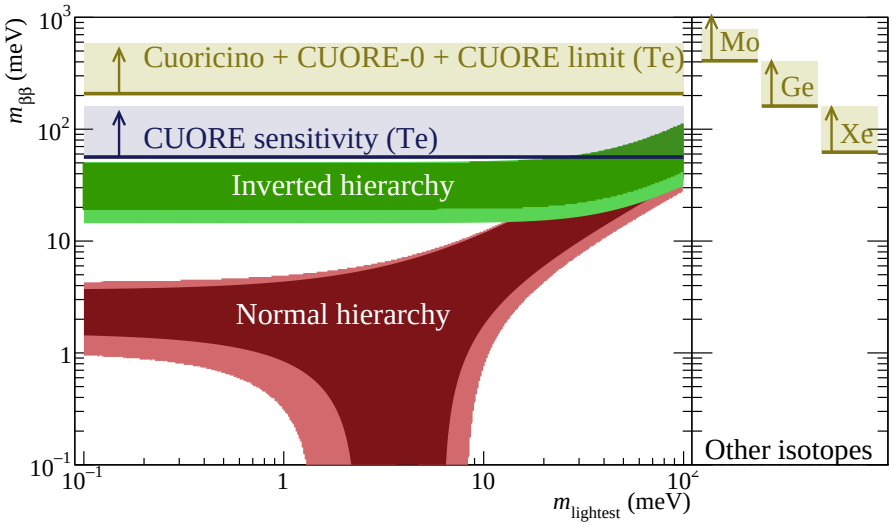

Figure 5.4.3: *Effective Majorana mass $m_{\beta\beta}$ as a function of $m_{lightest}$. The red and green bands represent respectively the NH and IH mutual excluding scenarios. The yellow band in the central plot represents this combined limit for CUORE[75] and the blue band is the CUORE projected sensitivity after 5 yr of data taking. The yellow bands on the right represent the lower limit set on the ^{100}Mo $0\nu\beta\beta$ decay by the NEMO-3 experiment [25]; the latest results on ^{76}Ge set by the GERDA experiment [23]; the latest limit set on ^{136}Xe by the KamLAND-Zen experiment [24].*

Conclusions

In this Thesis I reported the main steps that brought to the publication of the first CUORE results [75].
I was particularly involved in the optimization campaign that allowed a more stable data taking and an improvement in the energy resolution. In particular I discussed in detail the procedure to set the bias voltage for the NTD polarization circuit; the development of a procedure to automatically set the derivative trigger thresholds and the evaluation of the energy thresholds for all the channels; the implementation of a new active system to stabilize in time the noise contributions induced by the PT cryocoolers and the analysis that lead to find an optimal PT phase difference whose effect is the cancellation of this noise. This last optimization procedure recently lead to the publication of a paper on the PT active noise cancellation technique [62].
Then I followed the first physics data acquired by CUORE from its production to the compilation of the energy spectrum, discussing all the main steps of the low level analysis. Lastly I described in detail the procedure to obtain a channel dependent detector response using a simultaneous fit on the ^{208}Tl line from calibration data. Eventually, with the energy spectrum and the detector response we were able to fit the region of interest and, from its best fit values, to extract a limit to the $0\nu\beta\beta$ decay rate of ^{130}Te.
Including efficiencies and systematics we set the current best limit on the half-life of ^{130}Te

$$T_{0\nu}^{1/2} > 1.5 \cdot 10^{25}\,\text{yr}\ (90\%\ \text{CL, syst. included}) \tag{5.4.18}$$

and convert it to a limit on the effective Majorana mass $m_{\beta\beta}$ <(140 - 400) meV, in the hypothesis of $0\nu\beta\beta$ decay mediated by light Majorana neutrinos.
In conclusion, although we foreseen further improvements in energy resolution and analysis procedures, CUORE already demonstrated to be a competitive experiment for the search of $0\nu\beta\beta$ decay. In addition, for the first time, it was proven by the CUORE collaboration that it is possible to run a ton-scale experiment using the bolometric technique at temperatures as low as 10 mK.

List Of Acronyms

SM Standard Model

NH Normal Hierarchy

IH Inverted Hierarchy

QD Quasi Degenerate

QRPA Quasiparticle Random Phase Approximation

ISM Interacting Shell Model

IBM-II Interacting Boson Model

PMTs Photo Multiplier Tubes

CUORE Cryogenic Underground Observatory for Rare Events

LNGS Laboratori Nazionali del Gran Sasso

C.L. Confidence Level

ROI Region of Interest

PT Pulse Tube

PTs Pulse Tubes

DU Dilution Unit

DR Dilution Refrigerator

OVC Outer Vacuum Chamber

IVC Inner Vacuum Chamber

OFE Oxygen-Free Electrolytic

HEX Heat EXchangers

MC Mixing Chamber

TSP Tower Support Plate

FWHM Full Weight Half Maximum

ETP1 Electronic Tough Pitch

DS Detector Suspension

MSP Main Support Plate

DAQ Data AQuisition

FCS Fast Cooling System

DCS Detector Calibration System

TES Transition Edge Thermistors

ST Semiconductor Thermistors

MIT Metal-Insulator Transition

VRH Variable Range Hopping

CMRR Common Mode Rejection Ratio

PGA Programmable Gain Amplifier

NI National Instrument

ADC Analog to Digital Converter

TCP/IP Transmission Control Protocol/Internet Protocol

RDCF Raw Data Continuous Flow

CR Clean Room

PTFE PoliTetraFluoroEthilene

SNR Signal to Noise Ratio

UEML Unbinned Extended Maximum Likelihood

PDF Probability Density Function

NTD Neutron Trasmutation Doped

FE Front End

OF Optimum Filter

SNR Signal to Noise Ratio

AP Average Pulse

ANPS Average Noise Power Spectrum

NPS Noise Power Spectrum

PS Power Spectrum

LD Linear Drive

LDs Linear Drives

DFT Discrete Furier Transform

OT Optimum Trigger

PSA Pulse Shape Analysis

TVL Test Variable Left

TVR Test Variable Right

MAD Median Absolute Deviation

NLL Negative Log-Likelyhood

Bibliography

[1] C. Patrignani et al. The review of particle physics. *Chin. Phys. C*, 40:100001, 2016.

[2] Alessandro Strumia. Baryogenesis via leptogenesis. In *Particle physics beyond the standard model. Proceedings, Summer School on Theoretical Physics, 84th Session, Les Houches, France, August 1-26, 2005*, pages 655–680, 2006.

[3] Gary Steigman. Observational tests of antimatter cosmologies. *Annual Review of Astronomy and Astrophysics*, 14(1):339–372, 1976.

[4] A. D. Sakharov. Violation of CP Invariance, c Asymmetry, and Baryon Asymmetry of the Universe. *Pisma Zh. Eksp. Teor. Fiz.*, 5:32–35, 1967. [Usp. Fiz. Nauk161,61(1991)].

[5] D. V. Perepelitsa. Sakharov Conditions for Baryogenesis. *PHYS G6050 Particle Phenomenology class project, Columbia University, Department of Physics ?dvp/dvp-sakharov.pdf]. http://phys.columbia.edu/*, 2008.

[6] Patrick Huet. Electroweak baryogenesis and the standard model. In *Phenomenology of Unification from Present to Future: Proceedings of the 1st International Conference, March 23-26, 1994, Rome*, pages 77–91, 1994.

[7] M. Fukugita and T. Yanagida. Baryogenesis Without Grand Unification. *Phys. Lett.*, B174:45–47, 1986.

[8] Lee Grodzins. The tabletop measurement of the helicity of the neutrino. *Nuclear Physics B - Proceedings Supplements*, 229-232:5 – 13, 2012. Neutrino 2010.

[9] Lawrence J. Hall and Mahiko Suzuki. Explicit r-parity breaking in supersymmetric models. *Nuclear Physics B*, 231(3):419 – 444, 1984.

[10] A. Zee. A theory of lepton number violation and neutrino majorana masses. *Physics Letters B*, 93(4):389 – 393, 1980.

[11] Riccardo Barbieri, Paolo Creminelli, and Alessandro Strumia. Neutrino oscillations from large extra dimensions. *Nucl. Phys.*, B585:28–44, 2000.

[12] R. N. Mohapatra and J. W. F. Valle. Neutrino mass and baryon-number nonconservation in superstring models. *Phys. Rev. D*, 34:1642–1645, Sep 1986.

[13] S. Morisi and J. W. F. Valle. Neutrino masses and mixing: a flavour symmetry roadmap. *Fortsch. Phys.*, 61:466–492, 2013.

[14] A. S. Barabash. Average and recommended half-life values for two neutrino double beta decay. *Nucl. Phys.*, A935:52–64, 2015.

[15] Alessandro Strumia and Francesco Vissani. Neutrino masses and mixings and... 2006.

[16] E. D. Commins and P. H. Bucksbaum. *Weak Interactions of Leptons and Quarks*. 1983.

[17] Jouni Suhonen. Impact of the quenching of g_{A} on the sensitivity of $0\nu\beta\beta$ experiments. *Phys. Rev.*, C96(5):055501, 2017.

[18] Jouni T. Suhonen. Value of the axial-vector coupling strength in β and $\beta\beta$ decays: A review. *Frontiers in Physics*, 5:55, 2017.

[19] B. Pontecorvo. *Zh. Eksp. Teor. Fiz.*, 33:549, (1957) and 34, 247 (1958).

[20] Ziro Maki, Masami Nakagawa, and Shoichi Sakata. Remarks on the unified model of elementary particles. *Progress of Theoretical Physics*, 28(5):870–880, 1962.

[21] J. Schechter and J. W. F. Valle. Neutrino masses in su(2) $\bigotimes$ u(1) theories. *Phys. Rev. D*, 22:2227–2235, Nov 1980.

[22] S.M. Bilenky, J. Hošek, and S.T. Petcov. On the oscillations of neutrinos with dirac and majorana masses. *Physics Letters B*, 94(4):495 – 498, 1980.

[23] M. Agostini et al. Background free search for neutrinoless double beta decay with GERDA Phase II. 2017. [Nature544,47(2017)].

[24] A. Gando et al. Search for Majorana Neutrinos near the Inverted Mass Hierarchy Region with KamLAND-Zen. *Phys. Rev. Lett.*, 117(8):082503, 2016. [Addendum: Phys. Rev. Lett.117,no.10,109903(2016)].

[25] R. Arnold et al. Results of the search for neutrinoless double-? decay in ^{100}Mo with the NEMO-3 experiment. *Phys. Rev.*, D92(7):072011, 2015.

[26] K. Eguchi et al. First results from KamLAND: Evidence for reactor anti-neutrino disappearance. *Phys. Rev. Lett.*, 90:021802, 2003.

[27] K. Asakura et al. Results from KamLAND-Zen. *AIP Conf. Proc.*, 1666:170003, 2015.

[28] in2p3 web page on nemo-3. http://nemo.in2p3.fr/nemow3/.

[29] A. Giuliani et al. A low temperature TeO_2 detector to search for double beta decay of ^{130}Te. *Proc. Joint Int. Lepton Photon Symposium at High Energies (15th) and European Phys. Soc. Conf. on High-energy Phys.*, pages 670–672, 1991.

[30] E. Fiorini. CUORE: A cryogenic underground observatory for rare events. *Phys. Rep.*, 307:309–317, 1998.

[31] M. Fehr, M. Rehkämper, and A. Halliday. Application of mc-icpms to the precise determination of tellurium isotope compositions in chondrites, iron meteorites and sulfides. 232, 03 2004.

[32] M. Redshaw et al. Masses of Te-130 and Xe-130 and Double-beta-Decay Q Value of Te-130. *Phys. Rev. Lett.*, 102:212502, 2009.

[33] N. D. Scielzo et al. Double-beta decay Q values of Te-13-, Te-128, and Te-120. *Phys. Rev.*, C80:025501, 2009.

[34] S. Rahaman et al. Double-beta decay q values of 116cd and 130te. 703:412–416, 09 2011.

[35] B.R. Firestone and L.P. Ekström. The lund/lbnl nuclear data search. Version 2.1, February 1999.

[36] D. Mei and A. Hime. Muon-induced background study for underground laboratories. *Phys. Rev.*, D73:053004, 2006.

[37] G. Bellini et al. Cosmic-muon flux and annual modulation in borexino at 3800 m water-equivalent depth. *Journal of Cosmology and Astroparticle Physics*, 2012(05):015, 2012.

[38] F. Arneodo, A. Borio di Tagliole, and F. Cavanna. Neutron background measurements in the Hall C of the Gran Sasso Laboratory. *Nuovo Cimento A*, 112-8:819–831, 1999.

[39] P. Belli et al. Deep underground neutron flux measurement with large BF_3 counters. *Nuovo Cimento A*, 101:959, 1989.

[40] L. Pandola and others. Monte Carlo evaluation of the muon-induced background in the GERDA double beta decay experiment. *Nucl. Instrum. Meth.*, A570:149–158, 2007.

[41] C. Bucci et al. Background study and Monte Carlo simulations for large-mass bolometers. *Eur. Phys. J. A*, 41:155, 2009.

[42] D. R. Artusa et al. Searching for neutrinoless double-beta decay of ^{130}Te with CUORE. *Adv. High Energy Phys.*, 2015:879871, 2015.

[43] K. Alfonso et al. Search for Neutrinoless Double-Beta Decay of ^{130}Te with CUORE-0. *Phys. Rev. Lett.*, 115(10):102502, 2015.

[44] C. Alduino et al. Analysis techniques for the evaluation of the neutrinoless double-β decay lifetime in ^{130}Te with the CUORE-0 detector. *Phys. Rev. C*, 93(4):045503, 2016.

[45] C. Alduino et al. CUORE-0 detector: design, construction and operation. *J. Instrum.*, 11(07):P07009, 2016.

[46] Buccheri, E. and others. *Nucl. Instrum. Meth.*, A768:130–140, 2014.

[47] C. Alduino et al. Measurement of the two-neutrino double-beta decay half-life of^{130} Te with the CUORE-0 experiment. *Eur. Phys. J.*, C77(1):13, 2017.

[48] H. C. Stahl. *Cryogenic Particle Detection.* Springer, 2005.

[49] B. I. Shklovskii and A. L. Efros. *Electronic Properties of Doped Semiconductors.* Springer, 1984.

[50] E. E. Haller, N. P. Palaio, M. Rodder, W. L. Hansen, and E. Kreysa. Ntd germanium: A novel material for low temperature bolometers. In R. D. Larrabee, editor, *Neutron Transmutation Doping of Semiconductor Materials*, pages 21–36. Springer US, 1984.

[51] F. Alessandria et al. The 4K outer cryostat for the CUORE experiment: Construction and quality control. *Nucl. Instrum. Meth. A*, 727:65–72, 2013.

[52] A. Alessandrello et al. Measurements of internal radioactive contamination in samples of Roman lead to be used in experiments on rare events. *Nucl. Instrum. Meth.*, 142(1):163, 1998.

[53] C. Alduino et al. The projected background for the CUORE experiment. *Eur. Phys. J.*, C77(8):543, 2017.

[54] A. Bersani et al. The CUORE Detector Suspension. *JINST?*, XXX:XXX, 2017.

[55] J. S. Cushman et al. The detector calibration system for the CUORE cryogenic bolometer array. *Nucl. Instrum. Meth. A*, 844:32–44, 2017.

[56] M. Vignati. Model of the response function of large mass bolometric detectors. *J. Appl. Phys*, 108:8, 2010.

[57] C. Arnaboldi, P. Carniti, L. Cassina, C. Gotti, X. Liu, and G. Pessina. The front-end electronics system for the CUORE experiment. 2017.

[58] Root software package web page. https://root.cern.ch/. For this first data analysis we used ROOT version 5.34.

[59] Simone Copello. Dark Matter induced annual modulation analysis in CUORE-0, Spring 2017.

[60] E. Buccheri, M. Capodiferro, S. Morganti, F. Orio, A. Pelosi, and V. Pettinacci. An assembly line for the construction of ultra-radio-pure detectors. *Nucl. Instrum. Meth. A*, 768:130–140, 2014.

[61] G. Benato et al. Radon-free environment for the installation of the CUORE $0\nu\beta\beta$ decay detector. 2017.

[62] A. D'Addabbo, C. Bucci, L. Canonica, S. Di Domizio, P. Gorla, L. Marini, A. Nucciotti, I. Nutini, C. Rusconi, and B. Welliver. An active noise cancellation technique for the cuore pulse tube cryocoolers. December 2017.

[63] E. Gatti and P. F. Manfredi. Processing the Signals From Solid State Detectors in Elementary Particle Physics. *Riv. Nuovo Cim.*, 9N1:1–146, 1986.

[64] S. Di Domizio, F. Orio, and M. Vignati. Lowering the energy threshold of large-mass bolometric detectors. *JINST*, 6:P02007, 2011.

[65] P. C. Mahalanobis. On the generalised distance in statistics. *Proc. Natl. Inst. Sci. India*, (1936):49–55, 1936.

[66] G. Cowan et al. Asymptotic formulae for likelihood-based tests of new physics. *Eur. Phys. J. C*, 71(2):1554, Feb 2011.

[67] Tom Banks. Evaluation of the CUORE-0 energy resolution. *CUORE Internal Note 101D, Version 1.3.1*, 29 June 2015.

[68] Jonathan Loren Ouellet. The Search for $0\nu\beta\beta$ Decay in ^{130}Te with CUORE-0, Spring 2015.

[69] A. D. Bryant. *A Search for Neutrinoless Double Beta Decay of ^{130}Te.* PhD thesis, University of California, Berkeley, 2010.

[70] M Carrettoni. *Data analysis for Neutrinoless Double Beta Decay.* PhD thesis, Università degli Studi di Milano-Bicocca, 2011.

[71] Alessio Caminata and Irene Nutini. CUORE PRL analysis efficiency evaluation. *CUORE Internal Note 126D*, 20 December 2017.

[72] G. Casella and R.L. Berger. *Statistical Inference.* Duxburry Press, 1990.

[73] J. Lundberg, J. Conrad, W. Rolke, and A. Lopez. Limits, discovery and cut optimization for a Poisson process with uncertainty in background and signal efficiency: TRolke 2.0. *Comput. Phys. Commun.*, 181:683–686, 2010.

[74] Wolfgang A. Rolke, Angel M. Lopez, and Jan Conrad. Limits and confidence intervals in the presence of nuisance parameters. *Nucl. Instrum. Meth.*, A551:493–503, 2005.

[75] C. Alduino et al. First Results from CUORE: A Search for Lepton Number Violation via $0\nu\beta\beta$ Decay of ^{130}Te. 2017.

[76] E. Andreotti et al. ^{130}Te Neutrinoless Double-Beta Decay with CUORICINO. *Astropart. Phys.*, 34:822–831, 2011.

[77] J. Kotila and F. Iachello. Phase space factors for double-β decay. *Phys. Rev. C*, 85:034316, 2012.

[78] J. Barea, J. Kotila, and F. Iachello. $0\nu\beta\beta$ and $2\nu\beta\beta$ nuclear matrix elements in the interacting boson model with isospin restoration. *Phys. Rev. C*, 91(3):034304, 2015.

[79] Fedor Šimkovic, Vadim Rodin, Amand Faessler, and Petr Vogel. $0\nu\beta\beta$ and $2\nu\beta\beta$ nuclear matrix elements, quasiparticle random-phase approximation, and isospin symmetry restoration. *Phys. Rev. C*, 87(4):045501, 2013.

[80] Juhani Hyvärinen and Jouni Suhonen. Nuclear matrix elements for $0\nu\beta\beta$ decays with light or heavy Majorana-neutrino exchange. *Phys. Rev. C*, 91(2):024613, 2015.

[81] J. Menendez, A. Poves, E. Caurier, and F. Nowacki. Disassembling the Nuclear Matrix Elements of the Neutrinoless beta beta Decay. *Nucl. Phys. A*, 818:139–151, 2009.

[82] Tomas R. Rodriguez and G. Martinez-Pinedo. Energy density functional study of nuclear matrix elements for neutrinoless $\beta\beta$ decay. *Phys. Rev. Lett.*, 105:252503, 2010.

[83] Nuria López Vaquero, Tomás R. Rodríguez, and J. Luis Egido. Shape and pairing fluctuations effects on neutrinoless double beta decay nuclear matrix elements. *Phys. Rev. Lett.*, 111(14):142501, 2013.

[84] J. M. Yao, L. S. Song, K. Hagino, P. Ring, and J. Meng. Systematic study of nuclear matrix elements in neutrinoless double-β decay with a beyond-mean-field covariant density functional theory. *Phys. Rev. C*, 91:024316, Feb 2015.

Acknowledgment

I am glad it is over. I liked being a Ph.D. in Genova. I learned a lot about physics and about myself, I met wonderful people and I have done many interesting experiences. I tried on my skin the meaning of working as a team for a common purpose: it was weary, but at the end it gave me a lot of satisfaction... the feeling that I belong somewhere and that I was participating in building something. On the other hand I hated my Ph.D. because for many months I felt I was alone and my self esteem became anorexic and crouched in a corner looking at me like she did not know me. I do not think it was anyone's fault. Shit happens. So yes, I am glad this chapter of my life is over. But do not mistake my words: I am very happy about my thesis and what I achieved. This last year has been a crescendo of experiences, capped by the deliver of my thesis to the referees, Claudia and Andrea, whom I thank very much. And in the way, I believe I got all my pieces back.

I would like to express my sincere gratitude to my supervisors Prof. Marco Pallavicini and Dr. Sergio Di Domizio: Marco for the continuous support during these last three years and for pointing me the right direction when everything was dark and for letting me have a second possibility; Sergio for his careful guidance into the world of data acquisition, his patience when I was asking him the same questions over and over, his suggestions during the drafting of this thesis and his immense knowledge from which I benefited.

Besides my advisors, I would like to thank the rest of the CUORE collaboration. A particular thanks goes to the LNGS group, especially Carlo, Paolo and Lucia, who hosted me for many months and with whom I spent a wonderful and exciting time when we were installing the detector and looking at the first CUORE data, as well as the most terrible time, when we could not keep the pace of all the things we needed to do. An other thanks goes to the analysis team with whom I shared the burden of the analysis of the first CUORE data: Alexey, Irene, Jeremy, Jon, Matteo, Alessio, Stefano and many others. I found into this collaboration admirable guides, colleagues and friends and I am glad for their encouragement and insightful comments.

Lastly my sincere thanks goes to the people I care about more. Nello, who is always at my

side, compliant with my lunatic ideas and who had the patience of reading a good portion of my thesis. I thanks my companions of Ph.D., Luca, Coppe, Rugge and Fede with whom I shared a wonderful and crazy time in Genova and without whom I would have already give up this difficult path that lead me to this moment. Finally I would like to thank my parents Luciana and Giorgio, because even when I am far away they are always with me, and support my choices and keep my hand when I need affection. They are the best parents I could ever had.